ADVANCES IN DNA TECHNOLOGY TOWARDS DYNAMIC ASSEMBLIES AND BIOLOGICAL APPLICATIONS

BY

NGO YIN WONG

DISSERTATION

Submitted in partial fulfillment of the requirements
for the degree of Doctor of Philosophy in Materials Science and Engineering
in the Graduate College of the
University of Illinois at Urbana-Champaign, 2013

Urbana, Illinois

Doctoral Committee:

Professor Yi Lu, Chair
Professor Paul Braun
Professor Jianjun Cheng
Professor Steve Granick

Abstract

One of the major research aims in Materials Science and Engineering for the past two decades has pertained to the development of capabilities to manipulate and characterize materials on the molecular and atomic level. This capability has been largely driven by technological and engineering advances in the semiconducting industry, where better controls and higher resolution equates to better device performance and higher profits. Inspired by such lithographic approaches, there has been a parallel push to drive bottom up, self-assembly techniques, where short and long range forces drive the assembly of nanoscale components assemble into hundreds of billions of complexes and devices simultaneously. Correspondingly, our ability to form high quality and increasingly complex structures based on the principles of self-assembly demands the development of a highly repeatable, robust, and well characterized system. While the concepts of self-assembly is simple, the realization of high quality nanoscale assembly remains a stubbornly difficult challenge due a fundamental trade-off between degree of control, throughput (yield) of the assembly, and complexity of the final assembly.

In the early 1980's, Professor Nadrian Seeman published his seminal work on the design of DNA tiles, which along with his group, became the field now known as structural DNA nanotechnology. Professor Chad Mirkin and several others then later realized the power of complementary DNA can be utilized as a "smart glue" to programmably assembly many different types of nanomaterials. In the following three decades, DNA based nanotechnology has advanced greatly due to the commercial availability of artificially synthesized oligonucleotides, a vast library of chemical and enzymatic modifications, and the work of hundreds of groups around the world. This

thesis will describe efforts made to advance the field by identifying new conjugation chemistries that enable two and three dimensional scaffolding of nanomaterials on complex DNA structures.

Another extraordinary property of DNA was first described by Larry Gold and Jack Szostak and has since evolved into what is now functional DNA (f-DNA). The role of proteins (peptide chains) and ribozymes (RNA molecules) in a litany of biological enzymatic functions have long been studied. Functional DNA follows the hypothesis that certain DNA sequences will exhibit catalytic activity (much like ribozymes and proteins) or target recognition (much like antibodies). Of particular interest to the current thesis is functional DNA that has targeting properties based on their three dimensional structure in solution, also common known as DNA aptamers. Aptamers are selected through a process known as Systematic Evolution of Ligands by Exponential Enrichment or SELEX. DNA aptamers have drawn a great deal of attention as the next generation antibody due to (1) lower development and production cost, (2) higher stability, (3) more simple to characterize and modify. With a growing library of aptamers with target specific interactions, some of the most exiting research is the development of next generation medical imaging and therapies based on aptamer functionalities, in combination with novel nanomaterials. In this thesis, we describe work introducing a new type of optically active nanoparticles, that exhibits useful properties for disease diagnosis and therapy while reducing unwanted side effects.

As the rest of the thesis will demonstrate in great detail, the future of DNA based nanotechnologies is tremendous, with the potential to impact electronics, optics, and medical devices of the future.

For my mom and dad, Jennifer, and Ah Bee.

Acknowledgements

To Professor Yi Lu, thank you for your patience, mentorship, and friendship. Our relationship developed a great deal over the course of my time in your lab and I feel I grew up under your watchful eye. Thank you for encouraging me to be better than what I thought I could be and always encouraging my imagination. You cultivated my love for science, showed me the meaning of dedication, and always brought me back down to earth.

I would also like to thank other members of my thesis committee, Dr. Paul Braun, Dr. Steve Granick, and Dr. Jianjun Cheng and their respective labs for contributing their valuable experience, intelligence and time. All of your suggestions and support are highly appreciated.

To former and current Lu lab members, thank you for the wonderful discussions, late nights, and great memories. Special thanks to Dr. Zidong Wang and Dr. Jung Heon Lee for your mentorship and advice. Thanks also to Dr. Tian Lan, Hang Xing, Li Huey Tan, and Kevin Hwang for your friendship, late night discussions, and help on experiments.

I gratefully acknowledge the help on my experiments from MRL-CMM and Beckman-ITG staff with special thanks to Dr. Scott Maclaren for your help and advice. My work has been sponsored by the NIH National Cancer Institute Alliance for Nanotechnology in Cancer ‘Midwest Cancer Nanotechnology Training Center’ Grant R25 CA154015A. Special thanks to Laura Miller for all your help during the program.

Lastly and mostly, I want to thank my mom and dad for all the sacrifices you have made and standing by me always, none of this would have been possible without all that you did for me.

TABLE OF CONTENTS

CHAPTER 1

INTRODUCTION

Portions of this chapter were published as "DNA aptamer functionalized nanomaterials for intracellular analysis, cancer cell imaging, and drug delivery" Hang Xing, Ngo Yin Wong, Yu Xiang, and Yi Lu, *Current Opinion in Chemical Biology* **2012**, 16, 429-435

1.1 Functional Nanomaterials and Their Emerging Applications

A material or object is considered "nanoscale" when one or more of the dimensions are between 1 and 100 nanometers. While absolute size definitions can be at times, arbitrary, the common theme uniting nanoscale materials and more specifically, functional nanomaterials is the emergence of unique size dependent properties that is not apparent when the material is treated as a bulk material. Interestingly, the properties of nanoscale materials has been explored since the 1800's when stained glass were infused with different sizes of colloidal gold to infuse a gold or red color. While these ancient explorations lacked the theory and technology to fully understand the properties of gold colloids, their work became the inspiration for generations of scientists since to develop and understand functional nanoscale materials for an ever growing list of applications, including electronics and photonics, to energy and catalysis, and the next generation of medical therapies that promises to be more effective, less invasive, while dramatically reducing side effects.

Over the last two decades, an area of particular interest and tremendous has been the development of functional nanomaterials such as metallic nanoparticles(1,2), semiconducting nanocrystals (quantum dots) (3-5), carbon nanotubes (6-8), nanorods (9),

and nanoshells (10,11), to only name a few.(12) These materials all exhibit unique properties (optical, electronic, and catalytic) due to their small size, effects that are often not observable at the bulk scale. Subsequently, these material properties have been exploited for a wide range of applications such as electronics, optics, energy storage, catalysis, sensing, cellular imaging, and biomedical procedures. (13-16)

Another important concept in nanotechnology is the assembly and patterning of nanomaterials such that the aggregate behavior of the assembly is different or exhibit enhancements over a single particle or an uncontrolled aggregate. Phenomenon such as Förester (Fluorescence) resonant energy transfer (FRET), plasmonic hotspots, and surface enhanced Raman spectroscopy (SERS) are all distance dependent mechanisms between two or more electronically active materials. FRET and SERS, in particular have found wide adoption for detailed, nanoscale characterization of proteins, as well as extremely sensitive detection of small molecules and proteins. Our ability to control these nanoscale assemblies will be critical to develop a deeper understanding of these interactions as well as allow the design and fabrication of functional devices to take advantage of these nanoscale effects.

1.2 Bottom-Up Manufacturing and Structural DNA Nanotechnology

To date, there are two major schools of thought regarding nanoscale patterning. The first is the “top-down” approach. This powerful concept has been and continues to be the basis of semiconductor processing techniques, where a bulk material (usually silicon) is patterned and etched to reveal ever shrinking nanoscale features. Since the bulk of the work is done through optical lithography, many speculated that the features sizes of such

nanoscale structures will be limited by the diffraction limit, often estimated by $\lambda/2$ where λ is the wavelength of the incident light. Many had speculated that this limitation would hold these "top-down" techniques to size features of roughly 200 nanometers (nm). However, continued advances in technology have allowed silicon processors to continue to push the feature size into the tens of nanometers. One major drawback of "top-down" fabrication techniques, however, is complexity and cost. As industrial companies continue to follow "Moore's law" into the tens of nanometers, the costs have correspondingly escalated dramatically with a modern semiconductor "Fab" now costing several billion dollars.

The other fundamental approach to nanoscale patterning is often referred to as "Bottom-Up" techniques. Rather than starting with a bulk material, bottom up techniques start with atoms and molecules and through specific interactions, assemble into larger, ordered structures. These techniques are often biology inspired, and rely on intermolecular forces or a biological template to self-assemble individual components into ordered one, two, and three dimensional structures. Bottom up techniques are intrinsically lower cost and less complex, but suffers from reproducibility as well as maintaining a high level of spatial control over a large area. But rather than competing on a "race to the bottom" with top down approaches, bottom up approaches are often complementary to top down methods and are often appropriate under a different set of scenarios where nanometer spatial control of heterogeneous materials, soft substrates, and biocompatibility are of importance. Some of the most commonly explored materials for bottom up, self-assembled structures are block-copolymers, peptide/proteins, and DNA.

The central dogma of biology states the role of deoxyribonucleic acids (DNA) is to make ribonucleic acids (RNA), which in turns, make proteins. However, the properties of DNA, when viewed through a materials scientist's eyes, becomes a biopolymer with predictable structure, programmable chemistry, nanometer resolution, good thermal and chemical stability, and double strand persistence length of roughly 50 nanometers. Professor Nedrian Seeman, in 1982, theorized that DNA, due to its repetitive nature and structural stability would be an ideal scaffold to create predictable and crystalline structures, which can be in turn, used to study difficult to crystallize proteins. As his website states today, "Ultimate goals for this approach include the rational synthesis of periodic matter and the assembly of a biochip computer. The reason for trying to synthesize periodic matter in a rational fashion is the weakness of the current crystallization protocol and the expectation that DNA sticky ends can be used to assemble DNA cages containing oriented guests. If we can achieve this goal, we will have a good handle on the crystallization of all biological molecules."

DNA is capable of forming sequence specific double helixes through base-pairing of complementary bases. In his 1982 seminal paper, Professor Seeman introduced the concept of what is to become structural DNA nanotechnology, by designing a series of branched structural motifs that mimicked naturally occurring DNA structures known as "Holliday junctions." In the subsequent decades, Professor Seeman and a growing cohort designed and created increasing robust and complex motifs, such as the double and triple crossover motifs that significantly increased the stability of a DNA structure. (17-19) Later, he and co-workers designed and generated much more complex DNA structures with variations of the double crossover motif, triple crossover motifs, two dimensional

lattices, and polyhedral DNA structures such as the cube, six-connected network, pentagonal dedecahedron and truncated octahedron. (20,21) Novel motifs are continuously being introduced, and recently, a half-crossover based structure was reported by Yin *et al.*, which allowed them to form DNA tubes composed of four-helix bundles all the way up to twenty-helix bundles. (22) In another work, Hansen *et al.* introduced a way to incorporate some features of both the origami method and the tile based self-assembly to produce weave tile structures. (23) They reported formation of flexible structures that were used to increase the anticoagulant activity of thrombin-binding aptamers. The structure was composed of two long strands that have complementarities for each other (woven strands) and possess the sticky ends that provide complementary sequences for other tiles to produce the lattices. Unlike the other tile based or origami methods, the weave tile structure does not form based on the holiday junctions or crossovers and just benefits from the exact design of the structure based on the geometry of the DNA bases. The new design solves the problem of incorrect strand stoichiometry that has been reported with other tile-based assemblies because this approach only uses two DNA strands.

The DNA tile based system has also been used to make 3D structures. The first tile based 3D DNA structure was introduced by Seeman. (24) However, the study only provided indirect evidence for the formation of the 3D structure. A few years later other studies reported the construction of 3D DNA structures. An interesting study by Shih *et al.* reported formation of an octahedron by self-folding of a 1.7 kb single-stranded DNA (heavy strand) and a few smaller strands (light strands). (25) This structure might be considered as an early example of the DNA origami technique. Another study by

Goodman *et al.* reported construction of a tetrahedron DNA structure. They have also reported conformational changes in the structure due to restriction enzyme digestions (26) or by strand displacement. (27) Formation of various 3D structures such as triangular, cubic, hexameric prisms was reported by Aldaye and Sleiman. (28) Another interesting study by He *et al.* reported the formation of tetrahedron, dodecahedron, buckyball structures (27) and a DNA octahedral structure. (29)

The addition of dynamic properties to DNA nanostructures is another practice which has been applied over the last decade. (30-34) One of the most often employed strategies to trigger and produce dynamics in DNA nanostructures is strand displacement, which is a process of displacing pre-hybridized strands (one or more) in a DNA complex (consisting of two or more strands) via partial or full hybridization with a new strand (usually called a displacement strand), with a longer region of complementarity. To start strand displacement, the displacement strand hybridizes a single-stranded complementary region in the DNA complex and by branch migration displaces the pre-hybridized strand. The single-stranded region in the initial complex is called a toehold. Toehold based strand displacement in DNA nanotechnology was initially proposed by Yurke *et al.*. (30) They demonstrated a nanodevice which switched from open to closed states and *vice versa* by multi step hybridization and strand displacement. Later, scientists have programmed the movement of DNA molecules based on toehold strand displacement. Shih and Pierce designed a DNA device driven by fuel strands on top of a DNA tube (31), among other DNA walker designs. (35-38) Recently, Wang *et al.* introduced a new strategy for stepwise walking of a bipedal walker, where the forward step is triggered by introducing Hg^{2+} and H^{+} ions while the backward step is triggered by OH^{-} ions and

cysteine. (39) Tile-based DNA nanostructure architecture is a promising method, but there are major drawbacks for the tile-based assembly strategy. First, the design of complex structures using the tile method is a challenge since one needs to design and check the new sequence for each step, which is a time consuming and problematic step. Secondly it is very hard to control production of complex high order nanostructures, and even though some of the structures have finite size and shape, many other structures such as arrays or grids grow as long as sticky strands are available, and therefore there is no control over size. Finally, in order to obtain the predicted structure the strands need to be highly quantitatively controlled.

The "DNA origami" method was first proposed and implemented by Paul W. K. Rothemund in 2006 (40), in which he folded a long viral single-stranded DNA (ssDNA) molecule to create DNA structures of arbitrary shapes. However, DNA origami was foreshadowed by at least two other prior works. In the first attempt, Yan *et al.* reported formation of the nano arrays by using a long scaffold and some shorter strands. (41) However, they could not demonstrate exact control over size and shape of the structures. Another advance, mentioned previously, was published by Shih *et al.* who reported formation of an octahedron by self-folding of a long single-stranded DNA and a few smaller strands. (25) Moreover, a long time ago Williamson suggested the term "RNA origami" for 3D structures that could be formed by self-folding of the RNA molecules. (42)

The term origami refers to the Japanese art of folding paper into a special, often complex shape. DNA origami, therefore, is so named since one long strand of DNA is folded to produce the desired structure by the help of smaller staple strands. The origami

folding process is based on folding of the large ssDNA (usually the 7.3 kilobase genome of the M13 bacteriophage) with an excess of smaller complementary strands (typically 32 bases). These small strands are called “staple” strands and are complementary to at least two distinct segments of the long ssDNA. Long ssDNA and an excess of staple strands are then heat-annealed in a specific buffer with high concentration of magnesium to form the origami.

The origami method has been applied to construct two dimensional and more recently three dimensional DNA nanostructures. In the first demonstration of the technique, Rothemund illustrated construction of many arbitrary structures such as stars, squares, rectangles, smiley faces, triangles and other complex structures. He also demonstrated the addressability of the structures by showing formation of designed patterns on the top of the origami tiles. Only a few months after Rothemund’s original origami work was published, a Chinese group reported construction of a map of china by this method. (43) In 2008 software to design arbitrary structures, called SARSE, was released (44), and it was rapidly followed by caDNAno, an improved tool for the design of 2D and 3D DNA origami (45). More recently, canDo (46), an online program to predict properties, such as flexibility and predicted final shape of designed structures, was developed by the Dietz group.

Very recently Endo *et al.* reported formation of multi-domain DNA origami by using origami four-way junctions (47), and in a very similar work Rajendran *et al.* reported construction of the multi-domain DNA origami. (48) The DNA origami method has been highly successful and popular since it does not require any sequence design,

time-consuming stoichiometry studies or control over the quality and quantity of the staple strands, which are main challenges in tile based DNA architecture.

DNA origami tiles have gained wide interest since they are effective platforms for the spatial dependent study of other systems. In the earliest work, patterns (hairpin dumbbells) on top of the origamies were imaged by AFM. (40) Since then, DNA origami has been used as a template for patterning using streptavidin molecules (49) and Shen *et al.* showed patterning of enhanced green fluorescent protein on top of the origami. (50) DNA origami tiles has also been used to investigate binding of thrombin molecules to their aptamers. (51)

Moreover, patterning of gold nanoparticles has been reported on the six-helix bundle DNA origami (52) and rectangular origami. (53) By placing fluorophores at specific positions of DNA origami as a ruler, calibration objects for super-resolution optical microscopy have been reported. (54) DNA origami nanotubes have been aligned between gold islands (55) and recently, Liu *et al.* reported gold metallization of branched DNA origami. (56)

In an interesting study, Manue *et al.* (57) showed positioning of single-walled carbon nanotubes on top of rectangular origami. They demonstrated stable field-effect transistor-like behavior of the structure, which is an important advance toward using a complex system of DNA and nanotubes toward applications in nanoelectronics. Eskelinen *et al.* positioned carbon nanotubes on top of the DNA origami by aid of interactions between streptavidin molecules and biotinylated DNA strands precisely positioned on the origami and wrapped around the carbon nanotube. (58) In another

major step toward wafer scale origami applications, DNA origamies have been placed and oriented on lithographically patterned surfaces thus combining the top-down and bottom-up approaches. (59) Furthermore, Hung *et al.* reported specific positioning of gold nanoparticles on top of lithographically confined DNA origamies. (60)

In a very interesting development, scientists from Hao Yan's and Erik Winfree's groups separately demonstrated molecular robots which move along a predefined path on top of a rectangular origami. (61) The movement of this walker is based on a simple enzymatic reaction. In another advance, Gu and colleagues from Seeman's group introduced a DNA walker molecule which moves on top of an origami in programmed path and collects cargos which are placed at specific positions on the origami. (62) In another study Wickham *et al*. programmed directed, uniform and continuous translation of a molecular motor along a 100 nm track on flat DNA origami. (63)

1.3 Introduction to Functional DNA

Chapter five of this thesis discusses the use of aptamer functionalized DNA mediated gold nanoflowers for simple imaging and diagnosis of diseased cells. Here, a brief introduction to functional DNA, targeted vs. passive uptake, as well as previous successes in aptamer/ gold systems for *in vitro* and *in vivo* applications will be discussed below.

As we have highlighted above, DNA is among the most important class of biopolymers and is known primarily as a carrier of genetic information. (64,65) Since the early 1990s, however, DNA sequences have been identified that perform catalytic reactions (called DNAzymes, or deoxyribozymes) (42,66) like protein enzymes, or

exhibit target specific binding (aptamers) very much similar to antibodies. (67) DNAzymes, aptamers and their combination (called aptazymes or allosteric DNAzymes) (68) are now collectively called functional DNA. These functional DNA molecules have not been discovered in nature thus far, instead they have been isolated via a combinatorial biology technique known as *in vitro* selection (69), or a process also known as systematic evolution of ligands by exponential enrichment (SELEX). (70,71)

A unique feature of functional DNA and related functional RNA molecules (ribozymes and RNA aptamers) is their ability to specifically bind a broad range of analytes including inorganic, organic, and biomolecules, as well as bacteria, viruses, and cancer cells. (72-74) The binding affinity of these functional DNA/RNA molecules to specific targets can rival that of protein antibodies. In addition to their ability to recognize the large variety of targets, functional DNAs offer a number of competitive advantages over other molecules such as antibodies. (75) First, functional DNAs are isolated by in vitro selection and can be chemically synthesized and engineered in a standard chemistry lab after their sequences are determined, whereas antibody preparation often requires animals or cell cultures. Second, functional DNAs are generally more stable under harsh conditions, such as high temperature and non-aqueous solvent that are often encountered during materials synthesis and engineering; if the DNA sequences become denatured, they are easily refolded to their native active conformation, while denatured antibodies usually cannot be recovered. Finally, these functional DNAs induce little or no immunogenicity in therapeutic applications compared to those protein antibodies. Despite these advantages, there is still a lack of general methods to transform the selective binding of these functional DNAs to physically detectable signals such as fluorescence or

colors. Therefore, integration of functional DNA with nanomaterials provides new hybrid systems that combine specific molecular recognition or catalytic properties of functional DNA with diverse and strong signal transduction of nanomaterials. This novel combination has yielded stimuli responsive nanomaterial assemblies and various types of sensors for selective and sensitive detection of a wide range of analytes. (76-80)

Aptamers, in particular, are short single stranded DNA or RNA sequences that have been selected and refined for highly specific binding to a target of interest by in vitro selection or systematic evolution of ligands by exponential enrichment (SELEX). (70,71,81) In the past two decades, the technology has evolved quickly and has since found particular interest in environmental sensing, cancer imaging/diagnosis, and disease therapy. (82-89) Due to its automated synthesis, high stability, and well established selection process, DNA aptamers have become one of the most promising techniques for introducing target specificity to nanomaterials for intracellular imaging, diagnosis, and therapy. (80,90) Additionally, aptamers (10-15 kDa) are generally smaller in size compared with antibodies (150 kDa) and single chain variable fragments (25 kDa) and therefore accumulates more quickly within tumor tissue.

1.4 Aptamer Functionalized Nanomaterials for Biomedical Applications

Metal nanoparticles have been used widely for the studies of cellular uptake and analysis due to their simple synthesis, easy modifications, and biocompatibility. For applications in cellular analysis, gold and silver nanoparticles have been especially common owing to their excellent plasmonic properties, which have enabled significant advances in localized surface plasmon resonance (LSPR) for applications such as surface

enhanced Raman spectroscopy. (91) When in close proximity to the surface of a plasmonic metal, the Raman signal can achieve 10^{14} enhancements, due to electromagnetic enhancements from plasmonic "hot spots". Nanoparticles (92), nanoshells (93), nanoflowers (94), nanorods (95), and many other nanostructures (96) therefore, have been recently been explored for their plasmonic properties in cell imaging, uptake mechanisms, and detection of various analytes. (97) The reader is directed to other recent reviews that focus on SERS/plasmonic applications of nanoparticles for cellular analysis. (98)

Other types of nanomaterials such as silica nanoparticles, quantum dots (QDs), and carbon based nanomaterials have also been applied in cellular applications. (99-101) Nanosized silica is widely known for excellent compatibility and has been used extensively in cellular studies. (102) More recently, mesoporous structures dramatically increased the surface area of silica nanoparticles and enabled high loading of cargo for cellular imaging and delivery. (103) Another material of interests is semiconducting QDs. Because of their fluorescence stability, board absorption and narrow emission band, they are uniquely suited for high resolution (104) and multiplex imaging of cells. (105) Carbon based nanomaterials such as carbon nanotubes, fullerenes, and most recently graphene and graphene oxide are also promising nanomaterials for cellular applications, including the use of stabilized graphene oxide in cellular imaging and drug delivery. (106-108)

The materials discussed above have all demonstrated good biocompatibility and an ability to achieve either some function in diagnostics, therapy, or both. One of the remaining challenges in nanomaterial based diagnostics and therapy is the idea of

transitioning from “passive targeting” to “active targeting” mechanisms. In passive targeting, nanoparticles tend to accumulate at tumor sites due to the enhanced permeation retention effect (EPR). Normal vasculature is impenetrable to molecules larger than 2 – 4 nanometers (nm), except for major organs such as the kidney, liver, and spleen. In contrast, tumor vasculatures tend to be “leaky” due to rapid, uncontrolled growth. As a result, tumors exhibit increased permeability to macromolecules and particles up to 600 nm. The EPR effect has been widely exploited to deliver nanoscale drug formulations to tumor sites, with successful clinical examples such as DaunoXome (liposomal daunorubicin; Gilead Sciences, Foster City, California, US) and Doxil (PEG-coated liposomal doxorubicin; Centocor Ortho Biotech, Ratitan, New Jersey, USA). Passive targeting is effective for nano-formulated therapeutics for tumor tissue, however, the therapeutic agents must be internalized into the tumor cell to exhibit any effectiveness. This uptake can be achieved by active targeting.

Active targeting takes advantage of specific proteins or other ligands that are over expressed specifically on the surface of tumor cells that differentiate diseased cells from normal, healthy cells. Therefore, active targeting is achieved by attaching a target recognition component to the nanocarrier or nanoparticle. Some of these targeting agents include albumin, FA, galactose, peptides (RGD, VEFT peptide), proteins, antibodies, and the focus of the below discussion, aptamers.

While there are many published examples of target specific aptamers, examples of aptamers that have found clinical relevance is expectedly far fewer. In particular the A10 RNA aptamer (a competitive inhibitor of prostate cancer tumor marker) and AS1411 aptamer (binds specifically to nucleolin protein, a nuclear protein overexpressed in the

cytoplasm and the surface of many cancer cells, such as human breast cancer cells) have found wide interest by researchers interested in targeted uptake of nanoparticles. Researchers have also addressed the specificity issues of targeting a single biomarker by conjugating several targeting ligands to enhance targeting specificity and signal sensitivity. Ko *et al.* (109) reported a multimodal nanoparticle that consisted of the AS1411 aptamer, TTA1 aptamer (binds to the extracellular matrix protein tenascin-C) and the RGD peptide (binds to integrin $\alpha_v\beta_3$). Aptamers have also been conjugated to gold nanoparticles (110-112), and super-paramagnetic iron oxide nanoparticles (113,114) to obtain enhanced imaging of tumor tissues. Additionally, when anti-cancer agents where incorporated with these targeted delivery platforms, it lead to greater antitumor activity.

1.5 Summary

As discussed above, oligonucleotides are a unique material with excellent predictability and reproducibility. By taking advantage of the innate nanoscale precision offered by the double helix, it has become one of the most promising scaffolding platforms being explored today. In the following chapters, this thesis describes recent work in advancing the applications of complex DNA nanostructures for the assembly of functional nanomaterials. By minimizing the interference to complex structures, we are able to demonstrate excellent spatial and orientation control of cargo attachment to simple as well as complex nanostructures, we also report the first successful decoration of the tile based DNA tetrahedron, as first reported by Mao et al. We also introduce a "new" conjugation chemistry that is likely to find wide adoption within nanotechnology. Using a biotin-analogue, we demonstrate the programmable and reversible conjugation of the

streptavidin to a DNA origami tile. By enabling multi-step conjugation, it is now possible to create dynamic and complex nanostructures. Finally, we explore the use of DNA mediated nanoflowers for simple imaging and diagnosis of diseased cells. Nanoflowers exhibit high optical scattering properties which are invulnerable to photo-degradation, non-toxic, and can be imaged using a standard light optical microscopy set, eliminating the need for advanced light sources and filters.

1.6 References

(1) Xia, Y.; Halas, N. J. *Mrs Bulletin* 2005, *30*, 338-348.

(2) Murray, J. B.; Scott, W. G. *J.Mol.Biol.* 2000, *296*, 33-41.

(3) Murray, C. B.; Norris, D. J.; Bawendi, M. G. *J. Am. Chem. Soc.* 1993, *115*, 8706-8715.

(4) Alivisatos, A. P. *Science* 1996, *271*, 933-937.

(5) Peng, X. G.; Manna, L.; Yang, W. D.; Wickham, J.; Scher, E.; Kadavanich, A.; Alivisatos, A. P. *Nature* 2000, *404*, 59-61.

(6) Iijima, S. *Nature* 1991, *354*, 56-58.

(7) Ajayan, P. M. *Chem. Rev.* 1999, *99*, 1787-1799.

(8) Dai, H. J. *Accounts Chem Res* 2002, *35*, 1035-1044.

(9) Xia, Y. N.; Yang, P. D.; Sun, Y. G.; Wu, Y. Y.; Mayers, B.; Gates, B.; Yin, Y. D.; Kim, F.; Yan, Y. Q. *Adv. Mater.* 2003, *15*, 353-389.

(10) Sun, Y.; Mayers, B.; Herricks, T.; Xia, Y. *Nano Lett.* 2003, *3*, 955-960.

(11) Balakrishnan, V. K.; Halasz, A.; Hawari, J. *Envir. Sci. Tech.* 2003, *37*, 1838-1843.

(12) Kharisov, B. I.; Kharissova, O. V.; Jose-Yacaman, M. *Ind. Eng. Chem. Res.* 2010, *49*, 8289-8309.

(13) Chan, W. C. W.; Maxwell, D. J.; Gao, X. H.; Bailey, R. E.; Han, M. Y.; Nie, S. M. *Curr. Opin. Biotech.* 2002, *13*, 40-46.

(14) Chen, X.; Mao, S. S. *Chem. Rev.* 2007, *107*, 2891-2959.

(15) Martin, C. R.; Kohli, P. *Nat. Rev. Drug Discov.* 2003, *2*, 29-37.

(16) Xia, Y.; Xiong, Y.; Lim, B.; Skrabalak, S. E. *Angew. Chem., Int. Ed.* 2009, *48*, 60-103.

(17) Fu, T. J.; Seeman, N. C. *Biochemistry* 1993, *32*, 3211-3220.

(18) LaBean, T. H.; Yan, H.; Kopatsch, J.; Liu, F. R.; Winfree, E.; Reif, J. H.; Seeman, N. C. *J. Am. Chem. Soc.* 2000, *122*, 1848-1860.

(19) Mao, C. D.; LaBean, T. H.; Reif, J. H.; Seeman, N. C. *Nature* 2000, *407*, 493-496.

(20) Seeman, N. C. *DNA Cell. Biol.* 1991, *10*, 475-486.

(21) Seeman, N. C. *Curr Opin Struc Biol* 1996, *6*, 519-526.

(22) Yin, P.; Hariadi, R. F.; Sahu, S.; Choi, H. M. T.; Park, S. H.; LaBean, T. H.; Reif, J. H. *Science* 2008, *321*, 824-826.

(23) Hansen, M. N.; Zhang, A. M.; Rangnekar, A.; Bompiani, K. M.; Carter, J. D.; Gothelf, K. V.; LaBean, T. H. *J. Am. Chem. Soc.* 2010, *132*, 14481-14486.

(24) Chen, J. H.; Seeman, N. C. *Nature* 1991, *350*, 631-633.

(25) Shih, W. M.; Quispe, J. D.; Joyce, G. F. *Nature* 2004, *427*, 618-621.

(26) Goodman, R. P.; Berry, R. M.; Turberfield, A. J. *Chem. Commun.* 2004, 1372-1373.

(27) Goodman, R. P.; Heilemann, M.; Doose, S.; Erben, C. M.; Kapanidis, A. N.; Turberfield, A. J. *Nat. Nanotechnol.* 2008, *3*, 93-96.

(28) Aldaye, F. A.; Sleiman, H. F. *J. Am. Chem. Soc.* 2007, *129*, 13376-+.

(29) He, Y.; Su, M.; Fang, P.-a.; Zhang, C.; Ribbe, A. E.; Jiang, W.; Mao, C. *Angew. Chem. Int. Edit.* 2010, *49*, 748-751.

(30) Yurke, B.; Turberfield, A. J.; Mills, A. P.; Simmel, F. C.; Neumann, J. L. *Nature* 2000, *406*, 605-608.

(31) Shin, J. S.; Pierce, N. A. *J. Am. Chem. Soc.* 2004, *126*, 10834-10835.

(32) Yin, P.; Yan, H.; Daniell, X. G.; Turberfield, A. J.; Reif, J. H. *Angew. Chem. Int. Edit.* 2004, *43*, 4906-4911.

(33) Jungmann, R.; Steinhauer, C.; Scheible, M.; Kuzyk, A.; Tinnefeld, P.; Simmel, F. C. *Nano Lett.* 2010, *10*, 4756-4761.

(34) Sannohe, Y.; Endo, M.; Katsuda, Y.; Hidaka, K.; Sugiyama, H. *J. Am. Chem. Soc.* 2010, *132*, 16311-16313.

(35) Bath, J.; Green, S. J.; Turberfield, A. J. *Angew. Chem. Int. Edit.* 2005, *44*, 4358-4361.

(36) Omabegho, T.; Sha, R.; Seeman, N. C. *Science* 2009, *324*, 67-71.

(37) Sherman, W. B.; Seeman, N. C. *Nano Lett.* 2004, *4*, 1203-1207.

(38) Tian, Y.; He, Y.; Chen, Y.; Yin, P.; Mao, C. D. *Angew. Chem. Int. Edit.* 2005, *44*, 4355-4358.

(39) Wang, Z.-G.; Elbaz, J.; Willner, I. *Nano Lett.* 2011, *11*, 304-309.

(40) Rothemund, P. W. K. *Nature* 2006, *440*, 297-302.

(41) Yan, H.; LaBean, T. H.; Feng, L. P.; Reif, J. H. *Proc. Natl. Acad. Sci. U. S. A.* 2003, *100*, 8103-8108.

(42) Breaker, R. R.; Joyce, G. F. *Chem. Biol.* 1994, *1*, 223-9.

(43) Qian, L.; Wang, Y.; Zhang, Z.; Zhao, J.; Pan, D.; Zhang, Y.; Liu, Q.; Fan, C.; Hu, J.; He, L. *Chinese Sci. Bull.* 2006, *51*, 2973-2976.

(44) Andersen, E. S.; Dong, M.; Nielsen, M. M.; Jahn, K.; Lind-Thomsen, A.; Mamdouh, W.; Gothelf, K. V.; Besenbacher, F.; Kjems, J. *ACS Nano* 2008, *2*, 1213-1218.

(45) Douglas, S. M.; Marblestone, A. H.; Teerapittayanon, S.; Vazquez, A.; Church, G. M.; Shih, W. M. *Nucleic Acids Res.* 2009, *37*, 5001-5006.

(46) Castro, C. E.; Kilchherr, F.; Kim, D.-N.; Shiao, E. L.; Wauer, T.; Wortmann, P.; Bathe, M.; Dietz, H. *Nat Methods* 2011, *8*, 221-229.

(47) Endo, M.; Sugita, T.; Rajendran, A.; Katsuda, Y.; Emura, T.; Hidaka, K.; Sugiyama, H. *Chem. Commun.* 2011, *47*, 3213-3215.

(48) Rajendran, A.; Endo, M.; Katsuda, Y.; Hidaka, K.; Sugiyama, H. *ACS Nano* 2011, *5*, 665-671.

(49) Kuzuya, A.; Kimura, M.; Numajiri, K.; Koshi, N.; Ohnishi, T.; Okada, F.; Komiyama, M. *ChemBioChem* 2009, *10*, 1811-1815.

(50) Shen, W.; Zhong, H.; Neff, D.; Norton, M. L. *J. Am. Chem. Soc.* 2009, *131*, 6660-+.

(51) Rinker, S.; Ke, Y.; Liu, Y.; Chhabra, R.; Yan, H. *Nat. Nanotechnol.* 2008, *3*, 418-422.

(52) Stearns, L. A.; Chhabra, R.; Sharma, J.; Liu, Y.; Petuskey, W. T.; Yan, H.; Chaput, J. C. *Angew. Chem. Int. Edit.* 2009, *48*, 8494-8496.

(53) Sharma, J.; Chhabra, R.; Andersen, C. S.; Gothelf, K. V.; Yan, H.; Liu, Y. *J. Am. Chem. Soc.* 2008, *130*, 7820-+.

(54) Steinhauer, C.; Jungmann, R.; Sobey, T. L.; Simmel, F. C.; Tinnefeld, P. *Angew. Chem. Int. Edit.* 2009, *48*, 8870-8873.

(55) Ding, B.; Wu, H.; Xu, W.; Zhao, Z.; Liu, Y.; Yu, H.; Yan, H. *Nano Lett.* 2010, *10*, 5065-5069.

(56) Liu, J.; Geng, Y.; Pound, E.; Gyawali, S.; Ashton, J. R.; Hickey, J.; Woolley, A. T.; Harb, J. N. *ACS Nano* 2011, *5*, 2240-2247.

(57) Maune, H. T.; Han, S.-p.; Barish, R. D.; Bockrath, M.; Goddard, W. A., III; Rothemund, P. W. K.; Winfree, E. *Nat. Nanotechnol.* 2010, *5*, 61-66.

(58) Eskelinen, A.-P.; Kuzyk, A.; Kaltiaisenaho, T. K.; Timmermans, M. Y.; Nasibulin, A. G.; Kauppinen, E. I.; Torma, P. *Small* 2011, *7*, 746-750.

(59) Kershner, R. J.; Bozano, L. D.; Micheel, C. M.; Hung, A. M.; Fornof, A. R.; Cha, J. N.; Rettner, C. T.; Bersani, M.; Frommer, J.; Rothemund, P. W. K.; Wallraff, G. M. *Nat. Nanotechnol.* 2009, *4*, 557-561.

(60) Hung, A. M.; Micheel, C. M.; Bozano, L. D.; Osterbur, L. W.; Wallraff, G. M.; Cha, J. N. *Nat. Nanotechnol.* 2010, *5*, 121-126.

(61) Lund, K.; Manzo, A. J.; Dabby, N.; Michelotti, N.; Johnson-Buck, A.; Nangreave, J.; Taylor, S.; Pei, R.; Stojanovic, M. N.; Walter, N. G.; Winfree, E.; Yan, H. *Nature* 2010, *465*, 206-210.

(62) Gu, H.; Chao, J.; Xiao, S.-J.; Seeman, N. C. *Nature* 2010, *465*, 202-U86.

(63) Wickham, S. F. J.; Endo, M.; Katsuda, Y.; Hidaka, K.; Bath, J.; Sugiyama, H.; Turberfield, A. J. *Nat. Nanotechnol.* 2011, *6*, 166-169.

(64) Storhoff, J. J.; Mirkin, C. A. *Chem. Rev.* 1999, *99*, 1849-1862.

(65) Seeman, N. C. *Nature* 2003, *421*, 427-431.

(66) Breaker, R. R. *Nat.Biotechnol.* 1997, *15*, 427-431.

(67) Wilson, D. S.; Szostak, J. W. *Annu. Rev. Biochem.* 1999, *68*, 611-647.

(68) Robertson, M. P.; Ellington, A. D. *Nat.Biotechnol.* 1999, *17*, 62-66.

(69) Robertson, D. L.; Joyce, G. F. *Nature (London)* 1990, *344*, 467-468.

(70) Tuerk, C.; Gold, L. *Science* 1990, *249*, 505-510.

(71) Ellington, A. D.; Szostak, J. W. *Nature* 1990, *346*, 818-822.

(72) Li, J.; Lu, Y. *J. Am. Chem. Soc.* 2000, *122*, 10466-10467.

(73) Lu, Y.; Liu, J. *Curr. Opin. Biotech.* 2006, *17*, 580-588.

(74) Navani, N. K.; Li, Y. F. *Curr. Opin. Chem. Biol.* 2006, *10*, 272-281.

(75) O'Sullivan, C. K. *Anal. Bioanal. Chem.* 2002, *372*, 44-48.

(76) Liu, J. W.; Lu, Y. *J. Am. Chem. Soc.* 2003, *125*, 6642-6643.

(77) Lee, J. H.; Wang, Z. D.; Liu, J. W.; Lu, Y. *J. Am. Chem. Soc.* 2008, *130*, 14217-14226.

(78) Wang, Z. D.; Lee, J. H.; Lu, Y. *Adv. Mater.* 2008, *20*, 3263-3267.

(79) Zhao, W. A.; Chiuman, W.; Lam, J. C. F.; McManus, S. A.; Chen, W.; Cui, Y. G.; Pelton, R.; Brook, M. A.; Li, Y. F. *J. Am. Chem. Soc.* 2008, *130*, 3610-3618.

(80) Wang, Z. D.; Lu, Y. *J. Mater. Chem* 2009, *19*, 1788-1798.

(81) Beaudry, A. A.; Joyce, G. F. *Science* 1992, *257*, 635-641.

(82) Lu, Y.; Liu, J. W. *Accounts Chem Res* 2007, *40*, 315-323.

(83) Willner, I.; Zayats, M. *Angew. Chem. Int. Edit.* 2007, *46*, 6408-6418.

(84) Zhao, W.; Ali, M. M.; Brook, M. A.; Li, Y. *Angew. Chem. Int. Edit.* 2008, *47*, 6330-6337.

(85) Cho, E. J.; Lee, J. W.; Ellington, A. D. *Annu. Rev. Anal. Chem.* 2009, *2*, 241-264.

(86) Fang, X. H.; Tan, W. H. *Accounts Chem Res* 2010, *43*, 48-57.

(87) Li, D.; Song, S.; Fan, C. *Accounts Chem Res* 2010, *43*, 631-641.

(88) Lubin, A. A.; Plaxco, K. W. *Accounts Chem Res* 2010, *43*, 496-505.

(89) Oh, S. S.; Plakos, K.; Lou, X. H.; Xiao, Y.; Soh, H. T. *Proc. Natl. Acad. Sci. U. S. A.* 2010, *107*, 14053-14058.

(90) Liu, J. W.; Cao, Z. H.; Lu, Y. *Chem. Rev.* 2009, *109*, 1948-1998.

(91) Sathuluri, R. R.; Yoshikawa, H.; Shimizu, E.; Saito, M.; Tamiya, E. *Plos One* 2011, *6*.

(92) Ando, J.; Fujita, K.; Smith, N. I.; Kawata, S. *Nano Lett.* 2011, *11*, 5344-5348.

(93) Garrett, N.; Whiteman, M.; Moger, J. *Opt Express* 2011, *19*, 17563-17574.

(94) Wang, Z. D.; Zhang, J. Q.; Ekman, J. M.; Kenis, P. J. A.; Lu, Y. *Nano Lett.* 2010, *10*, 1886-1891.

(95) Jung, Y.; Reif, R.; Zeng, Y. G.; Wang, R. K. *Nano Lett.* 2011, *11*, 2938-2943.

(96) Bartczak, D.; Muskens, O. L.; Nitti, S.; Sanchez-Elsner, T.; Millar, T. M.; Kanaras, A. G. *Small* 2012, *8*, 122-130.

(97) Ding, C. F.; Qian, S. W.; Wang, Z. F.; Qu, B. *Anal. Biochem.* 2011, *414*, 84-87.

(98) Bantz, K. C.; Meyer, A. F.; Wittenberg, N. J.; Im, H.; Kurtulus, O.; Lee, S. H.; Lindquist, N. C.; Oh, S. H.; Haynes, C. L. *Phys. Chem. Chem. Phys.* 2011, *13*, 11551-11567.

(99) Ma, N.; Yang, J.; Stewart, K. M.; Kelley, S. O. *Langmuir* 2007, *23*, 12783-12787.

(100) Ma, N.; Tikhomirov, G.; Kelley, S. O. *Accounts Chem Res* 2010, *43*, 173-180.

(101) Park, H. S.; Kim, C.; Lee, H. J.; Choi, J. H.; Lee, S. G.; Yun, Y. P.; Kwon, I. C.; Lee, S. J.; Jeong, S. Y.; Lee, S. C. *Nanotechnology* 2010, *21*.

(102) Cai, Z. W.; Ye, Z. M.; Yang, X. W.; Chang, Y. L.; Wang, H. F.; Liu, Y. F.; Cao, A. N. *Nanoscale* 2011, *3*, 1974-1976.

(103) Liu, Y. T.; Mi, Y.; Zhao, J.; Feng, S. S. *Int J Pharmaceut* 2011, *421*, 370-378.

(104) Pinaud, F.; Clarke, S.; Sittner, A.; Dahan, M. *Nat Methods* 2010, *7*, 275-285.

(105) Stasiuk, G. J.; Tamang, S.; Imbert, D.; Poillot, C.; Giardiello, M.; Tisseyre, C.; Barbier, E. L.; Fries, P. H.; de Waard, M.; Reiss, P.; Mazzanti, M. *ACS Nano* 2011, *5*, 8193-8201.

(106) Peng, C.; Hu, W. B.; Zhou, Y. T.; Fan, C. H.; Huang, Q. *Small* 2010, *6*, 1686-1692.

(107) Liu, K. P.; Zhang, J. J.; Cheng, F. F.; Zheng, T. T.; Wang, C. M.; Zhu, J. J. *J. Mater. Chem* 2011, *21*, 12034-12040.

(108) Hong, B. J.; Compton, O. C.; An, Z.; Eryazici, I.; Nguyen, S. T. *ACS Nano* 2012, *6*, 63-73.

(109) Ko, M. H.; Kim, S.; Kang, W. J.; Lee, J. H.; Kang, H.; Moon, S. H.; Hwang, D. W.; Ko, H. Y.; Lee, D. S. *Small* 2009, *5*, 1207-1212.

(110) Javier, D. J.; Nitin, N.; Levy, M.; Ellington, A.; Richards-Kortum, R. *Bioconjugate Chem.* 2008, *19*, 1309-1312.

(111) Huang, C. C.; Chiu, S. H.; Huang, Y. F.; Chang, H. T. *Anal. Chem.* 2007, *79*, 4798-4804.

(112) Kim, D.; Jeong, Y. Y.; Jon, S. *ACS Nano* 2010, *4*, 3689-3696.

(113) Wang, Y. X. J.; Hussain, S. M.; Krestin, G. P. *Eur. Radiol.* 2001, *11*, 2319-2331.

(114) Wang, A. Z.; Bagalkot, V.; Vasilliou, C. C.; Gu, F.; Alexis, F.; Zhang, L.; Shaikh, M.; Yuet, K.; Cima, M. J.; Langer, R.; Kantoff, P. W.; Bander, N. H.; Jon, S. Y.; Farokhzad, O. C. *ChemMedChem* 2008, *3*, 1311-1315.

(115) Zadegan, R. M.; Norton, M. L. *International Journal of Molecular Sciences* 2012, *13*, 7149-7162.

(116) Fu, J. L.; Liu, M. H.; Liu, Y.; Yan, H. *Accounts Chem Res* 2012, *45*, 1215-1226.

(117) Rajendran, A.; Endo, M.; Sugiyama, H. *Angew. Chem. Int. Edit.* 2012, *51*, 874-890.

(118) Ke, Y.; Lindsay, S.; Chang, Y.; Liu, Y.; Yan, H. *Science* 2008, *319*, 180-183.

(119) Fu, J. L.; Liu, M. H.; Liu, Y.; Woodbury, N. W.; Yan, H. *J. Am. Chem. Soc.* 2012, *134*, 5516-5519.

(120) Zhao, Z.; Liu, Y.; Yan, H. *Organic & biomolecular chemistry* 2013, *11*, 596-8.

(121) Wang, R. S.; Nuckolls, C.; Wind, S. J. *Angew. Chem. Int. Edit.* 2012, *51*, 11325-11327.

(122) Pal, S.; Deng, Z. T.; Ding, B. Q.; Yan, H.; Liu, Y. *Angew. Chem. Int. Edit.* 2010, *49*, 2700-2704.

(123) Ke, Y. G.; Douglas, S. M.; Liu, M. H.; Sharma, J.; Cheng, A. C.; Leung, A.; Liu, Y.; Shih, W. M.; Yan, H. *J. Am. Chem. Soc.* 2009, *131*, 15903-15908.

(124) Han, D. R.; Pal, S.; Nangreave, J.; Deng, Z. T.; Liu, Y.; Yan, H. *Science* 2011, *332*, 342-346.

(125) Ke, Y. G.; Ong, L. L.; Shih, W. M.; Yin, P. *Science* 2012, *338*, 1177-1183.

(126) Jean-Philippe J. Sobczak, T. G. M., Thomas Gerling, Hendrik Dietz *Science* 2012, *338*, 1458-1461.

(127) Xia, Y.; Xiong, Y.; Lim, B.; Skrabalak, S. E. *Angew. Chem. Int. Edit.* 2009, *48*, 60-103.

(128) Wang, Y.; Li, Z. H.; Hu, D. H.; Lin, C. T.; Li, J. H.; Lin, Y. H. *J. Am. Chem. Soc.* 2010, *132*, 9274-9276.

(129) Chen, L. Q.; Xiao, S. J.; Peng, L.; Wu, T.; Ling, J.; Li, Y. F.; Huang, C. Z. *J. Phys. Chem. B* 2010, *114*, 3655-3659.

(130) Hwang, D. W.; Ko, H. Y.; Lee, J. H.; Kang, H.; Ryu, S. H.; Song, I. C.; Lee, D. S.; Kim, S. *J Nucl Med* 2010, *51*, 98-105.

(131) Li, L.-L.; Yin, Q.; Cheng, J.; Lu, Y. *Advanced healthcare materials* 2012, *1*, 567-72.

1.7 Figures

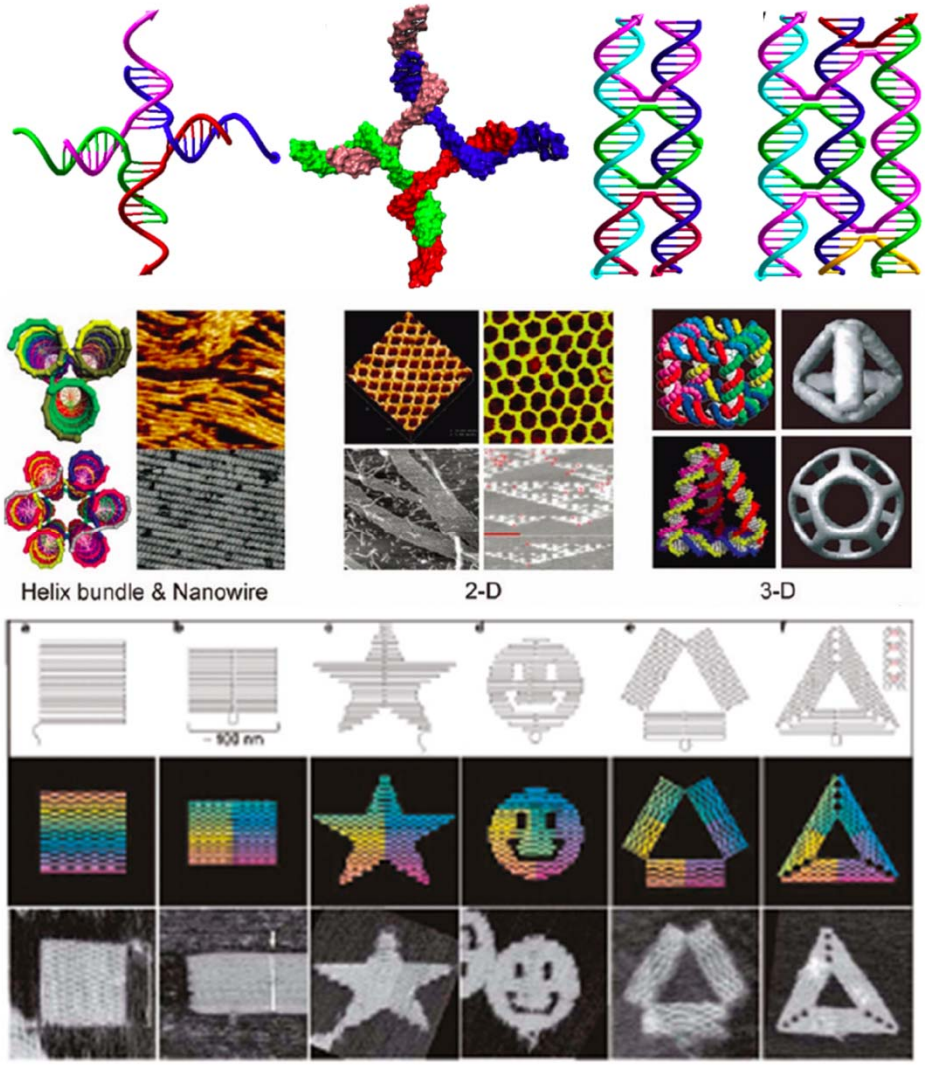

Figure 1.1 Schematic representations of (Top) 4 arm motif, double crossover (DX), and triple crossover (TX). (Middle) Design and corresponding AFM images of DNA helix, 2D crystals, and 3D shapes based on DNA tile designs. (Bottom) Design and corresponding AFM images of origami tiles as first described by Rothemund. Adapted from reference (40,115,116)

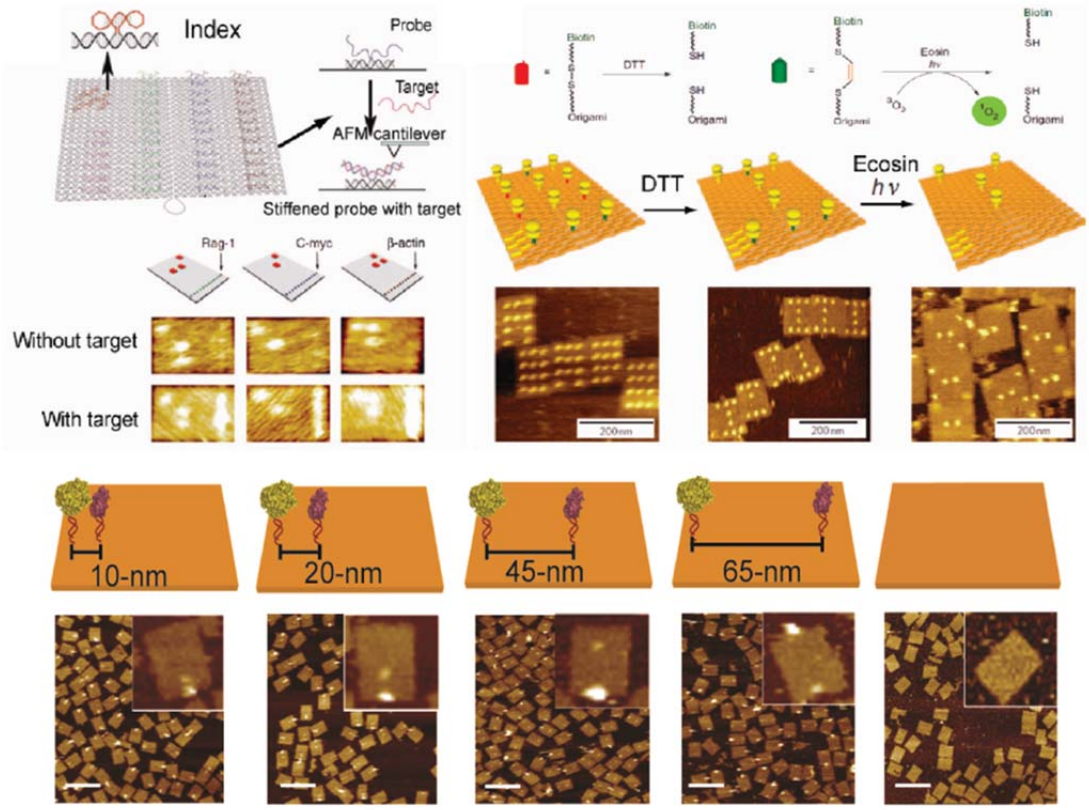

Figure 1.2 Recent examples of functionalized DNA origami tiles. (A) RNA and RNA hybridization origami "barcodes" for diagnostics and detection of oligonucleotides and proteins in solution. (B) Characterization of different single molecule reactions on origami tiles by atomic force microscopy. (C) Spatial control of two enzymes (glucose oxidase and horse radish peroxidase) to tune the enzymatic cascade reaction rate. The spatial control is further characterized by AFM and the rate of product production. Adapted from reference (117-119)

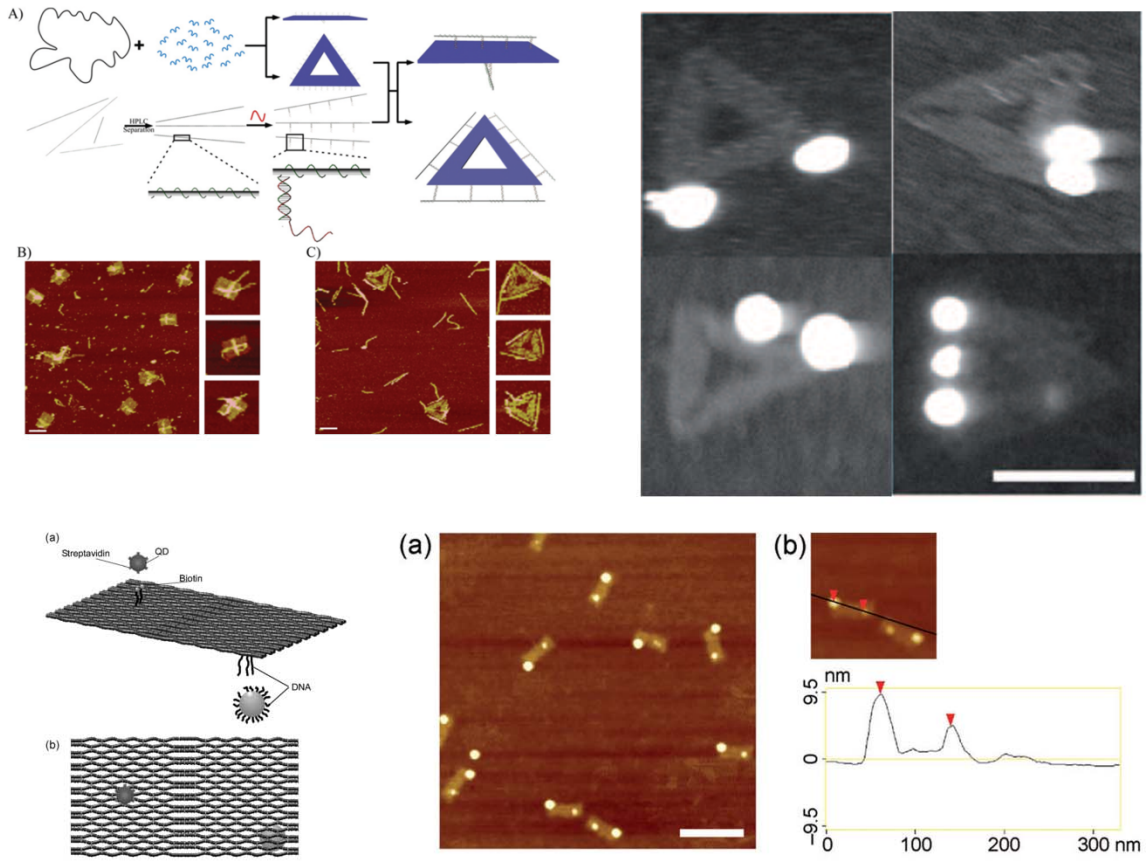

Figure 1.3 DNA origami tiles decorated with functional nanomaterials. (A) Origami directed assembly of carbon nanotubes, characterized by AFM. (B) TEM micrographs of origami directed assembly of silver nanopartilces. (C) AFM images of origami directed heterogeneous assembly of quantum dots and gold nanoparticles. Adapted from reference (120-122).

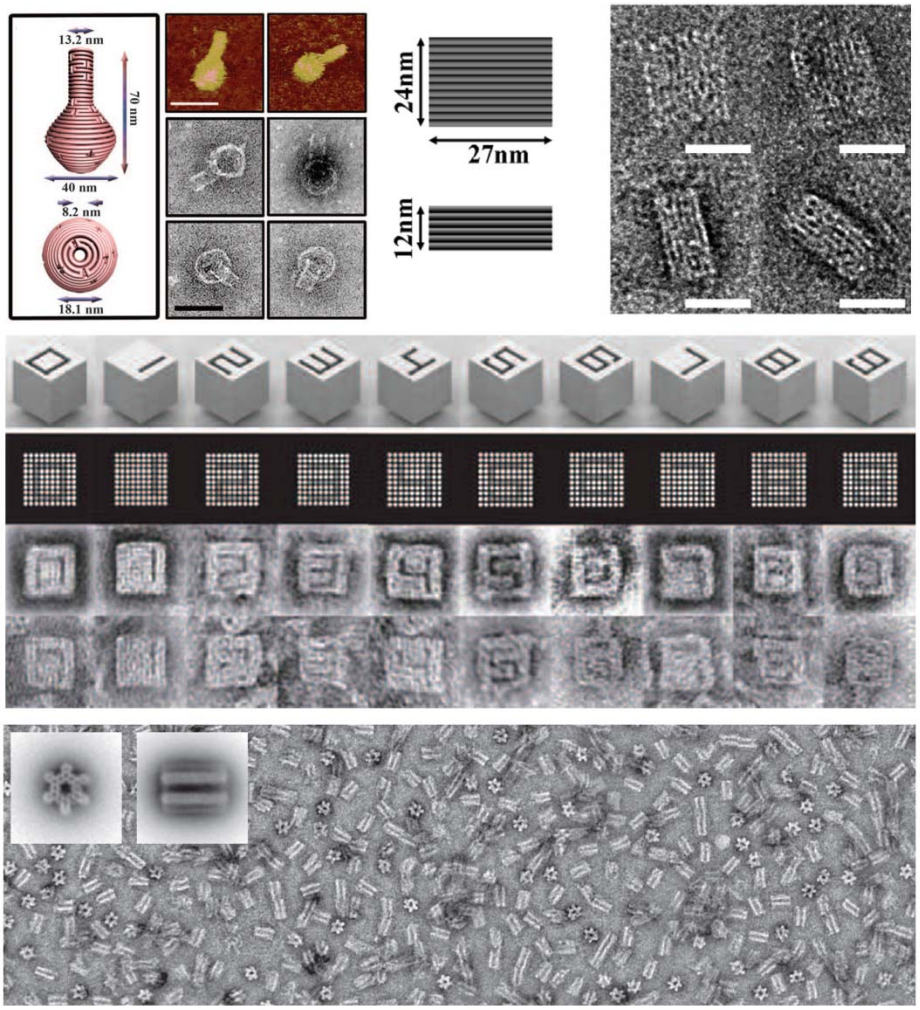

Figure 1.4 Three dimensional origami scaffolds. (A) AFM and TEM characterization of origami vessles with complex geometries. (B) Origami folded onto a square lattice. (C) "Lego like" orimgai bricks forming a large library of arbitrary three dimensional shapes. (D) High yield of three dimensional origami structures by annealing at a constant temperature over a short period of time. Adapted from reference (123-126).

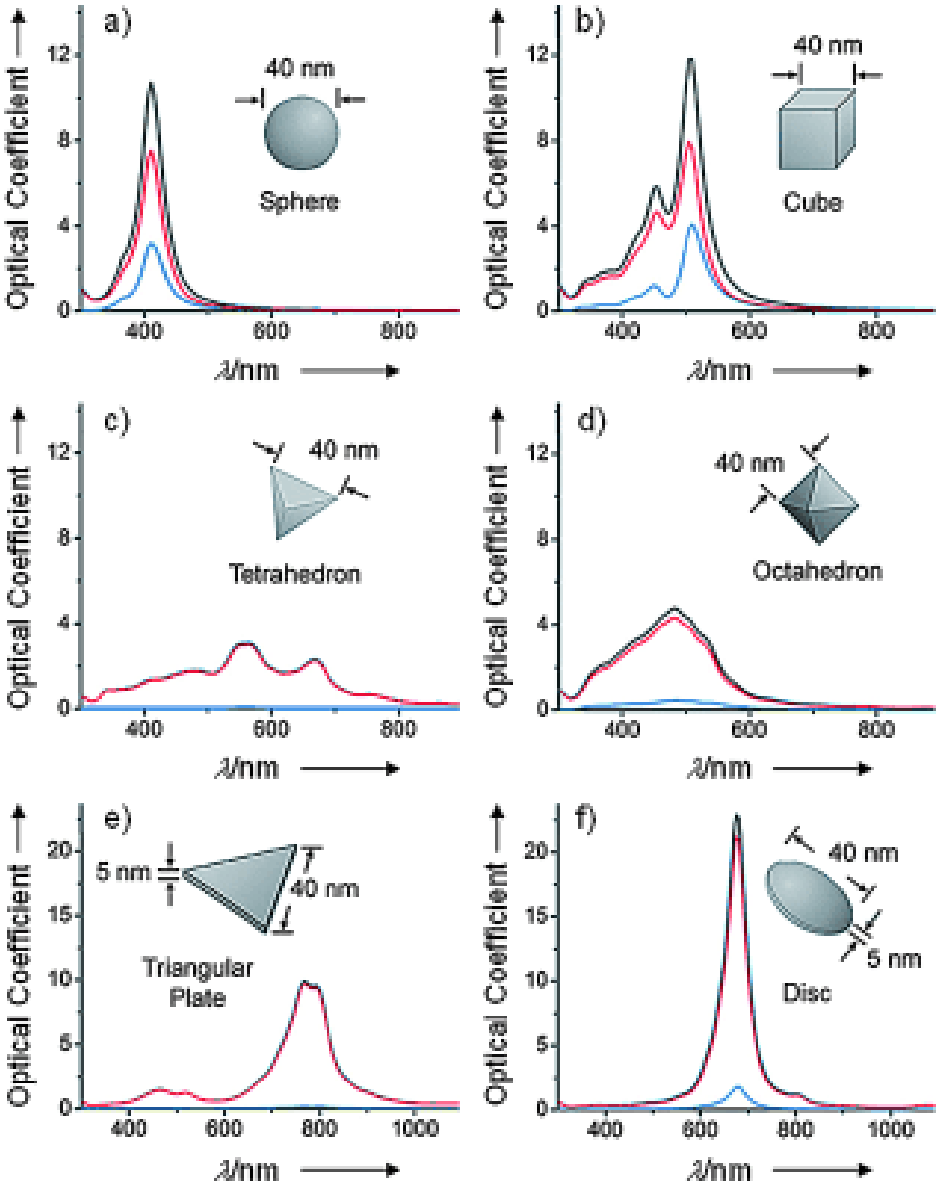

Figure 1.5 Calculated UV-visible extinction (black), absorption (red), and scattering spectra (blue) of Ag nanocrystal in various shapes. (A) Sphere, (B) cube, (C) tetrahedron, (D) octahedron, (E) triangular plate, (F) disc. Adapted from reference (127).

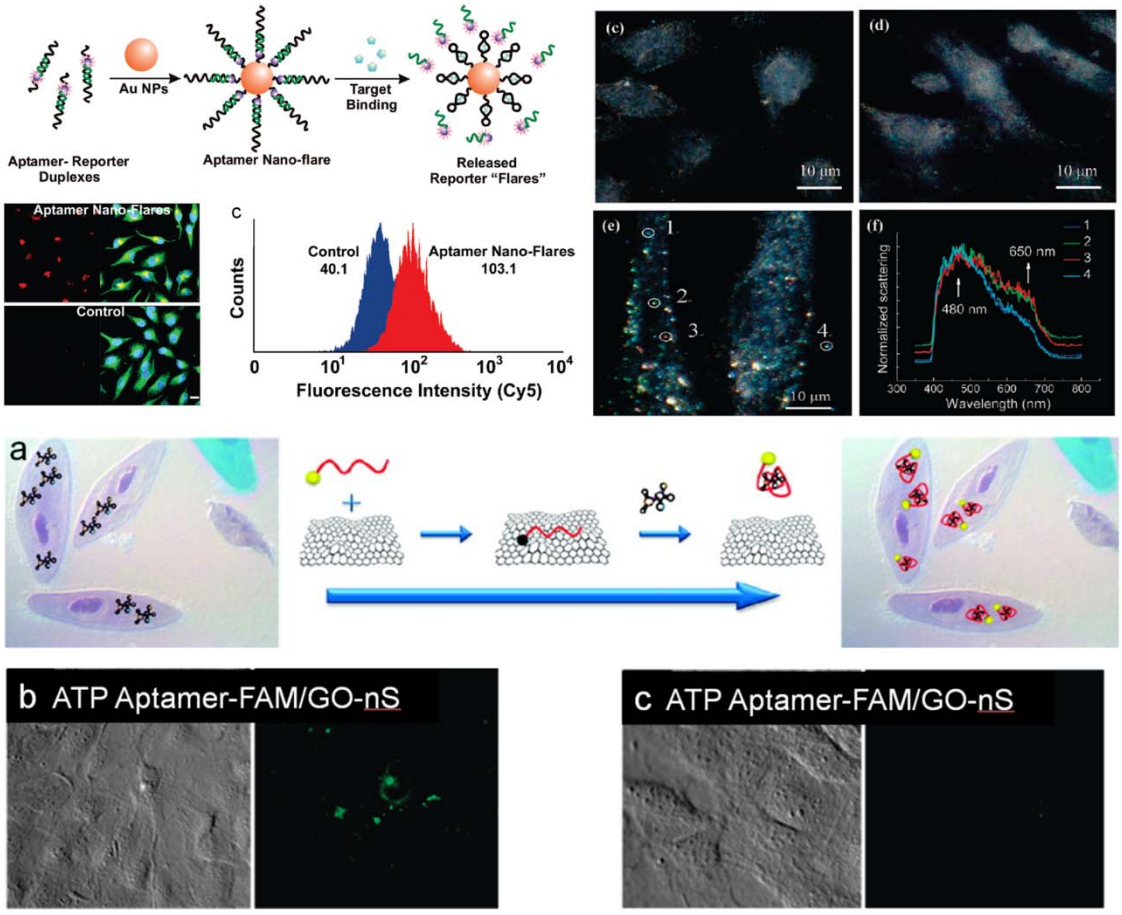

Figure 1.6 Various demonstrations of aptamer functionalized nanomaterials for directed uptake by cancer cells. (A) "Nano-flares" are highly stable DNA functionalized gold nanoparticles, used here to deliver a fluorescent probe to the target cell. (B) Highly scattering, aptamer functionalized silver nanoparticles uptaken and imaged by dark field microscopy. (C) Directed cellular uptake of aptamer functionalized graphene oxide nanosheets (GO-nS). Adapted from references (128,129).

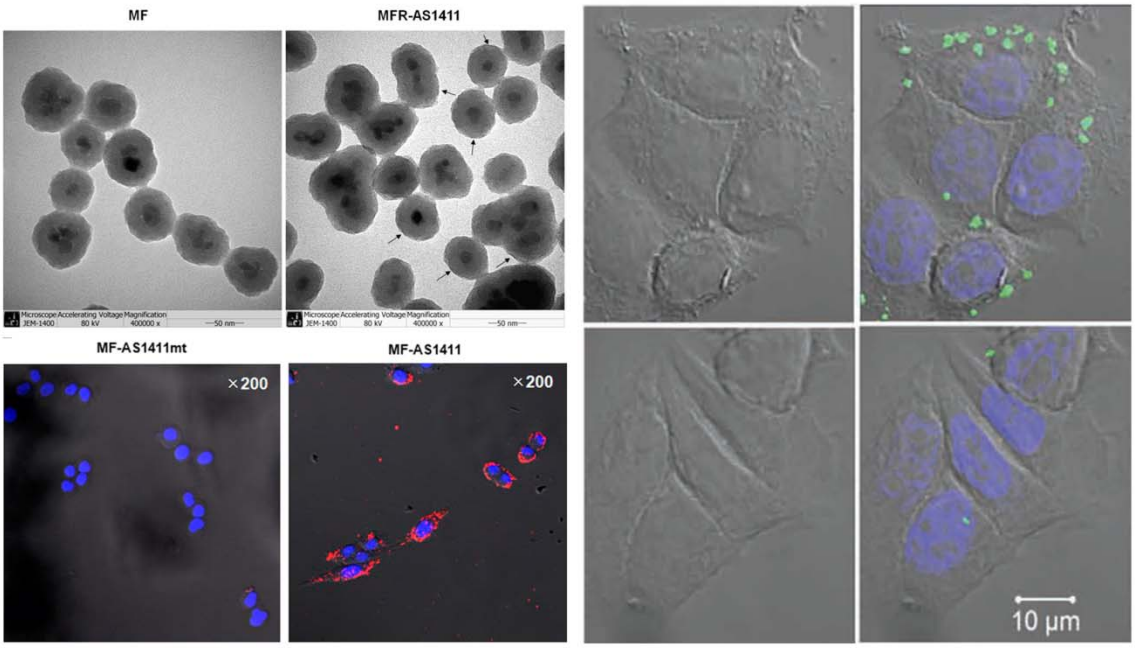

Figure 1.7 Targeted uptake of functional nanomaterials for multimodal imaging. (Left) Aptamer functionalized nanoparticles for multimodal imaging of human breast cancer cells. (Right) Mesoporous silica nanoparticles decorated with DNA aptamer for targeted uptake by cancer cells with potential to deliver anti-cancer agents. Adapted from reference (130,131)

CHAPTER 2

PHOSPHOROTHIOATE MODIFIED DNA FOR SITE SPECIFIC AND NANOSCALE 1D HETEROGENEOUS ASSEMBLY

Portions of this chapter were published as "Controlled Alignment of Multiple Proteins and Nanoparticles with Nanometer Resolution via Backbone Modified Phosphorothioate DNA and Bifucntional Linkers" Jung Heon Lee, Ngo Yin Wong, Li Huey Tan, Zidong Wang, and Yi Lu, *Journal of the American Chemical Society* **2010**, 132, 8906 – 8908. Portions of this chapter were published as "Site-Specific Control of Distances between Gold Nanoparticles Using Phosphorothioate Anchors on DNA and a Short Bifunctional Molecular Fastener" Jung Heon Lee, Daryl P. Wernette, Mehmet V. Yigit, Juewen Liu, Zidong Wang, and Yi Lu, *Angewandte Chemie International Edition* **2007**, 46, 9006-9010

2.1 Introduction

The heterogeneous assembly of nanomaterials to form functional complexes represents a significant and rewarding challenge with potential applications in electronics, photonics, and medicine. While progress on synthesizing functional nanomaterials with well-defined properties, excellent control, and good reproducibility have yielded a growing library of nanomaterials, it is unlikely these materials will find wide applicability by themselves. Instead, the promise of nanotechnology lies within the ability to combine different materials and functions that complement each other in such a way that a complete device can be assembled. To that end, traditional top-down lithography techniques fall short as it is difficult to produce structures that are capable of assembling

heterogeneous materials that have been synthesized. Instead, nanoscience has exploited many ways of "self-assembly" techniques to build scaffolds of various complexity, size, and control. The basic principle of self-assembly is to take advantage of existing and well understood interactions, such as van der Waals forces, hydrophobic/hydrophilic interactions, hydrogen bonds, and covalent bonds to predictably control the assembly of a final structure.

In the early 1950s, a team of researchers revealed for the first time the double helix nature of DNA. Soon, the details of Watson-Crick base pairing, as well as the many different structures of DNA were revealed through detailed analysis. It is now known that the double helix is formed by two anti-parallel strands which hybridize through Watson-Crick base pairing and base stacking. Structurally, the most common form of DNA under cellular and biological conditions is B-form DNA, characterized by a double helical structure with a pitch of 3.4 nanometers, a radius of 1 nanometer, 0.34 nanometers per nucleotide, and 10.5 bases to form a complete rotation of the helix. While the biological role of DNA is complex, its main function is the storage and transfer of genetic material, an idea summarized by the basic dogma of biology which tells us that "DNA makes RNA makes proteins." But with the advances in artificial DNA synthesis techniques over the past two decades, labs and companies are now able to synthesize short DNA strands (up to roughly 100 base pairs) of arbitrary sequence via a solid synthesis technique where each base is added to a growing strand in a step wise manner. These capabilities have enabled materials scientists and other non-biologist to look at DNA as a biopolymer with unique and desirable features for self-assembly applications. As a building material, DNA can be treated as both a rigid material (the persistence length of a double stranded

DNA is roughly 50 nanometers, where persistence length (P) is a measurement of stiffness of a polymer and at lengths below the persistence length, a polymer can be treated as a flexible elastic rod) or highly flexible (as a single stranded DNA). Additionally, extensive work has contributed to a vast and growing library of commerically available non-natural nucleotides that can incorporate novel functionalities. One of the largest collections of modified bases can be found at http://www.glenresearch.com and commercially synthesized oligos can be purchased from http://www.idtdna.com and http://www.trilinkbiotech.com. These functionalities include conjugation/ligation chemistries, photo-liable groups, as well as protection groups that increase the stability of DNA in the presence of endo- and exo- nucleases. The ability to control intra-strand chemistry on a base-by-base basis offers true nanoscale manipulation with a theoretical resolution of 0.34 nanometers.

With well-defined structural characteristics, a vast library of chemical modifications and unnatural bases, and a simple rule for highly specific hybridization, Professor Nadrian Seeman was the first to propose the use of DNA strands as the building blocks for a highly programmable three dimensional scaffold. As a protein crystallographer, Professor Seeman proposed that a simple, repeating molecule such as DNA can be easily designed to form repeating two (1,2) and three-dimensional crystals (3) that would in turn serve as a scaffold for hard to characterize proteins. Since his 1982 seminal paper describing the first DNA motifs (4), Prof. Seeman and his colleagues have designed increasingly sophisticated structural motifs, such as the double- and triple-crossover (5-7), to increase the stability of formed DNA structures and build upon a growing library of realized structures. (8)

One important consideration of using self-assembled DNA structures as a scaffold for the assembly of nanomaterials is the conjugation chemistry, or the link between the nanomaterial and the scaffold. The most common conjugation technique with DNA is known as the "sticky end," where end modified, complementary single stranded DNA are attached to two or more components and assembled through sequence specific hybridization. (9-11) While this technique has found extensive applications in assembly nanoparticles for different applications, the minimum number of hybridized bases required for thermal stability (at or around room temperature) is roughly 6 bases, therefore end modified DNA sequences cannot be used to explore single base resolution patterning. To overcome this problem, researchers have also modified the DNA bases, such as biotin-dT, to introduce functional groups inside the strand.(12,13) However, this modification significantly disrupts the Watson-Crick base pairing of DNA and dramatically inhibits the formation of more complex nanostructures. In order to reduce base pairing disruptions, proteins have also been conjugated by introducing functionality with enzymes (14) or in the minor grove of DNA by using polyamide conjugates.(15,16) The used enzyme requires specific DNA sequence for the method to work, restricting the position where protein can be placed. Researchers (12,13) have also demonstrated the assembly of nanoparticles into one and two dimensional structures through the use of nicks to extend sticky ends from the structure. By reducing the number of hybridized base pairs, this strategy is also prone to thermally unstable structures.

In order to demonstrate control over intra-strand chemistry without significant disruptions to the stability of the double helix, we turn to the sugar-phosphate backbone. Phosphorothioate modification (or S-oligos) is a variant of DNA where one of the two

non-bridging oxygen atoms has been converted to a sulfur atom. This chiral modification was originally explored for its ability to significantly increase the stability of DNA for in vitro and in vivo applications where DNA is quickly degraded by endo- and exo-nucleases such as POL1 exonuclease, nucleases S1 and P1, serum nucleases, and snake venom phosphodiesterase. Shaw *et al.* (17) showed that the half-life of DNA in serum increased from roughly three hours to greater than 7 days by replacing a diester bond with a thioate. In the same year, Conway (18) demonstrated the reactivity of the phosphorothioate moiety by attaching a small molecule dye, monobromobimane to the backbone. By labeling the oligos with multiple dyes, they reported that DNA containing > 1000 bases pairs can be visualized without the use of electronic equipment with a detection limit in the low to sub-femtomolar range. Fidanza *et al.* (19) reported in the subsequent year the conjugation of haloacetamid, aziridine sulfonamide, and unsaturated carbonyl to the phosphorothioate diester. The conditions highlighted in this report formed the basis of sequence design and reaction conditions described later in this chapter. In the report, Fidanza also reported that DNA sequences with a single modification, the thermal stability of the DNA duplex is generally very similar to unmodified DNA, subsequent reports identified a decrease of melting temperature decrease of 1 – 2 °C per phosphorothioate modification. Finally, at roughly $10 per base modification, PS modification is one of the most economical modifications available commercially.

Phosphorothioates are made by two principal routes: by the action of a solution of elemental sulfur in carbon disulfide on a hydrogen phosphonate, or by the more recent method of sulfurizing phosphite triesters with either tetraethylthiuram disulfide (TETD) or 3H-1, 2-bensodithiol-3-one 1, 1-dioxide (BDTD). The latter methods avoid the

problem of elemental sulfur's insolubility in most organic solvents and the toxicity of carbon disulfide. The TETD and BDTD methods also yield higher purity phosphorothioates.

In the first demonstration to functionalize PS-DNA with nanomaterials and assemble nanoparticles into a 1D assembly with nanoscale distance control, a previous student in the lab, Dr. Jung Heon Lee, modified a 100 base pair DNA strand with multiple PS sites as anchor points for gold nanoparticles (AuNP). After confirming that the PS/thiol moiety was not sufficiently reactive to bind directly to the nanoparticle, a short bifunctional linker (BF) was synthesized. The BF has an alkane thiol group at one end that can bind to an AuNP and an iodoacetamide group at the other end that can bind to a phosphorothioate group on a modified DNA backbone. This method can place nanomaterials at any selected backbone site of the DNA structure, making it possible to precisely control the position of the nanoparticles along DNA and the distances between them, without the need to functionalize AuNPs with a large number of DNA molecules (20,21) or purify monofunctionalized nanomaterials.(22-24) In the report, Lee and coworkers were able to control the distance between two AuNP from 60 base pairs to 80 base pairs, corresponding to roughly 20.4 to 27.2 nanometers, respectively, on a 100 base pair double stranded DNA template. (25)

After successfully demonstrating the feasibility of an iodoacetamide bifucntional linker to conjugate AuNPs to a DNA template, we were interested in extending the versatility of this technique to other functional nanoscale materials such as proteins. Designed and synthesized by nature, proteins are diverse and often exhibit a multitude of functions, ranging from fluorescence to catalytic reactions. While their applications in

ensemble solution state have been well established, precise control of protein molecules in nanometer scale distances and their alignment have been explored only recently.[1] Complex protein assemblies hold great promise in proteomics, nanoelectronics, and photonics. In the current work, we synthesize two new bifunctional linkers to incorporate biotin and maleimide to conjugate with streptavidin and a cysteine modified myoglobin, respectively. Additionally, we extended the number of proteins modified to three from a two, as previously reported. Conjugation yield was determined by gel shift assay as well as scanning electron microscopy (SEM) through the use of streptavidin modified gold nanoparticles.

2.2 Results and Discussions

Here, we propose that by modifying the linker chemistry, this technique can be used to conjugate different types of proteins on DNA with nanoscale distance control. First, we demonstrated conjugation of streptavidin (STV, 52.8 kDa) and cysteine modified myoglobin (S35C-Mb, 16.7 kDa) on DNA using biotin and maleimide bifunctional linkers (biotin-BL and maleimide-BL). By introducing multiple linkers on a dsDNA, we could conjugate multiple proteins on a single dsDNA without nick. Furthermore, we showed that the conjugated proteins maintain their activity by binding biotinylated AuNPs onto preassembled STV-dsDNA complexes, resulting in AuNP dimers and trimers with controlled distances.

More importantly, through melting temperature study, we demonstrate that our backbone modified PS DNA system is much more stable than base modified system placed in the middle of a dsDNA strand after protein conjugation. In order to conjugate

STV onto DNA, we used biotin-BL containing an iodoacetamide group on one end and a biotin on the other (Figure 2.1). For the conjugation of any protein with an available cysteine, we synthesized a linker with maleimide (maleimide-BL). As a model protein containing cysteine on its surface, we used a sperm whale myoglobin protein with a cysteine mutation introduced onto the surface (Figure 2.2; see experimental details).

After synthesis of the two bifunctional linkers (see experimental details), the linkers were characterized by electron spray ionization mass spectroscopy (ESI-MS) and the conjugation products after reaction with 3PS-DNA were characterized by matrix assisted laser desorption / ionization mass spectroscopy (MALDI-MS). Figure 2.3 shows the results of the biotin bifunction linker synthesis with a major product peak at 468 MW and a +24 peak that correlates well with the linker associated with a sodium atom. After reacting with an oligonucleotide that has three consecutive phosphorothioate modifications, MALDI-MS shows a distribution of DNA strands with one, two, or three modifications, with a high percentage of strands having at least one conjugated linker. Interestingly, there is a peak corresponding to a 3PS-DNA with 4 attached linkers. Since the sequence was ordered from IDT without gel or HPLC purification, this is likely due to adjacent sites unintentionally modified to PS from PO during synthesis. The biotin modified sequences are then used without further purification. This characterization is repeated for the synthesized maleimide bifucntional linker. Of particular note, the maleimide group is liable to degradation via hydrolysis, the linker was synthesized under dry / argon conditions, using dry reagents whenever possible. Figure 2.4 shows the various characterization of the linker via ESI-MS and the 3PS-DNA linker conjugate by MALDI-MS. It is observed that a majority of the strands were functionalized with at least

one maleimide linker, without significant degradation. The maleimide linker is also used without purification and often within two days of synthesis to avoid degradation.

To demonstrate the activity of the newly functionalized PS-DNA strands, we incubate each bifunctionalized linker functionalized DNA strand with the corresponding protein of interest. Figure 2.5 shows a gel shift assay (10% native PAGE) of the resulting protein conjugates with single stranded DNA strands. Due to the small size of the bifunctional linkers, we cannot observe a structural difference (as characterized by the difference in distanced traveled through the gel matrix) between the modified and unmodified 3PS-DNA strands (lane 1, 2, and 4). However, lane 3 shows a discreet, significantly higher molecular weight when the maleimide modified PS-DNA is reacted with S35C myoglobin, indicating the formation of a discreet conjugate. Lane 5 of the same figure shows the interaction between a biotin functionalized 3PS-DNA with streptavidin. With a molecular weight of 52.8 kDa and a conjugate molecular weight of 59.0 kDa, it can be observed that a discreet, high molecular weight conjugate was formed upon the reaction. Notably, the larger streptavidin-DNA conjugate traveled a smaller distance through the polyacrylamide matrix than a corresponding myoglobin-DNA conjugate (expected molecular weight of 16.7 kDa, combined molecular weight of 22.9 kDa), positively confirming the correct formation of desired conjugates.

Next, we further investigate the interaction between both BL treated PS-DNAs and proteins, biotin-BL-ssDNA and maleimide-BL-ssDNA was treated with STV and S35C-Mb, respectively, and the mixtures were purified with native 4-20% polyacrylamide gel electrophoresis (PAGE) (Figure 2.6). The result confirms the conjugation of streptavidin to biotin-BL-ssDNA (˜59 kDa, lane 3) and cysteine modified

myoglobin to maleimide-BL-ssDNA (˜23 kDa, lane 5). When two complementary ssDNA containing biotin-BL and malemide, respectively, were hybridized and interacted with both proteins, even larger heteroprotein structure (˜82 kDa, lane 7) was obtained. This indicates that two different proteins can be conjugated on a single dsDNA strand.

Since multiple PS modifications can be introduced at any desired places on a DNA backbone, we sought to use the PS-DNA to control the numbers and positions of protein conjugated on a DNA strand. To demonstrate the controllability, 100 bps dsDNAs (~34 nm) with 1-3 binding sites (BSs, each site contains triple biotin-BLs labeled on three adjacent PS modifications) were reacted with STV and purified with native 4-20% PAGE (see Fig. 2). Fluorescein labeled STV (STV-FITC) was used to track their position separately from DNA. As shown in lanes 1-4, if a DNA with at least one BS reacts with STV, identical band appears on both Fig. 2A and B, indicating the formation of STV and dsDNA conjugate. In contrast, control samples without PS modification showed negligible interaction between the biotin-BL and DNA (lanes 5 and 6). More importantly, as the number of BS placed on the DNA increased from 0 to 1, 2, or 3, a series of increasing higher molecular weight bands were formed (Lanes 1-4). This result suggests that as the number of BS placed on the DNA increases, the number of STV conjugated on DNA increases as well. Interestingly, even though the DNA strands with identical length, sequence, and number of BSs were used to conjugate STV, as the distance between the two BSs placed on DNA varies from 80 bps (2BS-dsDNA (80)) to 50 bps (2BS-dsDNA (50)), the positions of the band of two STV-DNA conjugates are different. We attribute the distinct positions of the bands to different conformation of the complexes or possible bending of DNA after conjugation with protein.

For practical applications, the stability of protein-dsDNA conjugate is important. Under identical conditions (5 mM phosphate, 10 mM NaCl buffer, pH 7), the STV-dsDNA conjugate with biotin-BL and PS modification had the melting temperature ~17 ^{o}C higher than that with biotin-dT. This surprising difference strongly suggests that protein-DNA conjugates formed by PS modifications and BLs have higher stability than those formed by modified bases.

Once attached to DNA, it is important for the proteins to maintain their activities so that the protein-dsDNA complex is available as a template for other functions. To demonstrate such an activity, biotinylated AuNPs were treated with STV and 100 bps dsDNA conjugates pre-immobilized on silicon surfaces. Figure 2.7 shows electron microscope image of AuNP trimers formed on STV-3BS-dsDNA templates. A large portion of AuNPs formed trimers with average distance of ~13 nm which is close to the predicted distance of ~14.3 nm. To show distance control, 2BS-dsDNA (80) and 2BS-dsDNA (50) with the binding sites separated by 80 and 50 bps were used. Average distances between AuNPs of dimers were ~26 and ~16 nm, respectively, which is close to the predicted distances between the two binding sites of 2BS-dsDNA (80) (~27.2 nm) and 2BS-dsDNA (50) (~17 nm). Without PS modification, only a few AuNPs were observed. These results suggest that STVs can indeed bind to DNA templates and form trimers and dimers with controlled distances.

2.3 Conclusions

The current work represents a successful proof of concept demonstrating the feasibility of using backbone modified phosphorothioate DNA as anchor points for

nanomaterials via engineered bifunctional linkers. We demonstrate the synthesis of three novel linkers that incorporates thiol, a biotin, and a maleimide group to the PS-DNA backbone that is then subsequently used to conjugate additional nanoparticles or proteins. We also demonstrated that the stability of a biotin moiety introduced onto the backbone of a double helix molecule is higher than a similar moiety introduced via a modified base. We also show the excellent spatial resolution offered through PS-DNA by controlling the spacing between gold nanoparticles separated by a programmed number of bases and verifying the distance control by scanning electron micrographs. Finally, we demonstrated the versatility of the technique by expanding the library of bifucntional linkers to include chemistry for protein conjugation. In particular, we demonstrated by introducing a surface thiol on a protein (cysteine modification), any protein can be theoretically conjugated to the DNA double helix. Looking ahead, there is a tremendous library of available conjugation chemistries that can be introduced to the DNA backbone via the phosphorothioate modification. In the following chapters, we will explore one of the main advantages of the PS-modification: minimal loss of double helix thermal stability (i.e. melting temperature) that will enable the modification of complex DNA structures.

2.4 Experimental Details

Oligonucleotides used in the work were purchased from Integrated DNA Technologies Inc. (Coralville, IA). The detailed sequences and information of the DNA strands are listed below. N-(+)-biotinyl-3-aminopropylammonium trifluoroacetate, N-(2-Aminoethyl)maleimide trifluoroacetate, and iodoacetic anhydride used for synthesis of biotinylated and maleimide containing bifunctional linker syntheses were all ordered

from Sigma-Aldrich (catalog number (CN): 71776, 56951, 284262). Unconjugated and FITC modified streptavidins were purchased from Invitrogen (CN: SNN1001) and Sigma-Aldrich (CN: S3762), respectively. 15% and 4-20% Ready Gel Tris-HCl Gel, used to separate DNA-protein conjugates from unreacted DNA and proteins, were obtained from Bio-Rad. (CN:161-1157 and 161-1159) N-(trimethoxysilylpropyl)ethylenediamine, triacetic acid, trisodium salt, 45% in water used to form layers of carboxyl group on Si substrate was purchased from Gelest, Inc. (CN: SIT8402.0) EDC (N-(3-Dimethylaminopropyl)-*N′*-ethylcarbodiimide hydrochloride) and NHS (Nhydroxysuccinimide) used for the attachment of DNA on Si surface were obtained from Sigma Aldrich (CN: E6383) and Fluka (CN: 08975), respectively. 5 nm biotinylated gold nanoparticles were ordered from NanoCS Inc. (CN: GNB5) P type doped Si wafers (⟨100⟩, 0.01–0.02 ohm-cm) used for AuNP assembly imaging were purchased from Montco Silicon Technologies (CN: S5935).

DNA sequences

Name	Sequence
0PS-20bp DNA	5' - GGC GTT CAC AAG GTC TGC AC - 3'
1PS-20bp DNA	5' - GGC GTT C*AC AAG GTC TGC AC - 3'
3PS-20bp DNA	5' - GGC GTT* C*A*C AAG GTC TGC AC - 3'
2PS-20bp DNA	5' – GGC* G*TT CAC AAG GTC TGC AC - 3'
0PS-20bp DNA-comp	5' - GTG CAG ACC TTG TGA ACG CC - 3'
2PS-20bp DNA-comp	5' - GTG CAG ACC TTG TGA AC*G* CC - 3'
3IntBiot-20bp DNA	5' - GGC GT Biotin-dT Biotin-dT Biotin-dT C AAG GTC TGC AC - 3'
IntBiot-20bp DNA-comp	5' - GTG CAG ACC TTG AAA ACG CC - 3'
Biotin-20bp DNA	5' - Biotin-GGC GTT CAC AAG GTC TGC AC - 3'
Biotin-20bp DNA-comp	5' - Biotin-GTG CAG ACC TTG TGA ACG CC - 3'

0PS-100bp Anchor DNA	5' - GGC ATG GTC TAC GTC ACC CTA GTC AGT CAT CTT GCA CTA TCT CCT TGA GAA CGT CAC GCG TCA GTA CGC TAC ATC TTA CAC CAG CAC TAC GTC ACA CCT A - 3'
1BS-100bp Anchor DNA	5' - GGC ATG GTC TAC GTC ACC C*T*A* GTC AGT CAT CTT GCA CTA TCT CCT TGA GAA CGT CAC GCG TCA GTA CGC TAC ATC TTA CAC CAG CAC TAC GTC ACA CCT A - 3'
2BS-100bp Anchor DNA (80)	5' - GGC ATG GTC* T*A*C GTC ACC CTA GTC AGT CAT CTT GCA CTA TCT CCT TGA GAA CGT CAC GCG TCA GTA CGC TAC ATC TTA CAC CAG CAC TA*C* G*TC ACA CCT A - 3'
2BS-100bp Anchor DNA(50)	5' - GGC ATG GTC TAC GTC ACC C*T*A* GTC AGT CAT CTT GCA CTA TCT CCT TGA GAA CGT CAC GCG TCA GTA CGC* T*A*C ATC TTA CAC CAG CAC TAC GTC ACA CCT A - 3'
3BS-100bp Anchor DNA	5' - GGC ATG GTC T*A*C* GTC ACC CTA GTC AGT CAT CTT GCA CTA TCT CCT TGA GAA C*G*T* CAC GCG TCA GTA CGC TAC ATC TTA CAC CAG CAC TAC GTC A*C*A* CCT A - 3'
100bp comp DNA	5' - TAG GTG TGA CGT AGT GCT GGT GTA AGA TGT AGC GTA CTG ACG CGT GAC GTT CTC AAG GAG ATA GTG CAA GAT GAC TGA CTA GGG TGA CGT AGA CCA TGC C - 3'
Amine-30T-100bp comp DNA	5' - Amine- TTT TTT TTT TTT TTT TTT TTT TTT TTT TTT TAG GTG TGA CGT AGT GCT GGT GTA AGA TGT AGC GTA CTG ACG CGT GAC GTT CTC AAG GAG ATA GTG CAA GAT GAC TGA CTA GGG TGA CGT AGA CCA TGC C - 3'

Bifunctional linker synthesis. N-(+)-biotinyl-3-aminopropylammonium trifluoroacetate was dissolved in 0.1 N NaOH to get 32 mM solution. Also iodoacetic anhydride was dissolved into 1,2 dichloroethane to get 0.22 M solution. Both solutions were mixed in 4:1 ratio and agitated using a vortex mixer for a minute to get white precipitate. The solution was centrifuged at about 10,000*g* for 15 minutes. Since the product is not soluble in either water or 1,2 dichloroethane, the precipitate can be removed from the solvent. In order to separate by-products and reagents from the product,

water was added to the precipitate followed by vortex, centrifugation, and supernatant removal. The process is repeated with acetone to remove unreacted iodoacetic anhydride from the product. The solvent is evaporated and Biotin-BL is stored in powder form.

Maleimide-BL synthesis.To a mixture of iodoacetic anhydride (0.28 mmol), N-(2-Aminoethyl) maleimide trifluroacetate salt (0.10 mmol), and DCM (2.5mL) was added NEt3 (0.028 mmol) dropwise. After stirring at room temperature for 1 hr, the reaction was washed with saturated NaHCO3 (2 x 1mL) and saturated NaCl (1 x 1 mL). The organic layer was dried (Na2SO4), and further dried under vacuum. The product is dissolved in DMSO before use.

Reaction between PS-DNA and bifunctional linkers. Biotin-BL was dissolved in DMSO so that the concentration becomes 100 mM. For DNA with one phosphorothioate modification, Biotin-BL in DMSO and phosphorothioate modified DNA in S4 buffer is mixed in the ratio of 200 to 1 in DMSO/water 1:1 solution. The reaction can be made at 30 oC for 5 hours. (Caution: Biotin-BL can be degraded in DMSO in a few days. So it is suggested to dissolve Biotin-BL in DMSO right before use).

DNA preparation and hybridization. 20bp dsDNA: Two complementary DNA strands were mixed in 20 mM phosphate (pH 7) / 100 mM NaCl and kept at room temperature for about an hour for hybridization. The concentration of DNA is 8 μM.

100bp dsDNA: Biotin-BL-3BS-dsDNA, Biotin-BL-2BS-dsDNA (80), Biotin-BL-2BS-dsDNA (50), and 0BS-dsDNA were prepared by hybridizing two complementary DNA strands in 20 mM phosphate (pH 7), 50 mM NaCl buffer at room temperature for about an hour. The concentration of DNA is 1.5 μM. Amine-30T-100bp comp DNA was

used instead of 100bp comp DNA for immobilization of DNA on carboxyl group modified on Si surface.

Gel electrophoresis. 15% Ready Gel (Tris-HCl Gel) was used to separate 20bp dsDNA conjugated with STV-FITC from unreacted dsDNA and STV. 8 μM of dsDNA and 48 μM of STV were mixed for STVdsDNA conjugation. STV-dsDNA reaction was made for 1.5 hrs before running gel. 4-20% Ready Gel (Tris-HCl Gel) was used to separate 100bp dsDNA conjugated with multiple STV-FITCs from unreacted dsDNA and STV-FITC. The concentration of DNA was adjusted to 300 nM and STV-FITC was added afterwards (27 μM) for STV-dsDNA conjugation. STV-FITC was used in excess to prevent crosslinking of STV and dsDNA. STV-dsDNA reaction was made for 1.5 hrs before running gel. 50 mM Tris acetate buffer (pH 7.2) was used as running buffer. As STV has isoelectric point (pI) around 5.5, it is negatively charged with about two electron charges at pH 7.2 (3) and it can migrate through gel with DNA as well. The concentration of STV was calculated based on the reported extinction coefficient of 41820 L mol-1cm-1 at 280 nm.

Melting temperature experiments. After 20bp dsDNA (0PS-dsDNA, 3PS-dsDNA, Biotin-dsDNA, Biotin-3dT-dsDNA, see Table S2) was hybridized and prepared based on the procedure mentioned above, the STV-dsDNA conjugate was formed by adding 4 eq. of STV into DNA solution. Afterwards the concentrations of phosphate and NaCl were adjusted to 5 and 10 mM, respectively. The temperature was controlled from 4 oC to 60 oC with 2 min interval between each temperature. HP 8453 UV-vis S5 spectrometer was used to collect absorbance variation at 260 nm.

AuNP attachment on STV-dsDNA templates. After piranha solution treatment and thorough washing, Si substrates were incubated in 0.45 % N-trimethosysilylpropyl) ethylenediamine, triacetic acid, sodium salt solution (0.5 mL of 45% solution was diluted in 50 mL of deionized water) for 12 hours to form multilayers of carboxyl groups on Si surface. The Si surface was thoroughly washed afterwards. In order to immobilize DNA on Si surface, 100bp dsDNA (3BS-dsDNA, 2BS(80)-dsDNA, 2BS(50)-dsDNA, and 0BS-dsDNA) was first prepared and hybridized following the process mentioned above. In this case, Amine-30T-100bp comp DNA (containing amine group on 5'end of the strand linked by 30T) was used instead of 100bp comp DNA to provide flexibility to dsDNA on the surface. After incubating carboxyl group modified Si substrate into DNA solution, 11 volume % of NHS solution (16.5 mg dissolved in 2.5 mL deionized water) was added to the DNA solution. Eleven volume % of EDC solution (33 mg dissolved in 2.5 mL deionized water) was added immediately afterwards and the reaction was kept for an hour. The Si substrates were washed with 25 mM phosphate (pH 7) and 100 mM NaCl.

To conjugate STV on dsDNA immobilized on surface, Si substrates were incubated in 2 μ M STV solution in 30 mM phosphate (pH 7) and 400 mM NaCl for an hour. The Si substrates were washed thoroughly with 25 mM phosphate (pH 7) and 100 mM NaCl.

To assemble AuNPs onto STV-dsDNA templates, Si substrates containing STV treated dsDNA were treated with 70 nM 5 nm biotinylated AuNPs solution 25 mM phosphate (pH 7) and 250 mM NaCl buffer. The reaction was made for 15 hours. Afterwards the Si substrates were washed thoroughly with 25 mM phosphate (pH 7) and

25 mM NaCl. The Si substrates were gently washed with deionized water before imaging to remove salt on the surface.

Hitachi S4800 scanning electron microscope was used to take images of AuNP trimers and dimers on Si surface. SEM was performed at 10 kV at the working distance of about 5 mm.

2.5 References

(1) Mao, C. D.; Sun, W. Q.; Seeman, N. C. *J. Am. Chem. Soc.* **1999**, *121*, 5437-5443.

(2) Liu, H. P.; He, Y.; Ribbe, A. E.; Mao, C. D. *Biomacromolecules* **2005**, *6*, 2943-2945.

(3) Zheng, J.; Birktoft, J. J.; Chen, Y.; Wang, T.; Sha, R.; Constantinou, P. E.; Ginell, S. L.; Mao, C.; Seeman, N. C. *Nature* **2009**, *461*, 74-77.

(4) Seeman, N. C. *J. Theor. Biol.* **1982**, *99*, 237-247.

(5) LaBean, T. H.; Yan, H.; Kopatsch, J.; Liu, F. R.; Winfree, E.; Reif, J. H.; Seeman, N. C. *J. Am. Chem. Soc.* **2000**, *122*, 1848-1860.

(6) Fu, T. J.; Seeman, N. C. *Biochemistry* **1993**, *32*, 3211-3220.

(7) Mao, C. D.; LaBean, T. H.; Reif, J. H.; Seeman, N. C. *Nature* **2000**, *407*, 493-496.

(8) Seeman, N. C. *Nature* **2003**, *421*, 427-431.

(9) Chen, J. H.; Seeman, N. C. *Nature* **1991**, *350*, 631-633.

(10) Mirkin, C. A.; Letsinger, R. L.; Mucic, R. C.; Storhoff, J. J. *Nature* **1996**, *382*, 607-609.

(11) Winfree, E.; Liu, F. R.; Wenzler, L. A.; Seeman, N. C. *Nature* **1998**, *394*, 539-544.

(12) Yan, H.; Park, S. H.; Finkelstein, G.; Reif, J. H.; LaBean, T. H. *Science* **2003**, *301*, 1882-1884.

(13) Li, H. Y.; Park, S. H.; Reif, J. H.; LaBean, T. H.; Yan, H. *J. Am. Chem. Soc.* **2004**, *126*, 418-419.

(14) Braun, G.; Diechrierow, M.; Wilkinson, S.; Schmidt, F.; Huben, M.; Weinhold, E.; Reich, N. O. *Bioconjugate Chem.* **2008**, *19*, 476-479.

(15) Cohen, J. D.; Sadowski, J. P.; Dervan, P. B. *Angew. Chem. Int. Edit.* **2007**, *46*, 7956-7959.

(16) Cohen, J. D.; Sadowski, J. P.; Dervan, P. B. *J. Am. Chem. Soc.* **2008**, *130*, 402-+.

(17) Shaw, J. P.; Kent, K.; Bird, J.; Fishback, J.; Froehler, B. *Nucleic Acids Res.* **1991**, *19*, 747-750.

(18) Conway, N. E.; McLaughlin, L. W. *Bioconjugate Chem.* **1991**, *2*, 452-457.

(19) Fidanza, J. A.; Ozaki, H.; McLaughlin, L. W. *J. Am. Chem. Soc.* **1992**, *114*, 5509-5517.

(20) Le, J. D.; Pinto, Y.; Seeman, N. C.; Musier-Forsyth, K.; Taton, T. A.; Kiehl, R. A. *Nano Lett.* **2004**, *4*, 2343-2347.

(21) Pinto, Y. Y.; Le, J. D.; Seeman, N. C.; Musier-Forsyth, K.; Taton, T. A.; Kiehl, R. A. *Nano Lett.* **2005**, *5*, 2399-2402.

(22) Loweth, C. J.; Caldwell, W. B.; Peng, X. G.; Alivisatos, A. P.; Schultz, P. G. *Angew. Chem. Int. Edit.* **1999**, *38*, 1808-1812.

(23) Fu, A. H.; Micheel, C. M.; Cha, J.; Chang, H.; Yang, H.; Alivisatos, A. P. *J. Am. Chem. Soc.* **2004**, *126*, 10832-10833.

(24) Deng, Z. X.; Tian, Y.; Lee, S. H.; Ribbe, A. E.; Mao, C. D. *Angew. Chem. Int. Edit.* **2005**, *44*, 3582-3585.

(25) Lee, J. H.; Wernette, D. P.; Yigit, M. V.; Liu, J.; Wang, Z.; Lu, Y. *Angew. Chem. Int. Edit.* **2007**, *46*, 9006-9010.

2.6 Figures

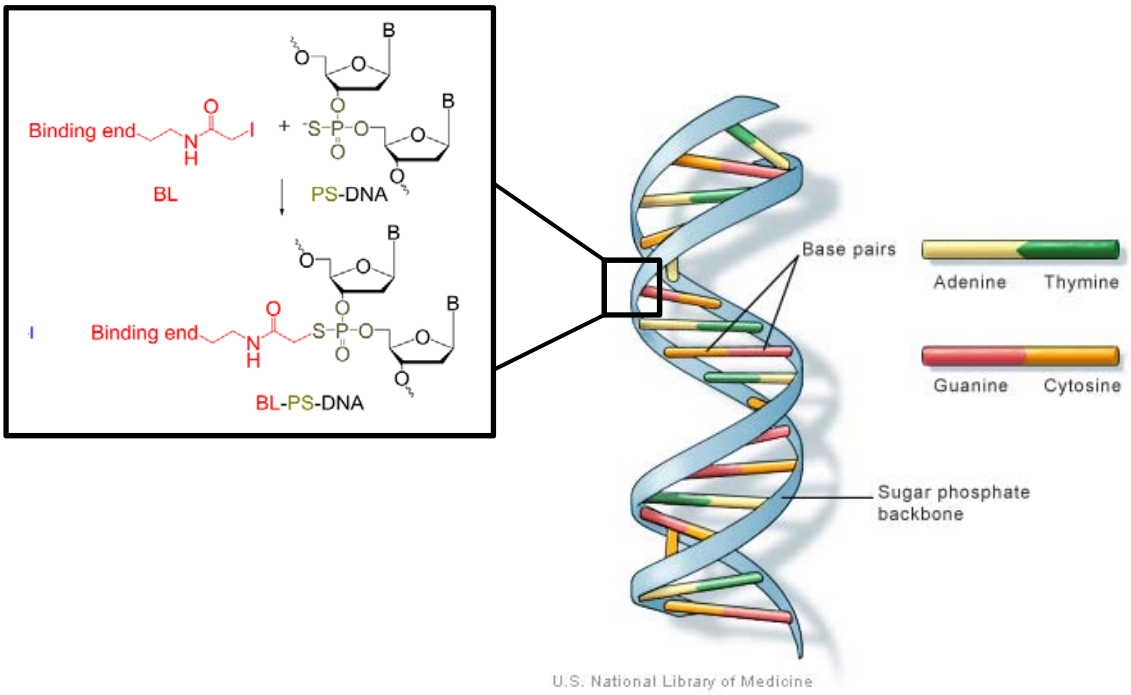

Figure 2.1 Schematic and chemical structure of the double helix DNA and phosphorothioate modification on one of the non-bridging oxygens on the DNA sugar phosphate backbone. The proposed chemical reaction between an iodoacetamide linker and the phosphorothioate modification is illustrated in the enlarged schematic. The binding end can be modified for a wide variety of conjugation chemistries.

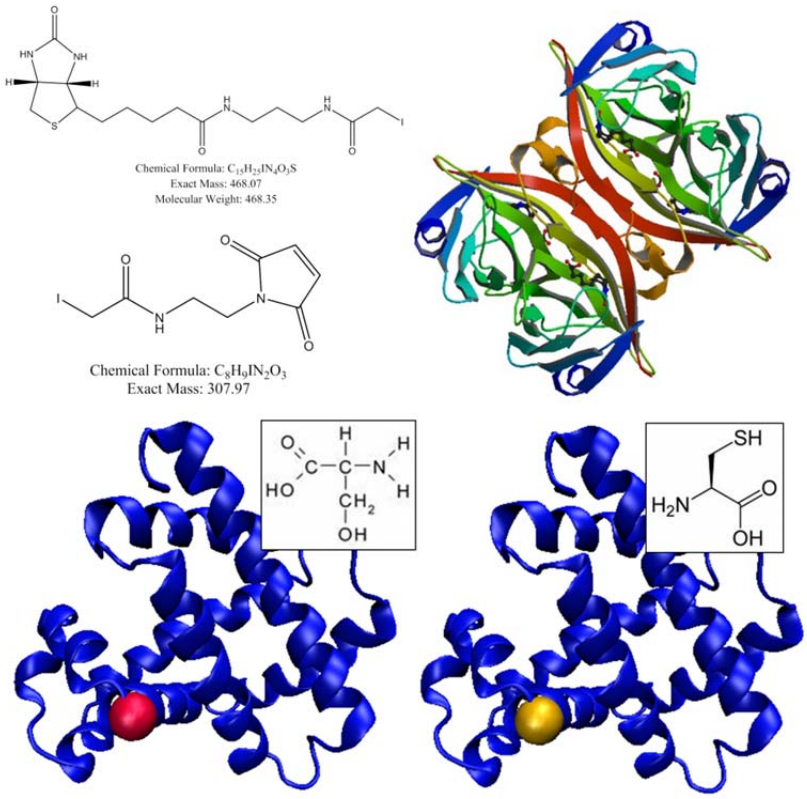

Figure 2.2 Chemical structures of the two synthesized bifunctional linkers (biotin and maleimide functionalized) as well as the two proteins of interest to this study: streptavidin and myoglobin. The bottom shows a representation of the serine (S35) mutation to cysteine, thereby introducing a thiol group to the surface of the protein. This thiol subsequently reacts with the maleimide linker to form a covalent bond between the protein and the DNA scaffold.

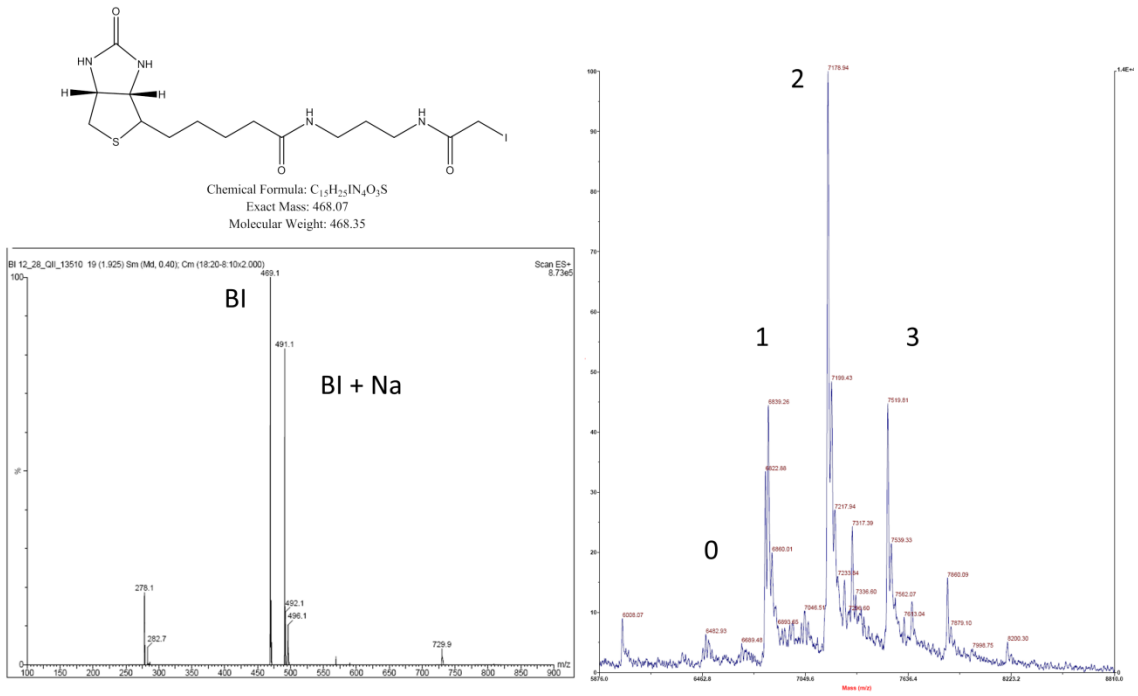

Figure 2.3 Chemical structure of the synthesized biotin bifunctional linker. The synthesis is confirmed via time-of-flight mass spectrometry where a correct mass of 468 was observed. (Right) After reacting with a DNA strand with 3 consecutive phosphorothioate modifications, the product was characterized using matrix assisted laser desorption/ionization mass spectroscopy (MALDI-MS). Peaks corresponding to the original, unmodified strand, as well as those corresponding to 1, 2, and 3 conjugated biotin linkers were observed.

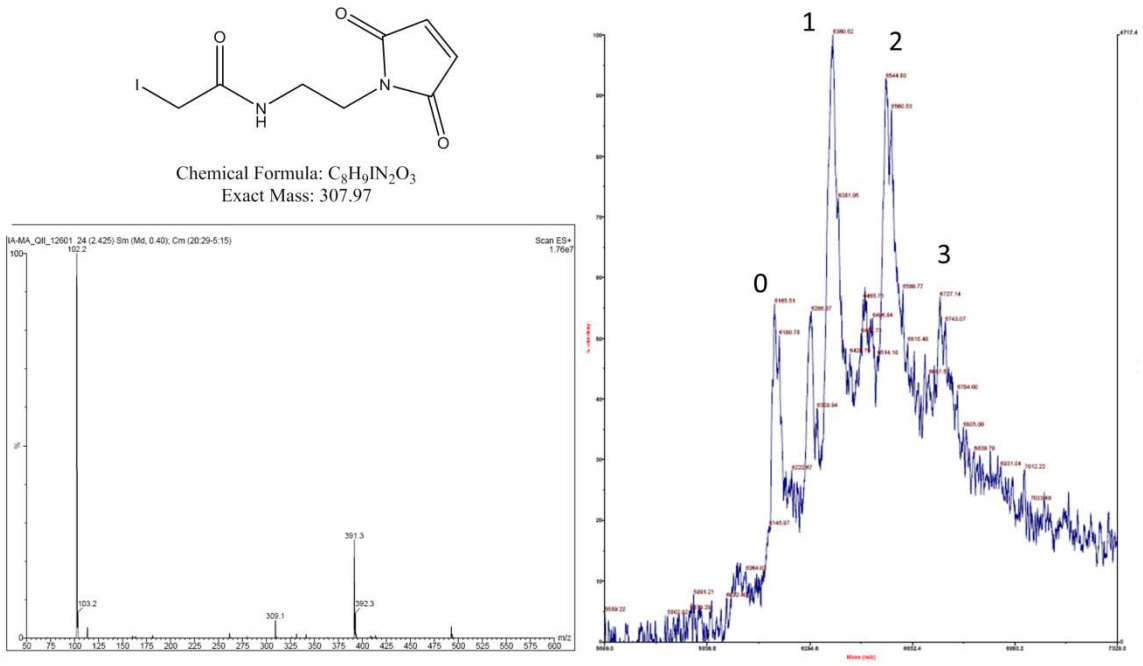

Figure 2.4 Chemical structure of the synthesized maleimide bifunctional linker. The synthesis is confirmed via time-of-flight mass spectrometry where a correct mass of 307 was observed. (Right) After reacting with a DNA strand with 3 consecutive phosphorothioate modifications, the product was characterized using matrix assisted laser desorption/ionization mass spectroscopy (MALDI-MS). Peaks corresponding to the original, unmodified strand, as well as those corresponding to 1, 2, and 3 conjugated maleimide linkers were observed.

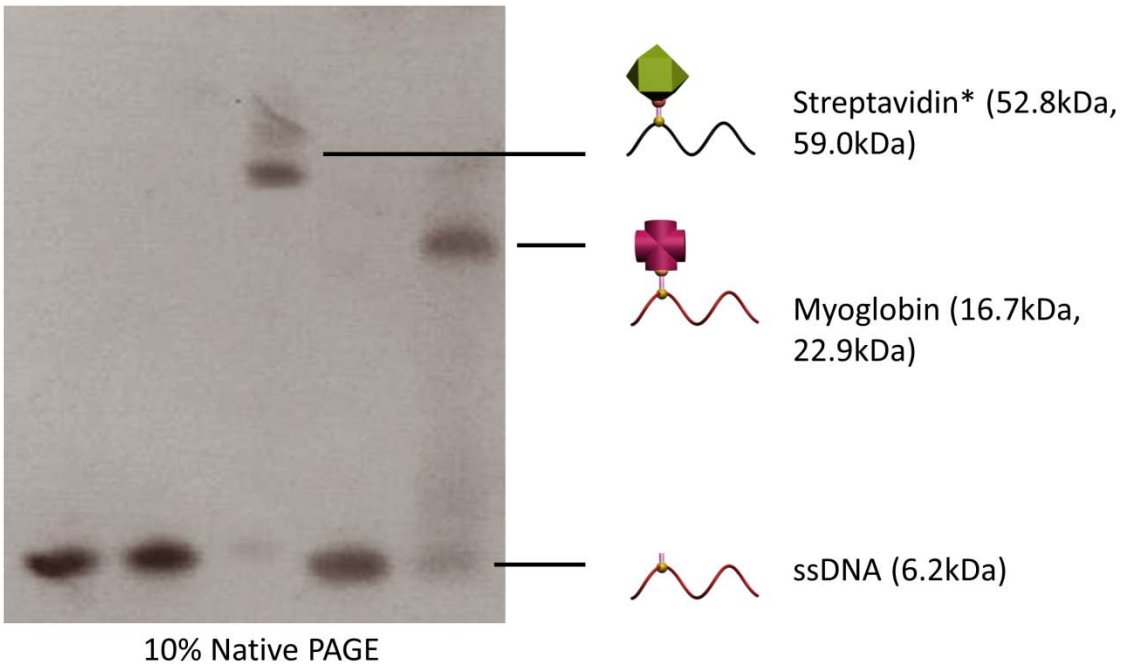

Figure 2.5 Gel shift assay under native conditions. (Lane 1) Original, unmodified DNA strand. (Lane 2) Single stranded phosphorothioate modified DNA (ss-PS-DNA) with biotin-bifunctional linker. (Lane 3) Biotin functionalized PS-DNA incubated with streptavidin. (Lane 4) Single stranded phosphorothioate modified DNA (ss-PS-DNA) with maleimide-bifunctional linker. (Lane 5) Maleimide functionalized PS-DNA incubated with myoglobin.

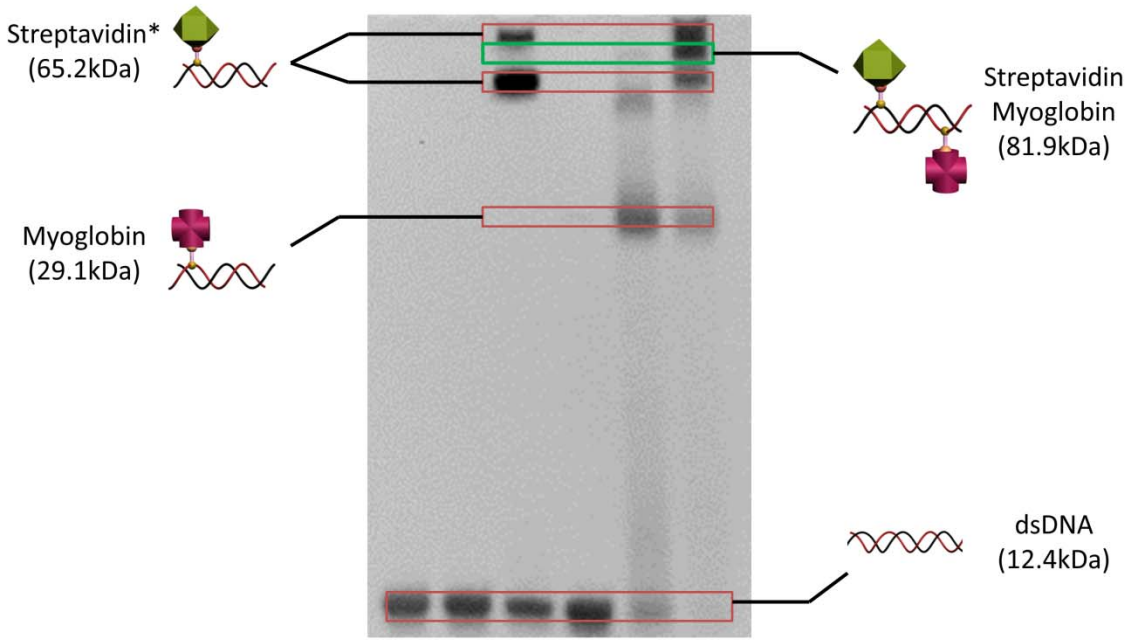

Figure 2.6 Gel shift assay under native conditions. (Lane 1) Double stranded phosphorothioate modified DNA (ds-PS-DNA). (Lane 2) ds-PS-DNA with biotin-bifunctional linker. (Lane 3) ds-PS-DNA with biotin-bifunctional linker incubated with streptavidin. (Lane 4) Maleimide functionalized ds-PS-DNA. (Lane 5) Maleimide functionalized ds-PS-DNA incubated with myoglobin. (Lane 6) Hybridized product of ss-PS-DNA with biotin/streptavidin and ss-PS-DNA with maleimide/myoglobin.

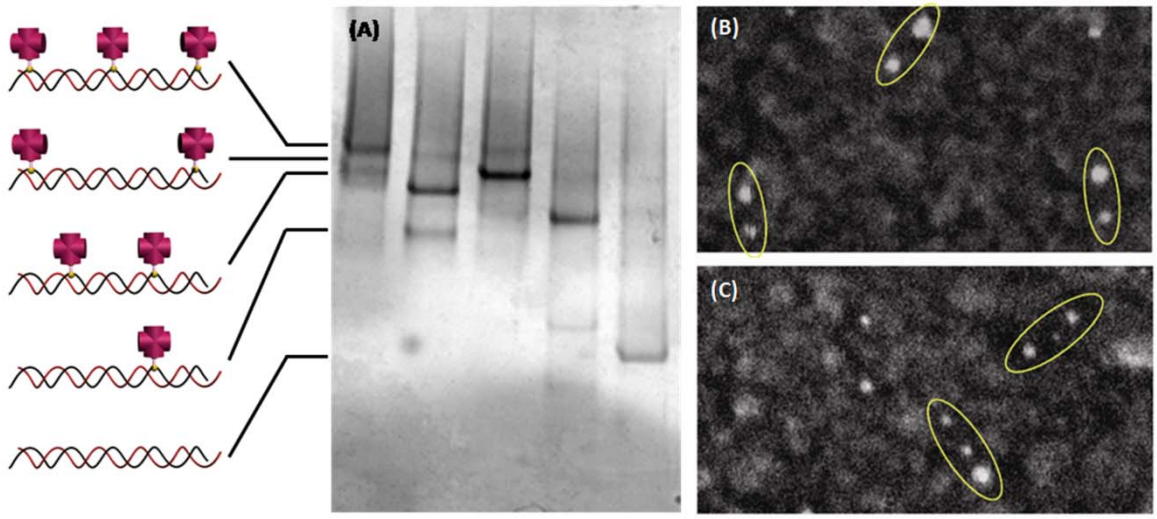

Figure 2.7 Multiple STV attachment onto 100 base-paired dsDNA, demonstrated by native PAGE. Images of (A) fluorescein labeled STV (λ_{excit} = 473 nm and λ_{em} = 520 nm) and (B) EtBr treated DNA (λ_{excit} = 530 nm and λ_{em} = 580 nm) after conjugation. Both gel images are taken from the identical gel, but at different excitation and emission wavelengths. Lanes 1-5: 3BS-dsDNA [3 binding sites (BS) on DNA with 42 bps distances], 2BS-dsDNA (80) [2BSs on DNA with 80 bps distance], 2BS-dsDNA (50) [2BSs on DNA with 50 bps distance], 1BS-dsDNA [1BS on DNA], and Biotin-BL treated 0BS-dsDNA [no BS on DNA] treated with STV. Lane 6: Biotin-BL untreated 0PS-dsDNA with STV. Lane 7 and 8: Unreacted STV and 0BS-dsDNA, respectively. Once dsDNA bind to STV, the conjugate should be observed in both gel

CHAPTER 3

ASSEMBLY ON COMPLEX DNA NANOSTRUCTURES WITH ADVANCED CONTROL AND PRECISION

Significant portions of this chapter were published as "Site-Specific Attachment of Proteins onto 3D DNA Tetrahedron through Backbone-Modified Phosphorothioate DNA" Ngo Yin Wong, Chuan Zhang, Li Huey Tan, and Yi Lu, *Small* **2011**, 7, 1427 – 1430.

3.1 Introduction

In chapter one, we introduced and demonstrated the feasibility of phosphorothioate modified DNA backbones as a one dimensional template for patterning nanomaterials such as nanoparticles and proteins with excellent resolution and minimal disruption to the stability of the double helix structure. To explore this idea further, we hypothesize that the PS modification is ideal for enabling the functionalization of complex DNA nanostructures, as well as enabling advanced spatial and orientation control over the conjugated material. (1)

As discussed briefly in the introduction of this thesis, there are two main strategies to build DNA nanostructures, the DNA tile methods and the origami method. The DNA tiles is designed and assembled from a small number of short DNA oligos, usually less than 4 strands of roughly 30-60 base pairs. These short oligonucleotides are designed such that they form double crossover (DX) or triple crossover (TX) structures, desigsn that significantly increased the rigidity of artificial DNA structures and advanced the field of structural DNA nanotechnology and is worthwhile of a brief discussion here.

DNA branched junctions were first described by Seeman and coworkers in the 1980s. (2) The first designs were inspired by the Holliday junction, a transient formation that supports genetic exchange in many organisms. By carefully optimizing the sequence and length of the arms, Seeman and coworkers were able to stabilize the three and four arm junctions, but the rigidity of the tiles remained an issue. If a four arm junction is not rigid and where each arm is fixed at right angles from each other, the tiles cannot be organized into larger, periodic structures due to angle fluctuations. This was eventually solved with the design of the double crossover structure, again by Seeman and coworkers. (3) The double crossover consists of joining two adjacent double helixes by a single strand that begins on one helix and ends on the adjacent helix. This concept was further extended into a triple crossover (TX) and the increase rigidity, along with the incorporation of sticky ends, later enabled allowed the growth of large two and three dimensional DNA crystals. (4)

One of the characteristics of using these multi-arm junctions is the lack of control over how large the final assembly becomes. Thanks to the symmetric nature of the tiles and the sticky ends, with careful design and preparation, Mao *et al.* have shown that two dimensional crystals can growth over 20 microns in length. (5) In order to gain greater control over the assembly, Yan et al. demonstrated the assembly of finite arrays through the judicious use of sequence symmetry. In an elegant demonstration of “algorithmic self-assembly” Winfree *et al.* (6,7) demonstrated that armed tiles can be used to create “Wang tiles” where each tile contains a single “color” on each of the four sides and assembles such that the adjacent tile is of the same color. From assembled templates, it is easy to imagine the decoration of these structures with different nanomaterials. Indeed

this was extensively explored by Kiehl, Seeman, and Yan, among many others. (8-11) Most of these researchers used toe-hold sticky ends as an anchor for the hybridization with a complementary strand that is attached to a nanomaterial.

More interestingly, by introducing additional flexibility at the vertices of these tiles, it becomes possible to form discreet three dimensional (3D) polyhedral. In an elegant demonstration He *et al.* (12) demonstrated the assembly of tetrahedral, dodecahedra, and buckyballs by controlling the concentration of three arm tiles in a one pot process. Other examples of 3D DNA structures include cubes (13), truncated octahedral (14), octohedra (15), and tetrahedral (16,17). The DNA tetrahedron described by He *et al.* forms the basis of the work in this chapter. He and coworkers further demonstrated structural control by designing and assembly two chiral DNA octahedral by taking advantage of the DNA double helix. (18) It is important to note that the tetrahedrons described by He (12) and Goodman (16) have significant differences that have lead to the higher adoption of Goodman's tetrahedron. Briefly, He's tetrahedron consists of 4 four-armed tiles that have sticky ends of 6-8 bases. This type of tile based assembly requires a long annealing process (24 – 48 hours), careful control of concentration (cannot exceed 60 nM), and careful titration of component strands to form the tetrahedrons. In contrast, Goodman's tetrahedron is considerably more simple, consisting of only 4 strands, with each strand making up one half of the double helix for each side of the tetrahedron. This simple design allows the tetrahedron to form is much higher concentrations and with higher yield, as well as a higher tolerance for strand ratios. In the following work, we succesfully demonstrate that the phosphorothioate backbone

anchor for fucntionalization is compatitble with both tetrahedrons, with the distinction of being the first chemistry reported to sucessfully decorate He's tetrahedron.

While there have been many excellent reports of assembly of proteins on a 2D scaffold, there has been significantly fewer reports of assembly on a 3D scaffold. Xibo *et al.* (19) described a "quasi-3D" structure by first assembling AuNPs on a 2D origami surface and subsequently rolling the structure into a 3D plasmonic structure with the introduction of additional staple strands. In one of the first demonstration of decoration of a 3D structure, Erben and coworkers (20) showed the encapsulation of a 12.4 kDa cytochrome c within a simple tetrahedron structure. The tetrahedron consists only of 4 unique strands and is smaller than the structure described previously. However, relaxed stoichiometric ratio requirements and a high assembly yield without the need for purification has fueled the popularity of this structure among researchers, with several recent publications by Walsh (21), Schueller (22), and Lee (23), demonstrating their in vitro applications. In one of the most complete *in vitro* and *in vivo* demonstrations of DNA nanostructures of diagnosis and therapy applications, Lee (23) highlighted the homogenous size, composition, and surface chemistry of DNA nanostructures. DNA structures also offer flexibility in size control as well as site-specific, asymmetric functionalization. Finally, taking advantage of the increased stability of DNA structures versus individual double stranded and single stranded DNA in serum and biological fluids, Lee and coworkers demonstrated targeted delivery of siRNA for gene silencing in in tumor xenograft mouse models via functionalized DNA tetrahedrons. Interestingly, they reported the optimal number of folate (as targeting agent) to be three, with no improvement in gene silencing with increasing numbers of folate. However, by

orientating the direction of each folate modification, they were able to see an increasing in gene silencing by orienting the targeting ligands in the same direction.

More recently, reports of *in vivo* fabrication of DNA structures were reported. Lin *et al.* (24) successfully incorporated sequences to form nanostructures into XL1-Blue cells and subsequently produced in high numbers by the cell. Delebecque and coworkers (25) reported the design and assembly of one and two dimensional RNA structures that assembled proteins in the hydrogen producing pathway and demonstrated that the presence of the scaffold proportionally increased the production of hydrogen.

3.2 Results and Discussions

For the current work, we chose to work with a 3 armed DNA motif, first proposed by He et al., that can form large, repeating hexagonal structures in the 2D or modified slightly to form a simple tetrahedron 3D cage. (12) Since both structures can be formed by the specific hybridization of 3 different strands of DNA, our strategy involves the functionalization of the "central" strand of the motif with phosphorothioate modifications on the DNA backbone. As will be described below, we designed a soluble version of the bifunctional linker to increase stability of the linker during the long anneal process. By introducing a biotin on one end of the linker, we are then able to conjugate a single streptavidin protein onto each tile, and since four tiles make up each tetrahedron, we would in theory be able to attach four proteins onto each tetrahedron. Using this current design, it is not possible to control the number of proteins that are conjugated to the tetrahedron since each of the vertexes is made up of an identical tile. Later, we utilize a different tetrahedron that allowed not only control over the number of protein conjugated

to a three dimensional structure, but the orientation of the protein cargo as well. Finally, we explore an often overlooked chemistry that allows the simple and effective release of the streptavidin cargo from the DNA nanostructures, enabling possible applications for DNA structures as nanoscale delivery vehicle for *in vitro* or *in vivo* applications.

Our previous work has confirmed the reaction between the iodoacetamide group with a phosphorothioate modification with high yield. PS modified DNA is conjugated with biotin linker in 1x TAE-Mg2+ buffer for 5 hours at 50C, the resulting product is desalted to remove excess linker molecules. The conjugation yield is greater than 90 percent as shown by mass spec and gel shift assay and is used without further purification. We have also demonstrated that the linker conjugation is thermally stable under the annealing conditions necessary to form 2D and 3D structures.

In the previous demonstration of phosphorothioated modified DNA (PS-DNA) by Lee et al., the linker used was a highly hydrophobic bifunctional small molecule that was the result of reacting N-(+)-biotinyl-3-aminopropylammonium trifluoroacetate with iodoacetic anhydride. The resulting product was almost completely insoluble in water and as a result its conjugation to the water soluble PS-DNA was easily prone to hydrolysis and degradation. This was a significant barrier as unlike the previous work in which the 1 dimensional arrays were formed by simply mixing complementary DNA sequences at room temperature and allowing the double helix to form, the formation of the DNA tetrahedron required heating the DNA strands to 90 °C and allowing it cool slowly over 48 hours. Mass spectroscopy confirmed that the linker modified DNA cannot survive the heating and the thiol is quickly hydrolyzed back into an oxygen atom and the linker is removed. One strategy to improve the stability of the linker was by making the

bifucntional linker more water soluble through the introduction of a short polyethylene glycol (C-C-O) chain within the linker. In determining the optimal linker, it is important to optimize the hydrophilicity of the bifuctional linker while minimizing the length to maintain good spatial control. By introducing a “three PEG” spacer in the linker, mass spectroscopy data showed that the linker is stable enough to withstand the annealing process of the tetrahedron. It is worth noting that a “two PEG” spacer exhibited significantly reduced solubility. For details on the synthesis and characterization of the biotin-PEG-iodoacetate linker, please see the experimental details later in the chapter.

The tetrahedron is formed by annealing a long, single circular “central” strand, along with two shorter “arm” strands. In designing the tile for formation of polyhedral, He et al. introduced 5 non-hybridized tymines that introduce the necessary flexibility to bend the tiles inward 60 degrees needed to form the vertices of a tetrahedron. A simple simulation of the location of the backbone shows that these bases are ideally suited for phosophorothioate modification since the phosphate backbone appears to be facing outward at each of the vertices. Also, the non-hybridized nature of the thymine means minimal disruption to base pairing and the stability of the structure. This is an important point for while these structures have been discovered for more than 4 years, there has yet to be a report of decoration of this type of structure with nanomaterials. Finally, the availability of three thymine sites (of five available) for phosphorothioate modification significantly increases the efficiency of linker binding and finally, the efficiency of protein binding as first reported by Lee and coworkers.

The PS modified central strand was first chemically modified with the synthesized biotin polyethyleneoxide iodoacetamide bifunctional linker in 1x TAE-Mg^{2+}

buffer at 50 °C for 5 hours and the excess linker was removed by size exclusion column. The conjugation was confirmed by mass spectrometry and the reaction yield was 100% after purification (for details, please again refer to experimental details section below). The use of non-purified strands resulted in a lower density of protein binding, therefore the purification step is necessary to achieve high density of protein conjugation (up to a maximum of 4 per tetrahedron) to the final tetrahedron structure.

After the functionalization of the long central DNA strand with the biotin bifunctional linker, individual DNA tiles (without sticky ends to form larger structures) were assembled by truncating the shortest arm strand that makes up the tile. The formed structures were incubated with streptavidin and characterized by gel shift assay. From the gel image, greater than 90% of the formed tiles are able to withstand the annealing process and subsequently bind a streptavidin protein to the PS modified DNA strand.

Assembly of the DNA tetrahedron containing the PS modification and bifunctional linker was adapted from a previously reported protocol. (26) Briefly, the three DNA strands were mixed at a ratio of (1:3:3) in a Tris-acetic acid-EDTA-Mg^{2+} buffer and the mixture was slowly cooled from 95 °C to 25 °C over 48 hours. The assembled DNA structures were characterized by non-denaturing polyacrylamide gel electrophoresis (PAGE). As shown in Figure 3.5, only a single band was observed in lane 1 and 3, suggesting that the PS modified and biotin linker functionalized central strands self-assemble with the middle and short strands into a single complex, in good agreement with previous reports. In order to keep a strict 1:3:3 ratio between the three sequences, the stock DNA is first diluted to the desired concentration as measured by Abs(260 nm) using a UV-Vis. Next, titration gels are used to fine tune the ratio between strand 1 and 2

as well as between 2 and 3. By varying the volume of one with respect to the other, annealing, and separated by 10% PAGE, the volume ratio where either initial strands cannot be seen (only higher molecular weight assembly is visible, Figure 3.5 and Figure 3.6) is determined to be the optimal ratio. For simplicity sake, it is often desired that the concentrations of the three strands be set to 3.33x, 10x, and 10x, respectively.

After determining the precise volume ratio of the three strands, they were combined at a final concentration of 60 μM in 1x TAE-Mg^{2+} buffer and annealed from 90 °C to room temperature over 2-3 days. The annealing process was done by floating the samples in a 2 liter water bath heated to 90 °C and placed in a large Styrofoam box and left until the system has cooled to room temperature. After carefully washing the annealed structures by centrifugation 3 times, the structures were characterized by native PAGE and stored for a maximum of three days at 4 °C until used.

To form the 3D tetrahedron, the structures are incubated with a solution of streptavidin for 2 hours before analysis by native gel shift assay and imaged under fluid atomic force microscopy. Figure 3.4 shows the results of a 10% native polyacrylamide gel shift assay analyzing the results of a typical tetrahedron assembly without further purification. Lane 1 shows the biotinylated PS-DNA strand with a portion associated with the streptavidin protein (as evident by the slower moving band, indicating a larger, higher molecular weight complex). Lanes 3, 4, and 5 shows a distinct band that corresponds to the tetrahedron, the PS-modified tetrahedron, and the biotin linker modified tetrahedron. The consistent location of the three bands indicated that the modifications and bifunctional linkers did not dramatically alter the shape and size of the tetrahedron. However, upon the introduction of streptavidin to a biotin linker modified tetrahedron,

the band that corresponded to an unmodified tetrahedron fades and discreet higher molecular weight products became visible.

Figure 3.5 then shows the results of the assembly and conjugation process with purified strands. As shown in the lane 3 and 4 of Figure 3.5, the band corresponding to the DNA tetrahedron containing PS modification and bifunctional linker fades and four discreet bands with higher molecular weights appeared instead. These results suggest successful conjugation of one, two, three, and four proteins onto the DNA nanostructure. Since the streptavidin protein has 4 binding sites for biotin, the concentration of protein added is ~16 times the concentration of tetrahedrons to encourage the binding of multiple proteins to a single nanostructure while discouraging the formation of single protein bound to multiple nanostructures. While we can achieve 100% conjugation of protein to single stranded PS-DNA, (Figure 3.1) the yield of tetrahedron structures modified with 4 streptavidin was significantly lower than expected. This is likely due to thermal degradation and hydrolysis of the biotin linker during the annealing process.

To further confirm the successful conjugation of protein to the discrete nanostructure, the unmodified structure and the band corresponding to tetrahedron with 1 protein attachment was purified by non-denaturing PAGE, recovered, and imaged using alternating current atomic force microscopy (AC-AFM). In the absence of streptavidin, the AC-AFM image of the assembled DNA strands containing PS modification and bifunctional linker showed well dispersed and uniform structures with a height of approximately ~2 nm and a lateral dimension of 25 nm (Figure 3.6). These results are similar to what was observed previously reported DNA tetrahedron without the PS modification or the bifunctional linker, and are consistent with a collapsed tetrahedron

due to its dried state and the tapping force. (26) After incubation with protein, nanostructures recovered from the band corresponding to a tetrahedron with one bound streptavidin shows structures with an increase in height to ~6 nm, correlating well with the addition of a ~4 nm protein onto the tetrahedron. Additional evidence for protein conjugation to the DNA tetrahedron scaffold can be obtained from observation of 2D structures when the same samples were imaged in fluid, which shows larger, unfolded hexagonal arrays formed from 3 point star components of the tetrahedron and selective protein attachment to the vertices (Figure 3.7).

Thermal stability of a PS-biotinylated double strand sequence was previously examined. Briefly, a PS-biotinylated DNA conjugated to STV had melting temperatures about 17 °C higher than strand with internal thymine biotin in 5 mM phosphate and 10 mM NaCl but 9.5 °C lower melting temperature then end conjugated streptavidin. This suggests that protein-DNA conjugates formed by PS modifications via backbone modifications have higher stability than those formed by modified bases. We further investigated the stability of PS modified and linker modified tetrahedrons via gel shift assay (Figure 3.8). Tetrahedrons, PS modified tetrahedrons, and biotin linker functionalized tetrahedrons were formed as described by slowly annealing 3 DNA strands slowly from 90 °C in a 1:3:3 ratio in 1x TAE-Mg buffer. The structures were concentrated by amicon to 1 μM and incubated at 25 °C for 3 days and characterized by non-denaturing gel shift assay.

Next, we further explore the compatibility of a backbone phosphorothioate modification with different DNA nanostructure designs. As mentioned in the introduction to this chapter, Goodman et al. (16) demonstrated a small DNA tetrahedron that consists

of 4 different strands, which each makes up one-half of the double helix that is each side of the tetrahedron. Since the double stranded DNA that makes up each side of the tetrahedron maintains its B-DNA formation, it is possible to predict where the backbone will be pointed “inside” the tetrahedron and when it will be pointed “outside.” This is an advancement over using nicks in the DNA double strand to introduce a sticky end since it does not lower the melting temperature of the structure and can, in theory, introduce many modifications without disrupting the structure.

In a simple demonstration of the orientation control of the protein cargo with respect to the tetrahedron, we introduced a series of phosphorothioate modifications to one side of the simple tetrahedron, functionalized the PS modification with biotin linkers as described above, assemble the structure as previously reported by Goodman and others, and finally incubated with streptavidin. Figure 3.9 shows the result of this experiment. We expect that if the protein is partially or fully orientated inside the tetrahedron, the overall dynamic radius will be smaller than if the protein was orientated outside of the tetrahedron. This difference can be directly characterized by a native PAGE gel shift assay where the distance traveled by the structures within the gel matrix is a function of structure size (molecular weight and secondary/tertiary structures) and charge density. Assuming the charge density is equivalent between a protein is inside or outside the tetrahedron, we can assume that a tetrahedron with a protein partially or fully within the structure will travel a greater distance within the gel matrix than a structure with a protein protruding from the side. This difference is observed in the PAGE image (Figure XX) and fits well with the predicted DNA double helix twist, where a complete rotation is repeated every 10.5 bases.

Finally, in a demonstration of the potential application of such DNA tetrahedral as an *in vitro* or *in vivo* delivery vehicle for therapeutic agents, the release of the protein from the tetrahedron structure is demonstrated.

To facilitate the release of streptavidin from the structure, we took advantage of a biotin-analogue, desthiobiotin, which exhibits a 1000 times lower binding affinity to streptavidin then biotin. A deeper discussion into desthiobiotin and linker design will be presented in the following chapter. Here, it remains suffice to mention that by replacing the biotin moiety on the bifuncitonal linker with a desthiobiotin, the streptavidin can bind to desthiobiotin but in the presence of a sufficient concentration of biotin, the desthiobiontin is competitively replaced and leads to the release of the protein from the tetrahedron. Figure 3.10 shows a gel shift assay of a tetrahedron structure prepared with desthiobiotin modified linkers at the same PS sites as the previously described, biotin functionalized linker. Here, when the protein decorated structure is treated with a solution of biotin overnight, the higher molecular weight products that indicate the decoration of the tetrahedron with one or more protein disappears and a single, lower molecular weight product appears. This band corresponds well to the non-PS modified tetrahedron, representing that the proteins had been successfully removed from the structure with excellent yield.

Future work (discussed in Chapter 4) will explore the selectivity of this competitive binding between streptavidin-desthiobiotin and streptavidin-biotin.

3.3 Conclusions

We have successfully demonstrated one of the most important claims of why phosphorothioate DNA modifications is an excellent candidate for the decoration of complex DNA nanostructures, mainly that it introduces minimal disruptions to the Watson-Crick base pairing and the ultimate stability of the DNA nanostructures. In this work, we have demonstrated the decoration of two different tetrahedron nanostructures using PS-modified DNA strands with multiple cargoes, demonstrated the orientation control over the cargo inside or outside of the tetrahedron, and finally, the release of the tetrahedron from the tetrahedron structure for possible applications for *in vitro* or *in vivo* therapeutic applications. This technique has demonstrated wide applicability in DNA tiled assemblies in both two and three dimensions and should find further applications in decoration of more complex, tile based DNA structures. However, with the introduction of the DNA origami structures by Rothemund in 2006, one of the fundamental challenges in addressability within a DNA structure was solved. The origami method will be discussed in detail in Chapter 4. (27)

3.4 Experimental Details

Materials. Biotin polyethyleneoxide iodoacetate was purchased from Sigma-Aldrich (B2059) and used as received. The PS modified central strand (10 μM) was incubated in 1x TAE-Mg^{2+} buffer with 4 mM of BPI at 50 °C for 5 hours. After incubation, excess salt and linker was removed by washing 15 times with millipore water using a 100 kDa Amicon. The conjugated DNA was analyzed by mass spec (MALDI-TOF) to confirm successful conjugation.

DNA (He's tetrahedron). DNA sequences were adapted from previous works, which were originally designed by a computer program "SEQUIN" (Seeman, N. C. *J. Biomol. Struct. Dyn.* **1990**, *8*, 573-581). All oligonucleotides were HPLC purified and purchased from IDT, Inc (Coralville, IA). Long strand: AGG CAC CAT CGT AGG TTT TTC TTG CCA GGC ACC ATC GTA GGT T*T*T* TCT TGC CAG GCA CCA TCG TAG GTT TTT CTT GCC ; medium strand: TAG CAA CCT GCC TGG CAA GCC TAC GAT GGA CAC GGT AAC GCC; short peripheral strand: TTA CCG TGT GGT TGC TAG GCG. *denotes a phosphorothioate bond.

DNA (Goodman's tetrahedron). Side 1: AGG CAG TTG AGA CGA ACA TTC CTA AGT CTG AAA TTT ATC ACC CGC CAT AGT AGA CGT ATC ACC; Side 2 – CTT GCT ACA CGA TTC AGA CTT AGG AAT GTT CGA CAT GCG AGG GTC CAA TAC CGA CGA TTA CAG; Side 3 – GGT GAT AAA ACG TGT AGC AAG CTG TAA TCG ACG GGA AGA GCA TGC CCA TCC ACT ACT ATG GCG; Side 4 – CCT CGC ATG ACT CAA CTG CCT GGT GAT ACG AGG ATG GGC ATG CTC TTC CCG ACG GTA TTG GAC.

As synthesized central PS-DNA strand from IDT has a calculated mass of 23956.6 g/mole and a measured mass of 23957.7 g/mole. Biotin polyethyleneoxide iodoacetate has a mass of 542.43 g/mole and the product of the reaction has a predicted mass of 24373, 24788, and 25204 g/mole for PS-DNA conjugated with 1, 2, and 3 linkers, respectively. Mass spectroscopy confirms successful conjugation of biotin polyethyleneoxide iodoacetate linker to PS-DNA with major peaks at 24350, 24813, and 25211 g/mol. PS-DNA mass spec supplied by IDT, biotinylated DNA analysis performed at UIUC Mass Spec Lab on a Voyager-DE STR (Applied Biosystems).

Desthiobiotin modification. The concentration of DNA was calculated based on absorption at 280 nm according to the Beer-Lambert law. and adjusted to 100 µM. A 10 µM solution of 5` thiol modified DNA (used as received from IDT) was incubated with 2 µL of tributylphosphine solution for 2 hours at room temperature to the reduce the disulfide bond. Next, a 35 mM solution of desthiobiotin polyethyleneoxide iodoacetamide was freshly prepared in a 1 x TAE-Mg2+ buffer (Tris, 40 mM; acetic acid, 20 mM; EDTA, 2 mM; and magnesium acetate, 12.5 mM; pH 8.0) and incubated for 5 hours at 50 °C. Excess linkers were removed by washing 10 times with water using a 30 MWCO Amicon centrifugal filter. To purify the desthiobiotin functionalized product, the washed and concentrated solution was incubated with avidin agarose beads and eluted following manufacturers suggested protocols.

Affinity Purification of Biotinylated PS-DNA. Biotin functionalized PS-DNA was purified from unmodified sequences using an avidin-agarose affinity column (Sigma-Aldrich, A9207). Briefly, after conjugation of biotin polyethyleneoxide iodoacetate to PS-DNA following above procedure, the product was washed 15 times with Millipore water using a 100 kDa Amicon to remove excess salt and unconjugated linkers. The desalted product was diluted in 1 mL of 1x PBS buffer (binding buffer, 50 mM NaCl, pH 7.2) then incubated with 1mL of avidin-agarose matrix for 2 hours at 25 °C. The matrix was washed with 15 mL of binding buffer to remove unmodified DNA. After washing, the matrix was incubated in 1.5 mL of 10 mM EDTA adjusted to pH 8.2 for 10 minutes at 90 °C and immediate eluted to recover biotinylated PS-DNA strands. The eluted product was washed 10x with DI water with a 100 kDa Amicon to remove excess EDTA and adjusted to 3.3 µM as determined by UV absorbance at 260 nm.

PAGE Purification. Biotinylated tetrahedrons with 1 conjugated protein were purified by 4% native PAGE. The band corresponding to tetrahedron + 1 STV was cut, recovered, and eluted at 4 °C in 0.5x TAE-$Mg2^{+}$ buffer for 12 hours, changing buffer at 4 hour intervals. Finally, the recovered structures were concentrated before imaging. Aggregation found during imaging likely due to streptavidin crosslinking during and after purification process.

AFM imaging. A 3 µL drop of DNA solution was spotted onto freshly cleaved mica surface, and kept for 10 s to achieve strong adsorption. The sample drop was then washed with 30 mM magnesium acetate solution, and dried by nitrogen. DNA samples were imaged in AC mode on an Asylum Cypher AFM in air using oxide-sharpened silicon probes having a resonance frequency in the range of 280–320 kHz (MikroMasch–NSC15). Fluid imaging was performed using nitride probes having a resonance frequency of 21-52 kHz (Olympus -TR400PSA). The tip–surface interaction was minimized by optimizing the scan set-point to the highest possible value. AFM imaging was performed at 22 °C. AFM data was processed with IGOR Pro software.

3.5 References

(1) Seeman, N. C. *Angew. Chem. Int. Edit.* **1998**, *37*, 3220-3238.

(2) Seeman, N. C. *J. Theor. Biol.* **1982**, *99*, 237-247.

(3) Fu, T. J.; Seeman, N. C. *Biochemistry* **1993**, *32*, 3211-3220.

(4) LaBean, T. H.; Yan, H.; Kopatsch, J.; Liu, F. R.; Winfree, E.; Reif, J. H.; Seeman, N. C. *J. Am. Chem. Soc.* **2000**, *122*, 1848-1860.

(5) Mao, C. D.; Sun, W. Q.; Seeman, N. C. *J. Am. Chem. Soc.* **1999**, *121*, 5437-5443.

(6) Winfree, E. *Journal of Biomolecular Structure & Dynamics* **2000**, 263-270.

(7) Barish, R. D.; Rothemund, P. W. K.; Winfree, E. *Nano Lett.* **2005**, *5*, 2586-2592.

(8) Yan, H.; Park, S. H.; Finkelstein, G.; Reif, J. H.; LaBean, T. H. *Science* **2003**, *301*, 1882-1884.

(9) Fu, A. H.; Micheel, C. M.; Cha, J.; Chang, H.; Yang, H.; Alivisatos, A. P. *J. Am. Chem. Soc.* **2004**, *126*, 10832-10833.

(10) Le, J. D.; Pinto, Y.; Seeman, N. C.; Musier-Forsyth, K.; Taton, T. A.; Kiehl, R. A. *Nano Lett.* **2004**, *4*, 2343-2347.

(11) Li, H. Y.; Park, S. H.; Reif, J. H.; LaBean, T. H.; Yan, H. *J. Am. Chem. Soc.* **2004**, *126*, 418-419.

(12) He, Y.; Ye, T.; Su, M.; Zhang, C.; Ribbe, A. E.; Jiang, W.; Mao, C. D. *Nature* **2008**, *452*, 198-U41.

(13) Chen, J. H.; Seeman, N. C. *Nature* **1991**, *350*, 631-633.

(14) Zhang, Y. W.; Seeman, N. C. *J. Am. Chem. Soc.* **1994**, *116*, 1661-1669.

(15) Shih, W. M.; Quispe, J. D.; Joyce, G. F. *Nature* **2004**, *427*, 618-621.

(16) Goodman, R. P.; Schaap, I. A. T.; Tardin, C. F.; Erben, C. M.; Berry, R. M.; Schmidt, C. F.; Turberfield, A. J. *Science* **2005**, *310*, 1661-1665.

(17) Goodman, R. P.; Berry, R. M.; Turberfield, A. J. *Chem. Commun.* **2004**, 1372-1373.

(18) He, Y.; Su, M.; Fang, P.-a.; Zhang, C.; Ribbe, A. E.; Jiang, W.; Mao, C. *Angew. Chem. Int. Edit.* **2010**, *49*, 748-751.

(19) Shen, X. B.; Song, C.; Wang, J. Y.; Shi, D. W.; Wang, Z. A.; Liu, N.; Ding, B. Q. *J. Am. Chem. Soc.* **2012**, *134*, 146-149.

(20) Erben, C. M.; Goodman, R. P.; Turberfield, A. J. *Angew. Chem. Int. Edit.* **2006**, *45*, 7414-7417.

(21) Walsh, A. S.; Yin, H. F.; Erben, C. M.; Wood, M. J. A.; Turberfield, A. J. *ACS Nano* **2011**, *5*, 5427-5432.

(22) Schueller, V. J.; Heidegger, S.; Sandholzer, N.; Nickels, P. C.; Suhartha, N. A.; Endres, S.; Bourquin, C.; Liedl, T. *ACS Nano* **2011**, *5*, 9696-9702.

(23) Lee, H.; Lytton-Jean, A. K. R.; Chen, Y.; Love, K. T.; Park, A. I.; Karagiannis, E. D.; Sehgal, A.; Querbes, W.; Zurenko, C. S.; Jayaraman, M.; Peng, C. G.; Charisse, K.; Borodovsky, A.; Manoharan, M.; Donahoe, J. S.; Truelove, J.; Nahrendorf, M.; Langer, R.; Anderson, D. G. *Nat. Nanotechnol.* **2012**, *7*, 389-393.

(24) Lin, C. X.; Rinker, S.; Wang, X.; Liu, Y.; Seeman, N. C.; Yan, H. *Proc. Natl. Acad. Sci. U. S. A.* **2008**, *105*, 17626-17631.

(25) Delebecque, C. J.; Lindner, A. B.; Silver, P. A.; Aldaye, F. A. *Science* **2011**, *333*, 470-474.

(26) He, Y.; Ye, T.; Su, M.; Zhang, C.; Ribbe, A. E.; Jiang, W.; Mao, C. *Nature* **2008**, *452*, 198-U41.

(27) Rothemund, P. W. K. *Nature* **2006**, *440*, 297-302.

3.6 Figures

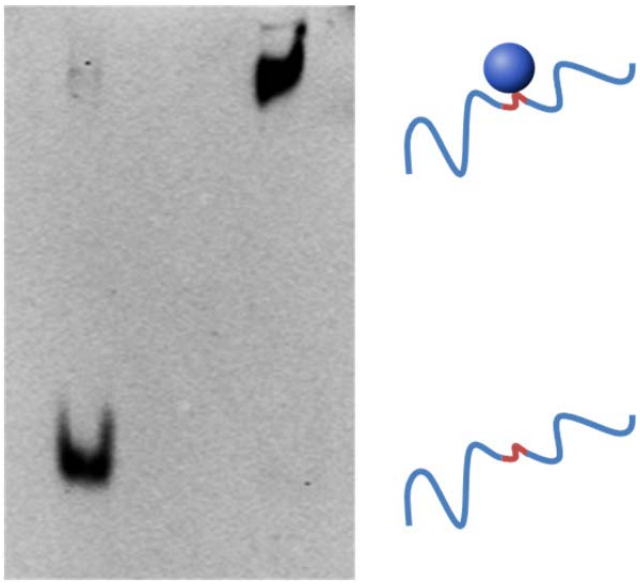

Figure 3.1 Polyacrylamide gel shift assay. (Left band) Purified DNA-linker conjugate and (right lane) DNA-linker conjugate with streptavidin.

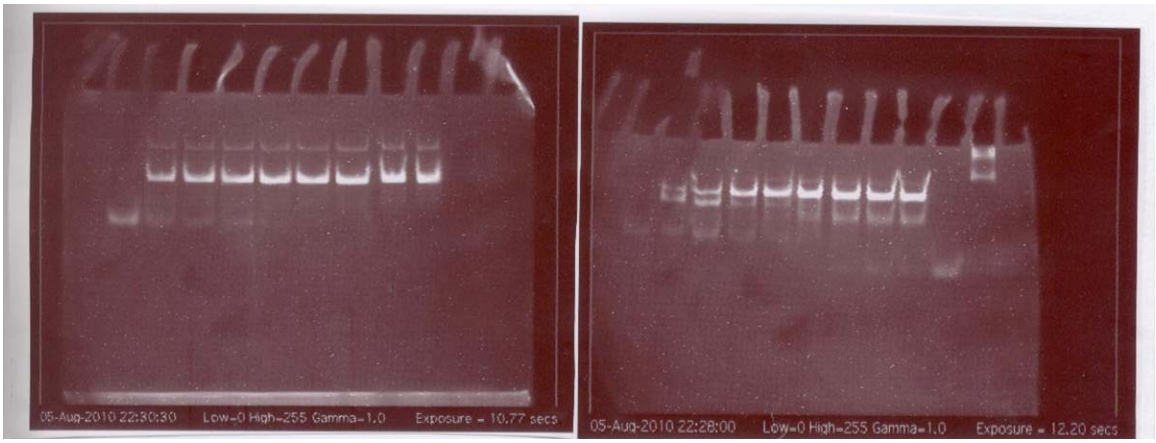

Figure 3.2 Polyacrylamide gel titration assay to optimize volume ratios between strands. The rightmost band shows a phosphorothioate modified 3-arm motif intermediate decorated with a streptavidin protein.

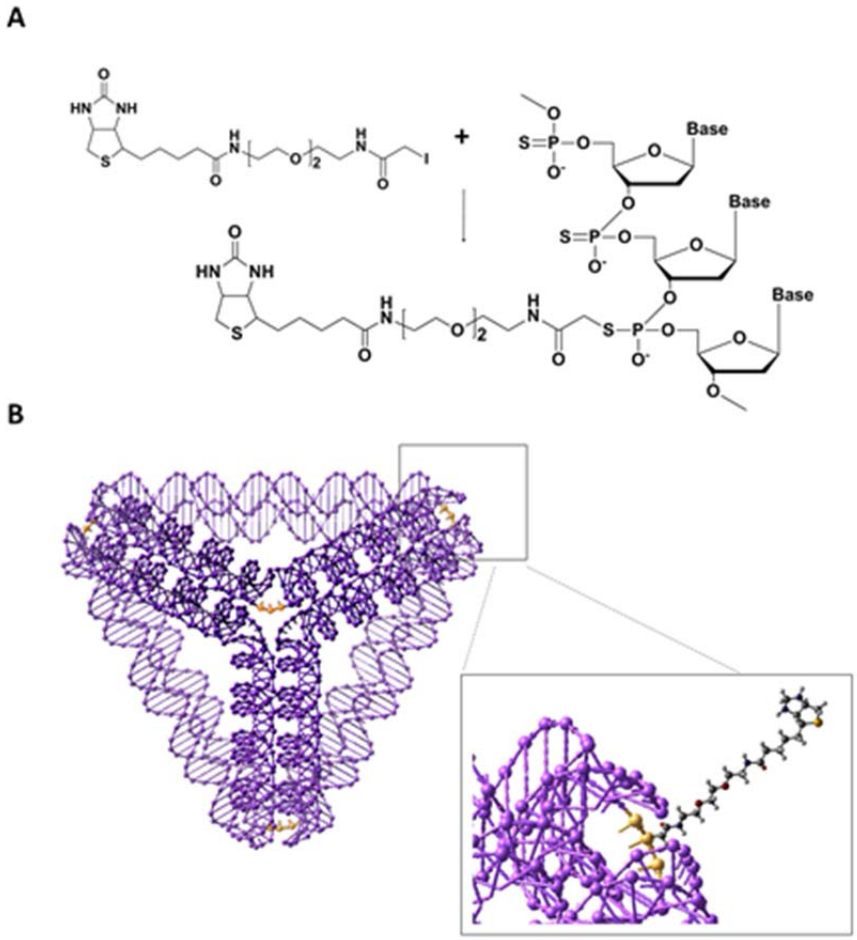

Figure 3.3 (A) Chemical structure of a phosphorothioated DNA backbone and its subsequent covalent conjugation with the biotin polyethyleneoxide iodoacetamide bifunctional linker. (B) 3D schematic of formed tetrahedron structure with PS bonds represented in orange before and after conjugation.

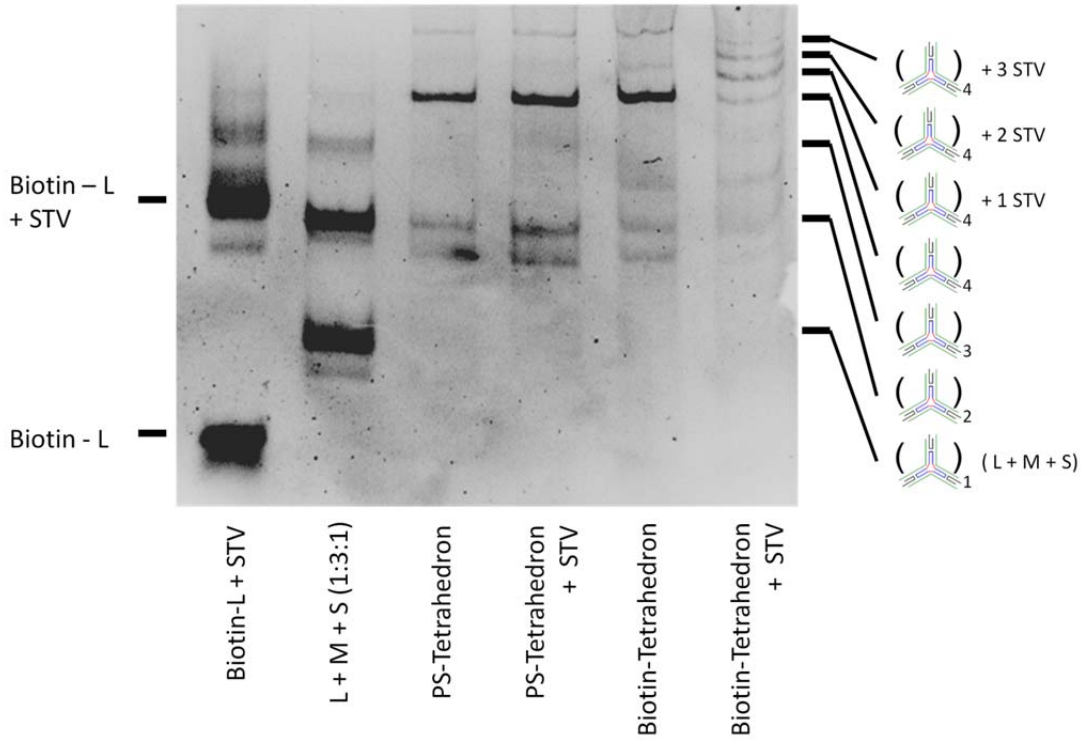

Figure 3.4 Complete gel shift assay characterizing pre-purified PS/Linker modified DNA (lane 1), 3 arm motif intermediates (lane 2), unmodified tetrahedron structures (lane 3), reaction between streptavidin and un-modified tetrahedrons (lane 4), PS/Linker modified tetrahedrons (lane 5), and streptavidin decoration of PS/Linker modified tetrahedrons (lane 6). In lane 6, 4 high molecular weight bands can be observed, corresponding to tetrahedrons with 0, 1, 2, and 3 proteins attached. Notably absent is the 5th band that would correspond to a tetrahedron with 4 proteins conjugated.

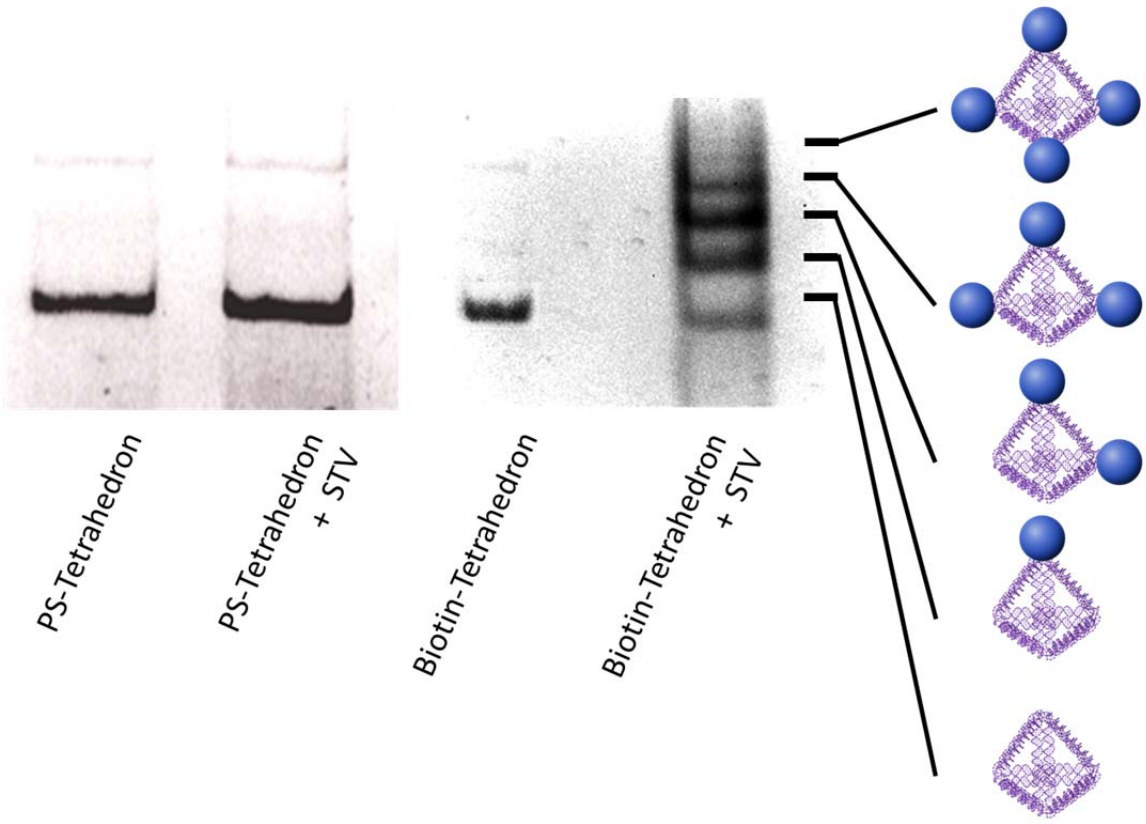

Figure 3.5 Gel shift assay showing the completed, purified PS-tetrahedron before and after streptavidin (STV) incubation (lane 1 and 2) and the biotin functionalized tetrahedron before and after streptavidin incubation (lane 3 and 4). In lane 4, 5 bands are observable, corresponding to a DNA tetrahedron with 0, 1, 2, 3, and 4 protein conjugated to the vertexes.

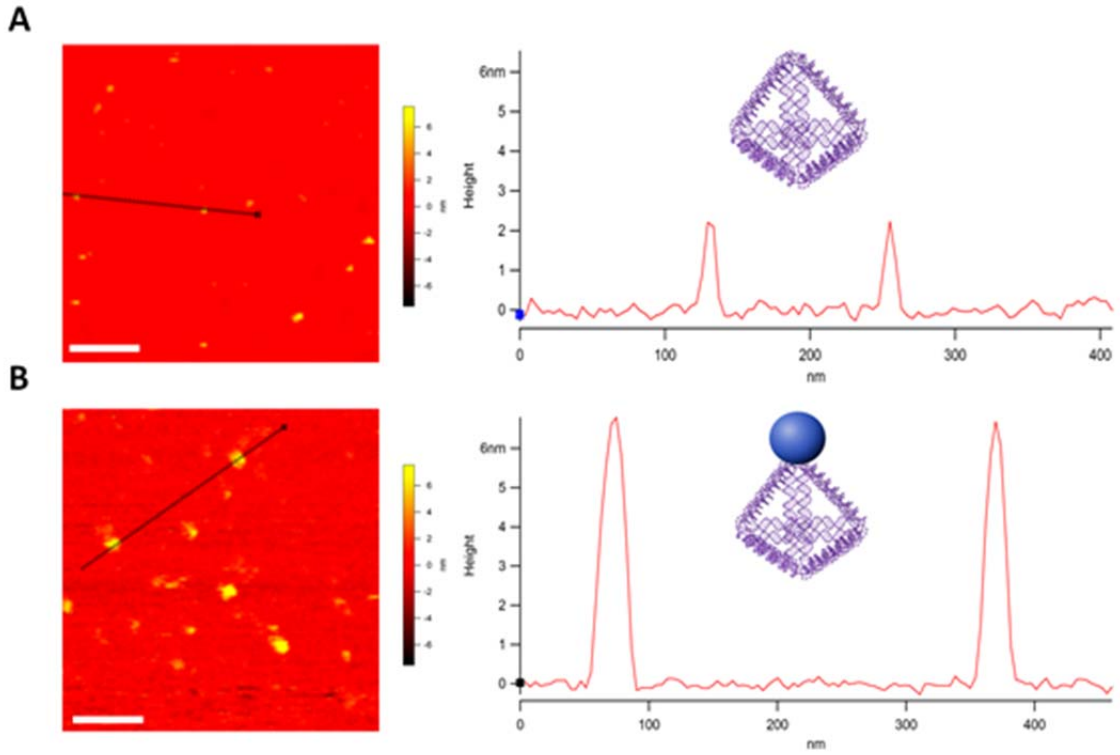

Figure 3.6 AFM and cross section of DNA tetrahedron A) before and B) after incubation with streptavidin. The nanostructures without protein are well dispersed with average height of ~2 nm. After incubation, nanostructure size increases by ~4 nm to ~6 nm, indicating successful protein(s) conjugation, in good agreement with a measured protein size of ~4.5 nm. Scale bar represents 100 nm.

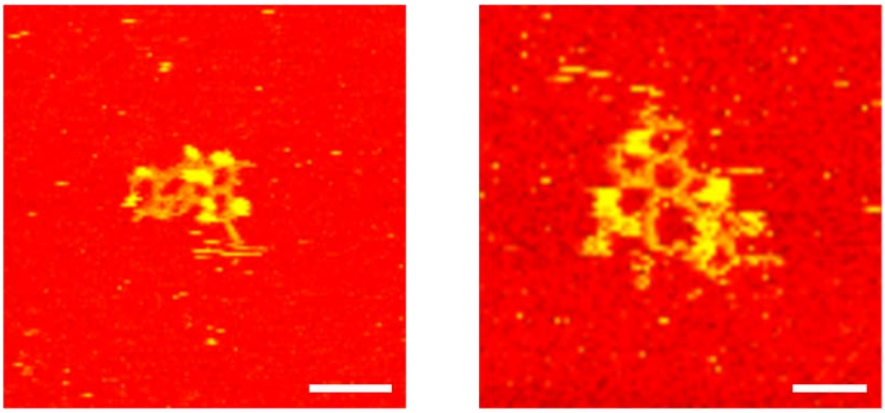

Figure 3.7 Fluid AFM imaging reveals some larger 2D structures adsorbed onto the mica. These structures have formed 2D hexagonal array based on the 3 point star motif and due to the biotin functionalization at the vertices, we can clearly see the streptavidin preferably binding to the array at the vertices. Smaller tetrahedrons likely do not bind well to the surface in liquid and cannot be imaged reproducibly. Scale bar represents 100 nm.

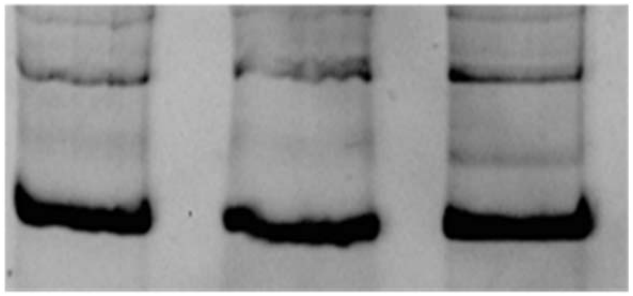

Figure 3.8 Stability comparison between unmodified and PS/Linker modified tetrahedrons stored at room temperature for 3 days. (Left) unmodified, (middle) PS-modified, and (right) biotin-linker modified.

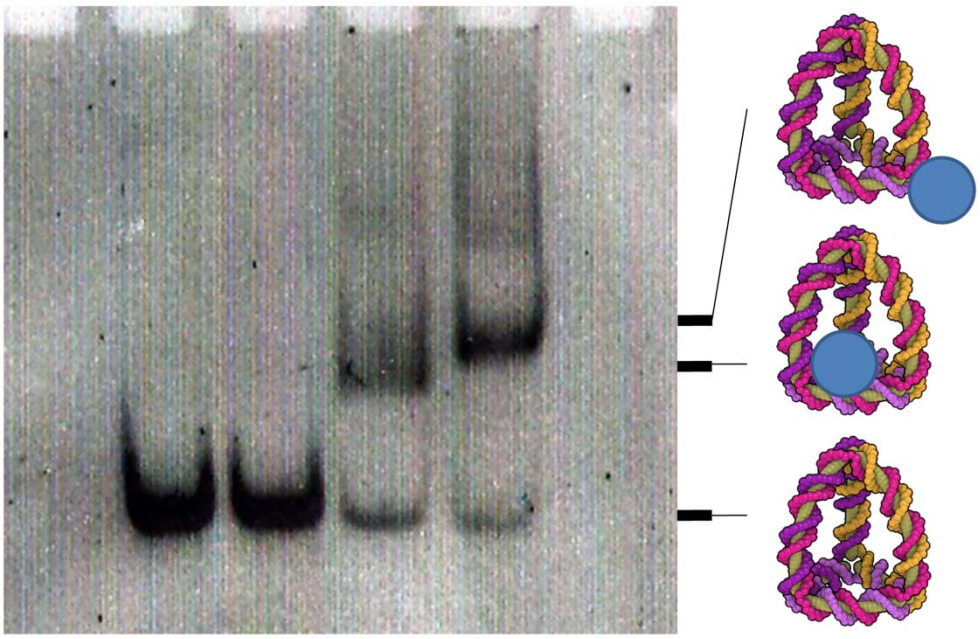

Figure 3.9 Gel shift assay characterizing Goodman's tetrahedron, consisting of 4 DNA strands that each form half of one side of the tetrahedron (Lane 1). Phosphorothioate modifications were placed at the vertices and along the side of the tetrahedron on one of the sides (Lane 2). By taking accounting for the rotation of the double helix, it is possible to position the linker modification outward or inside the tetrahedron. If the modification is placed facing inward, the overall tetrahedron-protein conjugate is smaller (lane 3). If the modification is placed facing outward, the overall tetrahedron-protein conjugate is larger (lane 4).

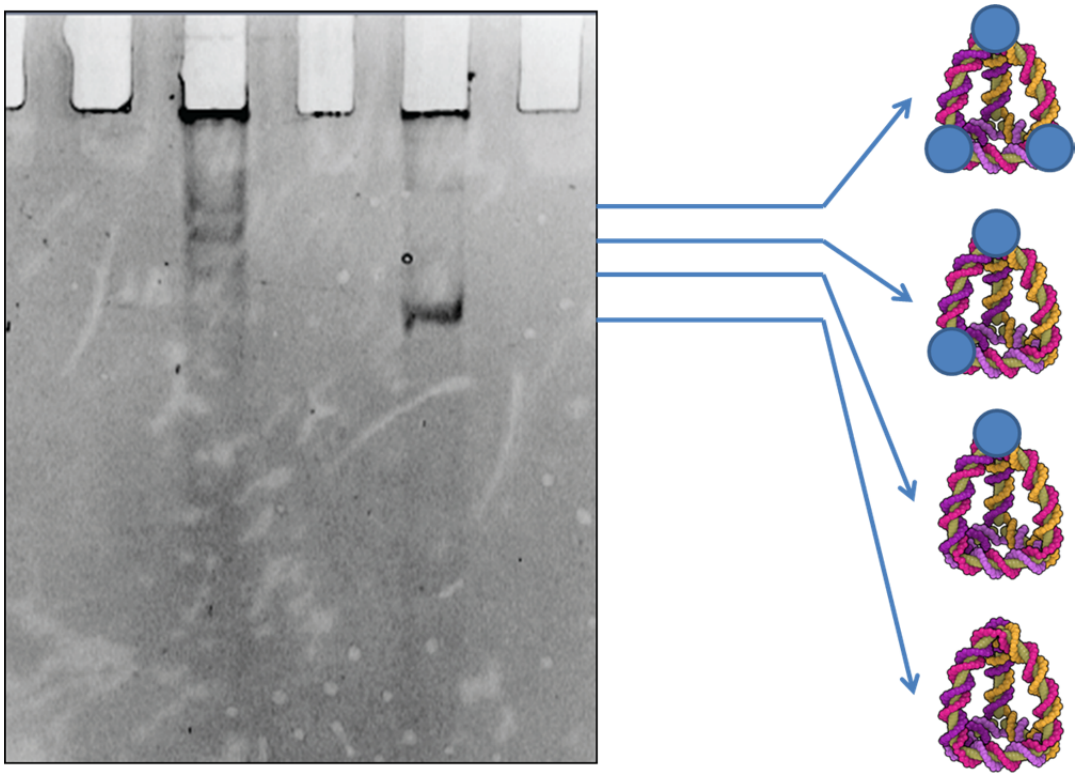

Figure 3.10 Gel shift assay demonstrating that by using a linker incorporating a biotin-analogue, it is possible to attach (left lane) and remove streptavidin proteins from the tetrahedron structure (right lane). This mechanism is further discussed in Chapter 4 of this thesis.

CHAPTER 4

DYNAMIC CONJUGATION OF CARGO TO DNA ORIGAMI TILES – NANO-MORSE CODE AND DELIVERY APPLICATIONS

Significant portions of this chapter were prepared as “Nano-Encryted Morse Code: A Versatile Approach to Programmable and Reversible Nanoscale Assembly and Disassembly” Ngo Yin Wong, Hang Xing, Li Huey Tan, and Yi Lu, *Journal of the American Chemical Society* **2012** submitted.

4.1 Introduction

This chapter continues the discussion of self-assembly of nanoscale objects on a DNA template. In this chapter, we discuss and explore one of latest advances in DNA based nanostructures, DNA origami, and its applications for addressable assembly with nanoscale precision. As was mentioned in Chapter 2 of this thesis, there are two main strategies toward the assembly of DNA nanostructures, tile based and origami. The main advantages of tile based assembly is the ability to generate large, two and three dimensional crystals based on rigid tiles with sticky ends. Tile based assembly, however, suffer from a number of inefficiencies that have limited their use in the broader scientific community. Mainly, the multi-armed tiles described by Seeman and coworkers do not allow a great deal of design freedom, requires careful radiometric titration to obtain high quality structures, and requires a long annealing process (24 to 48 hours). In 2006, Paul Rothemund was the first to describe the complete idea of DNA origami. While the

principles behind DNA origami have been proposed previously by others (1), the demonstration of its full potential remained unrealized. Rothemund, demonstrated for the first time, that by using a long naturally single stranded DNA (m13mp18, 7.8k base pairs) extracted from bacteria, hundreds of unique helper / staple sequences (usually 30 – 40 base pairs) would hybridize and fold a particular section of the long single strand. Repeated hundreds of times, a particular set of stable strands will direct the folding of the long strand into a predetermined, arbitrary, and discreet shape. In his original publication, Rothemund demonstrated this by designing and assembling a series of shapes such as a star, rectangle, and squares to more intricate shapes such as a map of the world and a smilie face. The origami technique jumpstarted the DNA structural community and over the next several years, we saw the rise of three distinct classes of publications based on the DNA origami technique: origami tiles as a template for nanomaterials, extended two and three dimensional structures, and active nano-mechanical devices.

One of the most difficult and least explored areas of DNA nanostructures remains the design and assembly of discreet, three dimensional structures. Anderson *et al.* (2) demonstrated one of the earliest 3D structures in the form of a 42 nm x 36 nm x 36 nm box with a controllable lid, which can be opened using a DNA ‘key.’ Shih, Yan, and colleagues next developed a more general strategy toward 3D structures (3) by systematically folding pleated layers of helices constrained into honeycomb (4), square (5), and hexagonal lattices (6). Dongran and coworkers (7) demonstrated the versatility of this approach by designing and assembling a 100 nm Mobius strip, supercoiled rings, and catenane structures through a fold-and-cut strategy. However, the assembly of these

exotic and complex structures suffered from yields of only ~ 20%, rendering them more a research wonder than a practical tool for further studies. In a surprising study, Jean-Philippe and coworkers (8) found that nothing happens throughout most of the annealing / assembly process, but rather, at a critical temperature, the origami tiles forms very rapidly and if the temperature is held at this critical temperature, even highly complex three dimensional structures can form will yields close to 100% within an hour. In this chapter, we will also present our data on the mechanistic studies of 2D origami tiles.

Very recently, Wei *et al.* (9) published a follow-up to the origami technique that is expected to generate new excitement in the field. One of the limiting steps in Rothemund's origami method is the single stranded bacteriophage DNA that cannot be obtained artificially and accounts of a considerable portion of the costs. By designing and using single stranded tiles (SST), Wei *et al.* circumvented this shortfall by using hundreds, and up to thousands of short single strands that act as tiles by associating with up to 4 other strands to form the desired shape.

In order for assembled DNA nanostructures to be applicable in directed self-assembly of nanomaterials, a conjugation method between the nanomaterial and the DNA scaffold is needed. The reader is directed to an excellent review by Sacca and Niemeyer (10) for an in-depth review of recent advances in DNA-protein hybrids. Some of the highlighted chemistries include nitrilotriacetic acid (NTA), aptamers, alkylthiol-amine and alkylthiol-thiol chemistries. Unsurprisingly for people familiar with the field, one of the most commonly used conjugation technique is the (strept)avidin-biotin complex. With a disassociate constant of roughly 10^{-15} M, it ranks among one of the strongest non-

covalent bond found in nature and is mostly a result of hydrophobic interactions and hydrogen bonding. With a staggeringly high affinity for binding, mild conjugation conditions, and widely available commercial products, the biotin-streptavidin conjugation is the often the proof of concept chemistry for nanoscale assemblies to achieve high yields. However, one of the drawbacks of this reaction is that due to the strong binding, removing the protein from biotin requires a combination of high temperature, extreme pH, and other chaotropic elements are required to disrupt it. Since these disruptive forces often destabilize or even destroy the materials on which the conjugation pair reside (e.g., double stranded DNA, proteins, nanoparticles) such a reaction is incompatible for many systems for which dynamic and reversible assembly and disassembly are of interest.

Programmable assembly of functional materials at the nanometer scale with designed patterns has received increasing attention in scientific research and engineering, because of its potential applications in electronics, photonics, and medicine. An excellent example of recent success in programmable assembly of nanomaterials was the development of structural DNA (11) and DNA origami (12,13) as a template for assembly of functional components such as nanoparticles (14-17), quantum dots (18,19), carbon nanotubes (20), and proteins (21-24). More recent advances in design (3,25), large scale patterning (26), and assembly of DNA origami structures in 1D (27), 2D (28,29) and 3D (2,30) offer a path towards practical applications. While tremendous progress has been made in the assembly of these components with excellent spatial resolution, a significant gap remains in our ability to achieve selectively reversible assembly of certain component(s) at selective site(s); exerting such a control of the assembly process will

make it possible to fine-tune the functional properties of the assembly and to realize more complex designs by replacing one component of the assembly with another in subsequent assembly steps.

Reversible processes are common in biology as well as in large-scale engineering systems, serving many important functions. For example, the reversible process in protein synthesis makes it possible to proof-read and correct errors in incorporation of wrong amino acids with a similar structure. Despite many such examples of programmable, reversible control of the processes both in biology and in bulk-scale engineering systems, very few processes in nanoscale assembly demonstrate similar controllability. (31-34) One successful strategy to achieve selective, reversible nanoscale binding is through the use of complementary DNA, invasive DNA strands, or toe-hold DNA designs. These techniques have been widely applied for use in DNA walkers and DNA motors that follow preprogrammed paths. (35-38) While the technique is useful, the use of DNA hybridization-based conjugation is limited to buffered conditions similar to that found in the cellular environment. In contrast, covalent conjugation techniques form stable linkages but typically suffer from lower yields and require specific reaction conditions. Consequently there are few examples of completely reversible bonding under mild conditions.

An early motivation for the current work lies with a key semiconductor processing technique: lift-off. One of the most important concepts in complex top-down lithography, a pattern is defined on a surface via a polymer (usually a photoresist). The polymer is then selectively cross-linked and the un-crosslink sections are washed away

and a material is deposited. Afterwards, the cross-linked section is removed and the same process is repeated to generate a new pattern of a new material. The idea is that the same process can be repeated to generate increasingly complex patterns with multiple different materials. By using the same patterning technique (masking and lift-off) the overall complexity of the process is reduced. The goal of this project was to extend this process into the nanoscale by using a reversible chemistry to effective “mask” an area of a template, which can later be removed and be available of subsequent modifications, using the same chemistry. This process enables the ability to achieve dynamic assemblies that are responsive to their environment, and if we can adopt a widely used chemistry for this purpose, the applications can be wide reaching. Today, one of the main strategies toward responsive assemblies or “robots” has been the use of competitive DNA hybridization. The idea is simple; a strand hybridized to a second strand can be displaced by a third strand if there are more complementary base pairs between the two strands. This process can be encouraged further with the introduction of toe-holds, protruding single stranded regions by lowering the activation energy for the competitive binding by giving the invading strand a favorable site to initiate hybridization. This technique has been extensively explored by researchers interested in molecular robots. (35) While DNA satisfies many of the requirements for basic research, it remains a niche research curiosity for the wider research community. One reason is likely the relatively low thermal stability and the need for buffered conditions to maintain the double-stranded helix of DNA.

On the other hand, the biotin-(strept)avidin conjugation pair is widely used in nanoscale science and technology today, thanks to the conjugation’s exceptional stability

and selectivity while requiring only mild conditions. As a result; it is commonly used to functionalize nanomaterials such as metal nanoparticles, quantum dots, carbon nanotubes, and proteins, as well as on a variety of surfaces, many of which are available commercially. A significant shortcoming of this conjugation, however, is its near irreversibility. Due to the extraordinarily strong binding affinity of the interaction (K_d ~ 10^{-15} M), Desthiobiotin, with a binding affinity to streptavidin ~1000 times weaker than biotin (K_d ~ 10^{-11} M), has long been used with solid supports to purify biotin-binding proteins under mild conditions by competition with free biotin in solution, but to our knowledge has not yet been exploited for nanoscale assembly. To demonstrate its utility in selective and reversible assembly, we first compared the binding of biotinylated and desthiobiotinylated DNA strands with streptavidin.

4.2 Results and Discussion

Desthiobiotin, with a binding affinity to streptavidin ~1000 times weaker than biotin, has long been used with solid supports to purify biotin-binding proteins under mild conditions and released through competition with free biotin in solution, (39,40) but to our knowledge has not yet been exploited for nanoscale assembly. To demonstrate its utility in selective and reversible assembly, we first compared the binding of biotinylated and desthiobiotinylated DNA strands with streptavidin. To introduce desthiobiotin onto the DNA, an oligonucleotide bearing a dithiol on the 5` end was first incubated with 5 mM tributylphosphine in 1x TAE-$Mg^{2+}$ to reduce disulfide bonds to expose a reactive thiol moiety at the 5` end. The resulting HS-DNA was then reacted with desthiobiotin

polyethyleneoxide iodoacetamide for 5 hours at 20 °C. After purification by 100k MWCO Amicon, mass spectrometry was used to confirm that 90% of DNA strands were successfully conjugated with desthiobiotin (see supplemental information). To achieve 100% purity, the above mixture was purified via an avidin agarose affinity column following manufacturer's instructions. The final product was confirmed by a gel shift assay. It is noted that desthiobiotinylated oligonueoclides are now available commercially through Integrated DNA technology.

To illustrate the binding activity and release of streptavidin from the functionalized DNA, either biotinylated or desthiobiotinylated DNA strands were incubated with 1 μM streptavidin for 2 hours at room temperature, the mixtures were then treated with 5 mM biotin in 1x TAE buffer overnight and analyzed by a gel shift assay. As shown in Figure 1B, upon incubation with streptavidin, both biotinylated and desthiobiotinylated DNA strands in Lanes 1 and 2 transformed into discrete, higher molecular weight products (see Lanes 3 and 4), indicating specific conjugation of the streptavidin with both DNA strands. In contrast, subsequent treatment of both conjugates with excess biotin at room temperature resulted in a different migration of the bands on the gel; while addition of excess biotin did not change the position of the biotinylated DNA strand, the addition under the same condition resulted in a complete reversal of the conjugated high molecular band to the lower molecular weight of free desthiobiontinylated DNA. These results reveal the competitive binding mechanism whereby biotin specifically replaces the weaker binding desthiobiotin from streptavidin, effectively reversing the conjugation process. The process was repeated by recovering the

free desthiobiotinylated DNA strand and again incubating with free streptavidin, confirming that the binding is fully reversible and that no observable degradation of desthiobiotin occurred during the process (Figure 5.2).

Having demonstrated full reversibility of the desthiobiotinylated DNA system, we then explored its application in reversible nanoscale assemblies on a rectangular 100 x 70 nm^2 DNA origami tile prepared by folding the single-stranded 7,249 base DNA genome of the bacteriophage M13mp18 in the presence of 226 shorter "staple" strands. (12) Because each of the 226 strands is uniquely indexed on the tile, site-specific modification on the DNA origami tile is a simple process of picking and functionalizing the desired strands based on a diagram of the staple strands. The resulting patterns on each tile can be revealed by incubating the tiles with streptavidin and then obtaining the images under atomic force microscope.

As a first demonstration of this methodology, we investigated the application of this methodology towards the encryption of a message written in Morse code at the nanoscale. Invented in the 1840's, Morse code was the prevalent language of telecommunication for most of the 19^{th} and into the 20^{th} century. Consisting of a series of dots and dashes that make up the alphabet, we constructed a message using proteins while simultaneously "encrypting" the message with excess proteins (Figure 5.3). To design the nano-Morse codes, a "primary" pattern or masked message is first defined by selecting a series of staple strands that gives the best representation of the original design. Within this pattern of sequences, it is then possible to incorporate a "secondary" design, or hidden message or code. The secondary design consists of sequences that are modified

with biotin while the remaining staple strands of the primary design are functionalized with desthiobiotin. As a result, the primary design will be visible after streptavidin incubation and the secondary design or decoded message will be revealed after incubation in an excess solution of biotin.

To realize the encrypted Morse code, we designed an origami tile consisting of 9 desthiobiotinylated and 15 biotinylated staple strands to encode the word “NANO.” In the current design, each row represents one letter, with 2 proteins representing a dash and a single protein corresponding to a dot within Morse code. Translated, the encrypted message generated simply by incubating the tile with streptavidin represents a nonsensical encrypted message. However, upon subsequent addition of the biotin “decoder,” the original intended message “NANO” can be revealed (Figure 5.4).

Based on the above design, a combination of biotin and desthiobiotin modified staple strands representing specific positions within the origami scaffold, the modified staple strands, along with unmodified strands were annealed from 90 °C to 20 °C over 5 hours to form the desired origami structure. After the formed DNA tiles were filtered by 100k MWCO Amicon membranes to remove excess staple strands, the formed tiles were allowed to incubate with a 20 times excess of streptavidin overnight in 1x TAE-$Mg2^{+}$. Subsequent high resolution AFM reveals a 4x3 array of dashes (each consisting of 2 proteins) (Figure 2D), as predicted in our scheme. The measured height of the DNA tile and protein are 1.7 nm and 4 nm respectively, in excellent agreement with the known dimensions of these biomolecules.

Next, to demonstrate selective release of protein from origami template and thus

revealing of the nanoscale Morse code, the protein-decorated tiles were treated with biotin for 2 hours at room temperature. The AFM images in Figure 5.4 show that the addition of biotin was able to reveal the hidden Morse code message “NANO.”

AFM analysis of 8 well-formed, encrypted nano-Morse code tiles similar to those shown in Figure 2D reveal that 90% of the streptavidin had bound correctly (Figure 5.6). Interestingly, the percentage of the streptavidin bound correctly to biotin-modified staple strands was ~95% while the same tiles only had ~84% bound correctly to desthiobiotinylated modified strands. This discrepancy is likely due to the weaker binding affinity of desthiobiotin to streptavidin than biotin. Furthermore, even with minimal tapping force between the AFM probe and the sample, it is conceivable that some proteins were removed through tip interactions. Because of the differences in affinity for streptavidin, more desthiobiotin-bound streptavidin would be dislodged then the biotin-bound proteins. Following incubation with biotin solution to displace desthiobiotin-bound streptavidin, an analysis of 8 well-formed tiles similar to that shown in Figure 5.7 shows that approximately 96% of the proteins are correctly bound, confirming reversible assembly in high yield.

To further demonstrate the versatility and reversibility of the method described here, we designed an “I” pattern made of a combination of biotin and desthiobiotin modifications (Figure 5.5). The second design is inspired by the University of Illinois logo of a capital I. Upon addition of biotin, the lower case “i” can then be revealed. Furthermore, addition of streptavidin can restore display of the original capital letter. More importantly, due to the small separation between biotin and desthiobiotin

modifications, we were able to investigate whether the spacing between conjugated streptavidin would hinder the binding or release of the protein from desthiobiotin in the presence of excess biotin. Following similar procedures as before, we observed under AFM highly efficient formation of DNA origami rectangles with a clear capital “I” after initial incubation with streptavidin. Following overnight incubation with biotin at 4º C, more than 90% of the tiles were successfully converted to a lower case “i” pattern, demonstrating efficient and selective removal of proteins attached to desthiobiotin. To demonstrate the availability of desthiobiotin sites for subsequent functionalization, the system was again incubated with excess streptavidin. AFM imaging (Figure 5.5) shows greater than 70% of the desthiobiotin sites available on the tiles were bound to streptavidin, demonstrating the reversible nature of the conjugation.

In order for DNA origami to become an established technique in template directed self-assembly of nanomaterials, there is a need to gain mechanical insights into the formation of such a densely packed DNA structure.

4.3 Conclusions

In conclusion, we take advantage of the different binding affinities of biotin and desthiobiotin toward streptavidin and demonstrate for the first time selective and reversible deco-ration of DNA origami tiles with streptavidin. In the first demonstration of such a versatile approach, we showed that an encrypted Morse code message could be revealed after addition of biotin to replace desthiobiotin-bound streptavi-din. In a further demonstration of reversibility, a pattern of letter “I” can be replaced with “i” first, and

then restored back to “I”. The yields of the conjugations are high (> 90%) and the process is reversible. The technique presented here should find wide applications within the fields of nano-eletronics, photonics, and biomedicine where it is desirable for researchers to create nanoscale assemblies with pro-grammable capture and release of multiple nanomaterials.

4.4 Experimental Details

Chemicals and Materials. All Oligonucleotides used in the current study were purchased from Integrated DNA Technologies (Coralville, IA). M13 viral DNA was purchased from New England Biolabs, Inc. (#N4040S, NEB). Tributylphosphine solution (200 mM, in N-methyl-2-pyrrolidinone; Sigma-Aldrich), Desthiobiotin polyethyleneoxide Iodoacetamide (>90%, Sigma-Aldrich), Avidin agarose (6% beaded agarose, Thermo Scientific) Amicon centrifugal filter units (100,000 MWCO, Millipore). All buffer components were purchased from Sigma Aldrich unless otherwise noted.

Origami Design and Sequences.

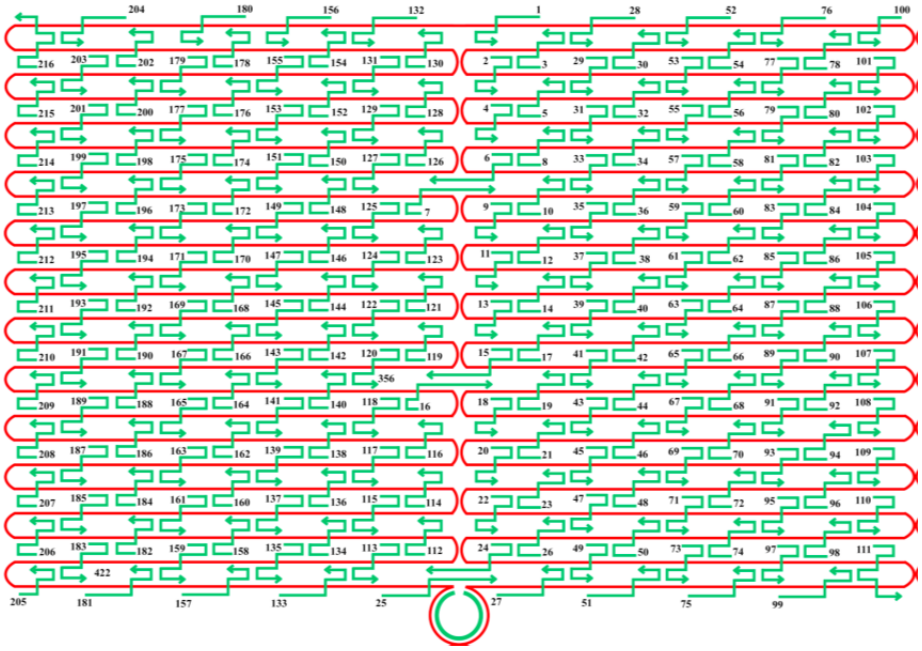

Table 4.1 Staple strands for 100 x 70 nm rectangular origami structure.

Sequence Name	Sequence
1	CAAGCCCAATAGGAAC CCATGTACAAACAGTT
2	AATGCCCCGTAACAGT GCCCGTATCTCCCTCA
3	TGCCTTGACTGCCTAT TTCGGAACAGGGATAG
4	GAGCCGCCCCACCACC GGAACCGCGACGGAAA
5	AACCAGAGACCCTCAG AACCGCCAGGGGTCAG
6	TTATTCATAGGGAAGG TAAATATT CATTCAGT
7	CATAACCCGAGGCATA GTAAGAGC TTTTTAAG
8	ATTGAGGGTAAAGGTG AATTATCAATCACCGG
9	AAAAGTAATATCTTAC CGAAGCCCTTCCAGAG
10	GCAATAGCGCAGATAG CCGAACAATTCAACCG
11	CCTAATTTACGCTAAC GAGCGTCTAATCAATA
12	TCTTACCAGCCAGTTA CAAAATAAATGAAATA

Table 4.1 (Continued)

13	ATCGGCTGCGAGCATG TAGAAACCTATCATAT
14	CTAATTTATCTTTCCT TATCATTCATCCTGAA
15	GCGTTATAGAAAAAGC CTGTTTAGAAGGCCGG
16	GCTCATTTTCGCATTA AATTTTTGAGCTTAGA
17	AATTACTACAAATTCT TACCAGTAATCCCATC
18	TTAAGACGTTGAAAAC ATAGCGATAACAGTAC
19	TAGAATCCCTGAGAAG AGTCAATAGGAATCAT
20	CTTTTACACAGATGAA TATACAGTAAACAATT
21	TTTAACGTTCGGGAGA AACAATAATTTTCCCT
22	CGACAACTAAGTATTA GACTTTACAATACCGA
23	GGATTTAGCGTATTAA ATCCTTTGTTTTCAGG
24	ACGAACCAAAACATCG CCATTAAATGGTGGTT
25	GAACGTGGCGAGAAAG GAAGGGAACAAACTAT
26	TAGCCCTACCAGCAGA AGATAAAAACATTTGA
27	CGGCCTTGCTGGTAAT ATCCAGAACGAACTGA
28	CTCAGAGCCACCACCC TCATTTTCCTATTATT
29	CTGAAACAGGTAATAA GTTTTAACCCCTCAGA
30	AGTGTACTTGAAAGTA TTAAGAGGCCGCCACC
31	GCCACCACTCTTTTCA TAATCAAACCGTCACC
32	GTTTGCCACCTCAGAG CCGCCACCGATACAGG
33	GACTTGAGAGACAAAA GGGCGACAAGTTACCA
34	AGCGCCAACCATTTGG GAATTAGATTATTAGC
35	GAAGGAAAATAAGAGC AAGAAACAACAGCCAT
36	GCCCAATACCGAGGAA ACGCAATAGGTTTACC
37	ATTATTTAACCCAGCT ACAATTTTCAAGAACG
38	TATTTTGCTCCCAATC CAAATAAGTGAGTTAA
39	GGTATTAAGAACAAGA AAAATAATTAAAGCCA
40	TAAGTCCTACCAAGTA CCGCACTCTTAGTTGC
41	ACGCTCAAAATAAGAA TAAACACCGTGAATTT
42	AGGCGTTACAGTAGGG CTTAATTGACAATAGA
43	ATCAAAATCGTCGCTA TTAATTAACGGATTCG
44	CTGTAAATCATAGGTC TGAGAGACGATAAATA
45	CCTGATTGAAAGAAAT TGCGTAGACCCGAACG
46	ACAGAAATCTTTGAAT ACCAAGTTCCTTGCTT
47	TTATTAATGCCGTCAA TAGATAATCAGAGGTG

Table 4.1 (Continued)

48	AGATTAGATTTAAAAG TTTGAGTACACGTAAA
49	AGGCGGTCATTAGTCT TTAATGCGCAATATTA
50	GAATGGCTAGTATTAA CACCGCCTCAACTAAT
51	CCGCCAGCCATTGCAA CAGGAAAAATATTTTT
52	CCCTCAGAACCGCCAC CCTCAGAACTGAGACT
53	CCTCAAGAATACATGG CTTTTGATAGAACCAC
54	TAAGCGTCGAAGGATT AGGATTAGTACCGCCA
55	CACCAGAGTTCGGTCA TAGCCCCCGCCAGCAA
56	TCGGCATTCCGCCGCC AGCATTGACGTTCCAG
57	AATCACCAAATAGAAA ATTCATATATAACGGA
58	TCACAATCGTAGCACC ATTACCATCGTTTTCA
59	ATACCCAAGATAACCC ACAAGAATAAACGATT
60	ATCAGAGAAAGAACTG GCATGATTTTATTTTG
61	TTTTGTTTAAGCCTTA AATCAAGAATCGAGAA
62	AGGTTTTGAACGTCAA AAATGAAAGCGCTAAT
63	CAAGCAAGACGCGCCT GTTTATCAAGAATCGC
64	AATGCAGACCGTTTTT ATTTTCATCTTGCGGG
65	CATATTTAGAAATACC GACCGTGTTACCTTTT
66	AATGGTTTACAACGCC AACATGTAGTTCAGCT
67	TAACCTCCATATGTGA GTGAATAAACAAAATC
68	AAATCAATGGCTTAGG TTGGGTTACTAAATTT
69	GCGCAGAGATATCAAA ATTATTTGACATTATC
70	AACCTACCGCGAATTA TTCATTTCCAGTACAT
71	ATTTTGCGTCTTTAGG AGCACTAAGCAACAGT
72	CTAAAATAGAACAAAG AAACCACCAGGGTTAG
73	GCCACGCTATACGTGG CACAGACAACGCTCAT
74	GCGTAAGAGAGAGCCA GCAGCAAAAAGGTTAT
75	GGAAATACCTACATTT TGACGCTCACCTGAAA
76	TATCACCGTACTCAGG AGGTTTAGCGGGGTTT
77	TGCTCAGTCAGTCTCT GAATTTACCAGGAGGT
78	GGAAAGCGACCAGGCG GATAAGTGAATAGGTG
79	TGAGGCAGGCGTCAGA CTGTAGCGTAGCAAGG
80	TGCCTTTAGTCAGACG ATTGGCCTGCCAGAAT
81	CCGGAAACACACCACG GAATAAGTAAGACTCC
82	ACGCAAAGGTCACCAA TGAAACCAATCAAGTT

Table 4.1 (Continued)

83	TTATTACGGTCAGAGG GTAATTGAATAGCAGC
84	TGAACAAACAGTATGT TAGCAAACTAAAAGAA
85	CTTTACAGTTAGCGAA CCTCCCGACGTAGGAA
86	GAGGCGTTAGAGAATA ACATAAAAGAACACCC
87	TCATTACCCGACAATA AACAACATATTTAGGC
88	CCAGACGAGCGCCCAA TAGCAAGCAAGAACGC
89	AGAGGCATAATTTCAT CTTCTGACTATAACTA
90	TTTTAGTTTTTCGAGC CAGTAATAAATTCTGT
91	TATGTAAACCTTTTTT AATGGAAAAATTACCT
92	TTGAATTATGCTGATG CAAATCCACAAATATA
93	GAGCAAAAACTTCTGA ATAATGGAAGAAGGAG
94	TGGATTATGAAGATGA TGAAACAAAATTTCAT
95	CGGAATTATTGAAAGG AATTGAGGTGAAAAAT
96	ATCAACAGTCATCATA TTCCTGATTGATTGTT
97	CTAAAGCAAGATAGAA CCCTTCTGAATCGTCT
98	GCCAACAGTCACCTTG CTGAACCTGTTGGCAA
99	GAAATGGATTATTTAC ATTGGCAGACATTCTG
100	TTTT TATAAGTA TAGCCCGGCCGTCGAG
101	AGGGTTGA TTTT ATAAATCC TCATTAAATGATATTC
102	ACAAACAATTTTAATCAGTAGCGACAGATCGATAGC
103	AGCACCGTTTTTTAAAGGTGCAACATAGTAGAAAA
104	TACATACATTTTGACGGGAGAATTAACTACAGGGAA
105	GCGCATTA TTTT GCTTATCC GGTATTCTAAATCAGA
106	TATAGAAGTTTTCGACAAAAGGTAAAGTAGAGAATA
107	TAAAGTACTTTTCGCGAGAA AACTTTTTATCGCAAG
108	ACAAAGAA TTTT ATTAATTA CATTTAACACATCAAG
109	AAAACAAA TTTT TTCATCAA TATAATCCTATCAGAT
110	GATGGCAA TTTT AATCAATA TCTGGTCACAAATATC
111	AAACCCTCTTTTACCAGTAA TAAAAGGGATTCACCA GTCACACG TTTT
112	CCGAAATCCGAAAATC CTGTTTGAAGCCGGAA
113	CCAGCAGGGGCAAAAT CCCTTATAAAGCCGGC
114	GCATAAAGTTCCACAC AACATACGAAGCGCCA
115	GCTCACAATGTAAAGC CTGGGGTGGGTTTGCC
116	TTCGCCATTGCCGGAA ACCAGGCATTAAATCA
117	GCTTCTGGTCAGGCTG CGCAACTGTGTTATCC

Table 4.1 (Continued)

118	GTTAAAATTTTAACCA ATAGGAACCCGGCACC
119	AGACAGTCATTCAAAA GGGTGAGAAGCTATAT
120	AGGTAAAGAAATCACC ATCAATATAATATTTT
121	TTTCATTTGGTCAATA ACCTGTTTATATCGCG
122	TCGCAAATGGGGCGCG AGCTGAAATAATGTGT
123	TTTTAATTGCCCGAAA GACTTCAAAACACTAT
124	AAGAGGAACGAGCTTC AAAGCGAAGATACATT
125	GGAATTACTCGTTTAC CAGACGACAAAAGATT
126	GAATAAGGACGTAACA AAGCTGCTCTAAAACA
127	CCAAATCACTTGCCCT GACGAGAACGCCAAAA
128	CTCATCTTGAGGCAAA AGAATACAGTGAATTT
129	AAACGAAATGACCCCC AGCGATTATTCATTAC
130	CTTAAACATCAGCTTG CTTTCGAGCGTAACAC
131	TCGGTTTAGCTTGATA CCGATAGTCCAACCTA
132	TGAGTTTCGTCACCAG TACAAACTTAATTGTA
133	CCCCGATTTAGAGCTT GACGGGGAAATCAAAA
134	GAATAGCCGCAAGCGG TCCACGCTCCTAATGA
135	GAGTTGCACGAGATAG GGTTGAGTAAGGGAGC
136	GTGAGCTAGTTTCCTG TGTGAAATTTGGGAAG
137	TCATAGCTACTCACAT TAATTGCGCCCTGAGA
138	GGCGATCGCACTCCAG CCAGCTTTGCCATCAA
139	GAAGATCGGTGCGGGC CTCTTCGCAATCATGG
140	AAATAATTTTAAATTG TAAACGTTGATATTCA
141	GCAAATATCGCGTCTG GCCTTCCTGGCCTCAG
142	ACCGTTCTAAATGCAA TGCCTGAGAGGTGGCA
143	TATATTTTAGCTGATA AATTAATGTTGTATAA
144	TCAATTCTTTTAGTTT GACCATTACCAGACCG
145	CGAGTAGAACTAATAG TAGTAGCAAACCCTCA
146	GAAGCAAAAAAGCGGA TTGCATCAGATAAAAA
147	TCAGAAGCCTCCAACA GGTCAGGATCTGCGAA
148	CCAAAATATAATGCAG ATACATAAACACCAGA
149	CATTCAACGCGAGAGG CTTTTGCATATTATAG
150	ACGAGTAGTGACAAGA ACCGGATATACCAAGC
151	AGTAATCTTAAATTGG GCTTGAGAGAATACCA
152	GCGAAACATGCCACTA CGAAGGCATGCGCCGA

Table 4.1 (Continued)

153	ATACGTAAAAGTACAA CGGAGATTTCATCAAG
154	CAATGACACTCCAAAA GGAGCCTTACAACGCC
155	AAAAAAGGACAACCAT CGCCCACGCGGGTAAA
156	TGTAGCATTCCACAGA CAGCCCTCATCTCCAA
157	GTAAAGCACTAAATCG GAACCCTAGTTGTTCC
158	AGTTTGGAGCCCTTCA CCGCCTGGTTGCGCTC
159	AGCTGATTACAAGAGT CCACTATTGAGGTGCC
160	ACTGCCCGCCGAGCTC GAATTCGTTATTACGC
161	CCCGGGTACTTTCCAG TCGGGAAACGGGCAAC
162	CAGCTGGCGGACGACG ACAGTATCGTAGCCAG
163	GTTTGAGGGAAAGGGG GATGTGCTAGAGGATC
164	CTTTCATCCCCAAAAA CAGGAAGACCGGAGAG
165	AGAAAAGCAACATTAA ATGTGAGCATCTGCCA
166	GGTAGCTAGGATAAAA ATTTTTAGTTAACATC
167	CAACGCAATTTTTGAG AGATCTACTGATAATC
168	CAATAAATACAGTTGA TTCCCAATTTAGAGAG
169	TCCATATACATACAGG CAAGGCAACTTTATTT
170	TACCTTTAAGGTCTTT ACCCTGACAAAGAAGT
171	CAAAAATCATTGCTCC TTTTGATAAGTTTCAT
172	TTTGCCAGATCAGTTG AGATTTAGTGGTTTAA
173	AAAGATTCAGGGGGTA ATAGTAAACCATAAAT
174	TTTCAACTATAGGCTG GCTGACCTTGTATCAT
175	CCAGGCGCTTAATCAT TGTGAATTACAGGTAG
176	CGCCTGATGGAAGTTT CCATTAAACATAACCG
177	TTTCATGAAAATTGTG TCGAAATCTGTACAGA
178	ATATATTCTTTTTTCA CGTTGAAAATAGTTAG
179	AATAATAAGGTCGCTG AGGCTTGCAAAGACTT
180	CGTAACGATCTAAAGT TTTGTCGTGAATTGCG
181	ACCCAAATCAAGTTTT TTGGGGTCAAAGAACG
182	TGGACTCCCTTTTCAC CAGTGAGACCTGTCGT
183	TGGTTTTTAACGTCAA AGGGCGAAGAACCATC
184	GCCAGCTGCCTGCAGG TCGACTCTGCAAGGCG
185	CTTGCATGCATTAATG AATCGGCCCGCCAGGG
186	ATTAAGTTCGCATCGT AACCGTGCGAGTAACA
187	TAGATGGGGGGTAACG CCAGGGTTGTGCCAAG

Table 4.1 (Continued)

188	ACCCGTCGTCATATGT ACCCCGGTAAAGGCTA
189	CATGTCAAGATTCTCC GTGGGAACCGTTGGTG
190	TCAGGTCACTTTTGCG GGAGAAGCAGAATTAG
191	CTGTAATATTGCCTGA GAGTCTGGAAAACTAG
192	CAAAATTAAAGTACGG TGTCTGGAAGAGGTCA
193	TGCAACTAAGCAATAA AGCCTCAGTTATGACC
194	TTTTTGCGCAGAAAAC GAGAATGAATGTTTAG
195	AAACAGTTGATGGCTT AGAGCTTATTTAAATA
196	ACTGGATAACGGAACA ACATTATTACCTTATG
197	ACGAACTAGCGTCCAA TACTGCGGAATGCTTT
198	CGATTTTAGAGGACAG ATGAACGGCGCGACCT
199	CTTTGAAAAGAACTGG CTCATTATTTAATAAA
200	GCTCCATGAGAGGCTT TGAGGACTAGGGAGTT
201	ACGGCTACTTACTTAG CCGGAACGCTGACCAA
202	AAAGGCCGAAAGGAAC AACTAAAGCTTTCCAG
203	GAGAATAGCTTTTGCG GGATCGTCGGGTAGCA
204	ACGTTAGTAAATGAAT TTTCTGTAAGCGGAGT
205	TTTT CGATGGCC CACTACGTAAACCGTC
206	TATCAGGGTTTTCGGTTTGC GTATTGGGAACGCGCG
207	GGGAGAGGTTTTTGTAAAACGACGGCCATTCCCAGT
208	CACGACGT TTTT GTAATGGG ATAGGTCAAAACGGCG
209	GATTGACC TTTT GATGAACG GTAATCGTAGCAAACA
210	AGAGAATC TTTT GGTTGTAC CAAAAACAAGCATAAA
211	GCTAAATC TTTT CTGTAGCT CAACATGTATTGCTGA
212	ATATAATG TTTT CATTGAAT CCCCCTCAAATCGTCA
213	TAAATATT TTTT GGAAGAAA AATCTACGACCAGTCA
214	GGACGTTGTTTTTCATAAGGGAACCGAAAGGCGCAG
215	ACGGTCAATTTTGACAGCATCGGAACGAACCCTCAG
216	CAGCGAAAATTTTACTTTCAACAGTTTCTGGGATTTTGCTAAA C TTTT
Loop1	AACATCACTTGCCTGAGTAGAAGAACT
Loop2	TGTAGCAATACTTCTTTGATTAGTAAT
Loop3	AGTCTGTCCATCACGCAAATTAACCGT
Loop4	ATAATCAGTGAGGCCACCGAGTAAAAG
Loop5	ACGCCAGAATCCTGAGAAGTGTTTTT
Loop6	TTAAAGGGATTTTAGACAGGAACGGT

Table 4.1 (Continued)

Loop7	AGAGCGGGAGCTAAACAGGAGGCCGA
Loop8	TATAACGTGCTTTCCTCGTTAGAATC
Loop9	GTACTATGGTTGCTTTGACGAGCACG
Loop10	GCGCTTAATGCGCCGCTACAGGGCGC

Modified Strands (Morse Code).

Table 4.2 Thiol modified staple strands / Morse Code:

Sequence Name	Sequence (5'-3')
HS-16	GCTCATTTTCGCATTA AATTTTTG AGCTTAGA
HS-32	GTTTGCCACCTCAGAG CCGCCACCGATACAGG
HS-38	TATTTTGCTCCCAATC CAAATAAGTGAGTTAA
HS-44	CTGTAAATCATAGGTC TGAGAGACGATAAATA
HS-56	TCGGCATTCCGCCGCC AGCATTGACGTTCCAG
HS-62	AGGTTTTGAACGTCAA AAATGAAAGCGCTAAT
HS-68	AAATCAATGGCTTAGG TTGGGTTACTAAATTT
HS-128	CTCATCTTGAGGCAAA AGAATACAGTGAATTT
HS-194	TTTTTGCGCAGAAAAC GAGAATGAATGTTTAG

Table 4.3 Biotin modified staple strands / Morse Code:

Sequence Name	Sequence (5'-3')
Bio-50	GAATGGCTAGTATTAA CACCGCCTCAACTAAT
Bio-74	GCGTAAGAGAGAGCCA GCAGCAAAAAGGTTAT
Bio-112	CCGAAATCCGAAAATC CTGTTTGAAGCCGGAA
Bio-123	TTTTAATTGCCCGAAA GACTTCAAAACACTAT
Bio-134	GAATAGCCGCAAGCGG TCCACGCTCCTAATGA
Bio-140	AAATAATTTTAAATTG TAAACGTTGATATTCA
Bio-146	GAAGCAAAAAAGCGGA TTGCATCAGATAAAAA
Bio-152	GCGAAACATGCCACTA CGAAGGCATGCGCCGA
Bio-182	TGGACTCCCTTTTCAC CAGTGAGACCTGTCGT
Bio-188	ACCCGTCGTCATATGT ACCCCGGTAAAGGCTA
Bio-200	GCTCCATGAGAGGCTT TGAGGACTAGGGAGTT
Bio-206	TATCAGGG TTTT CGGTTTGC GTATTGGGAACGCGCG
Bio-209	GATTGACC TTTT GATGAACG GTAATCGTAGCAAACA
Bio-212	ATATAATG TTTT CATTGAAT CCCCCTCAAATCGTCA
Bio-215	ACGGTCAA TTTT GACAGCAT CGGAACGAACCCTCAG

DNA Sequences (Uppercase I / Lowercase i)

Table 4.4 Biotin modified staple strands / (I/i) :

Sequence Name	Sequence (5'-3')
Bio-14	CTAATTTATCTTTCCT TATCATTCATCCTGAA
Bio-37	ATTATTTAACCCAGCT ACAATTTTCAAGAACG
Bio-40	TAAGTCCTACCAAGTA CCGCACTCTTAGTTGC
Bio-59	ATACCCAAGATAACCC ACAAGAATAAACGATT
Bio-61	TTTTGTTTAAGCCTTA AATCAAGAATCGAGAA
Bio-124	AAGAGGAACGAGCTTC AAAGCGAAGATACATT
Bio-144	TCAATTCTTTTAGTTT GACCATTACCAGACCG

Table 4.5 Thiol modified staple strands / (I/i):

Sequence Name	Sequence (5'-3')
HS-11	CCTAATTTACGCTAAC GAGCGTCTAATCAATA
HS-57	AATCACCAAATAGAAA ATTCATATATAACGGA
HS-63	CAAGCAAGACGCGCCT GTTTATCAAGAATCGC
HS-65	CATATTTAGAAATACC GACCGTGTTACCTTTT
HS-121	TTTCATTTGGTCAATA ACCTGTTTATATCGCG
HS-147	TCAGAAGCCTCCAACA GGTCAGGATCTGCGAA
HS-164	CTTTCATCCCCAAAAA CAGGAAGACCGGAGAG
HS-166	GGTAGCTAGGATAAAA ATTTTTAGTTAACATC
HS-168	CAATAAATACAGTTGA TTCCCAATTTAGAGAG
HS-170	TACCTTTAAGGTCTTT ACCCTGACAAAGAAGT
HS-172	TTTGCCAGATCAGTTG AGATTTAGTGGTTTAA

Desthiobiotin modification of thiol-DNA. The concentration of DNA was calculated based on absorption at 280 nm according to the Beer-Lambert law. and adjusted to 100 µM. A 10 µM solution of 5` thiol modified DNA (used as received from IDT) was incubated with 2 µL of tributylphosphine solution for 2 hours at room temperature to the reduce the disulfide bond. Next, a 35 mM solution of desthiobiotin polyethyleneoxide iodoacetamide was freshly prepared in a 1 x TAE-Mg2+ buffer (Tris, 40 mM; acetic acid, 20 mM; EDTA, 2 mM; and magnesium acetate, 12.5 mM; pH 8.0) and incubated for 5 hours at 50 °C. Excess linkers were removed by washing 10 times with water using a 30 MWCO Amicon centrifugal filter. To purify the desthiobiotin functionalized product, the washed and concentrated solution was incubated with avidin agarose beads and eluted following manufacturers suggested protocols.

Non-denaturing PAGE. Gels containing 4% polyacrylamide (19:1 acrylamide/ bisacrylamide) were run on an Owl Adj2 electrophoresis unit at 4 °C (4 W, constant

wattage). The running buffer was 1x TAE-Mg^{2+} buffer. After electrophoresis, the gels were stained with ethidium bromide (Sigma) and imaged under UV illumination. DNA recovery was done by cutting and soaking gel pieces with 1x TAE-Mg^{2+} buffer for 12 hours at 4 °C.

Design and assembly of DNA origami. Rectangular origami tiles were formed according to Rothemund's paper with a ratio of 1:20 between viral DNA and both modified and unmodified staple strands. A concentration of 10 nM viral DNA was used in this work. Helper strands were mixed to form a master mix (50 μM) that was added to the viral DNA sequence in 1x TAE-Mg^{2+} buffer and annealed from 90 °C to 20 °C over 3 hours. After assembly of the origami tiles, they were washed 3x with 1x TAE-Mg^{2+} and concentrated using Amicon centrifugal filter units (100 MWCO, 300 x g speed, 10 min).

Conjugation of proteins to DNA origami template. To demonstrate selective release of protein from origami template, the protein decorated tiles were diluted to 1 mL and dialyzed overnight in a 300,000 MWCO membrane to remove the large excess of streptavidin that was necessary to prevent aggregation in the previous incubation step. The sample is then treated with 3 mM of biotin solution in 1x TAE-Mg^{2+} for 2 hours at room temperature before dialyzed with 1 mM biotin for 24 hours at 4 °C. The final solution is washed several times with 1x TAE-Mg^{2+} to remove excess biotin and concentrated to 30 μL using a 100,000 MWCO membrane.

AFM imaging. A drop of 3 ul DNA solution was spotted onto freshly cleaved mica surface, and kept for 10 s to achieve strong adsorption. 30 μL of 1x TAE-Mg^{2+} was added to the mica surface and the tip was pre-wet to prevent drift during imaging. Fluid

imaging was performed using nitride probes having a resonance frequency of 21-52 kHz (Olympus -TR400PSA). The tip–surface interaction was minimized by optimizing the scan set-point to the highest possible value. AFM imaging was performed at 22 °C. AFM data was processed with IGOR Pro software.

4.5 References

(1) Shih, W. M.; Quispe, J. D.; Joyce, G. F. *Nature* 2004, *427*, 618-621.

(2) Andersen, E. S.; Dong, M.; Nielsen, M. M.; Jahn, K.; Subramani, R.; Mamdouh, W.; Golas, M. M.; Sander, B.; Stark, H.; Oliveira, C. L. P.; Pedersen, J. S.; Birkedal, V.; Besenbacher, F.; Gothelf, K. V.; Kjems, J. *Nature* 2009, *459*, 73-U75.

(3) Douglas, S. M.; Marblestone, A. H.; Teerapittayanon, S.; Vazquez, A.; Church, G. M.; Shih, W. M. *Nucleic Acids Res.* 2009, *37*, 5001-5006.

(4) Douglas, S. M.; Dietz, H.; Liedl, T.; Hoegberg, B.; Graf, F.; Shih, W. M. *Nature* 2009, *459*, 414-418.

(5) Ke, Y. G.; Douglas, S. M.; Liu, M. H.; Sharma, J.; Cheng, A. C.; Leung, A.; Liu, Y.; Shih, W. M.; Yan, H. *J. Am. Chem. Soc.* 2009, *131*, 15903-15908.

(6) Ke, Y.; Voigt, N. V.; Gothelf, K. V.; Shih, W. M. *J. Am. Chem. Soc.* 2012, *134*, 1770-1774.

(7) Han, D.; Pal, S.; Liu, Y.; Yan, H. *Nat. Nanotechnol.* 2010, *5*, 712-717.

(8) Jean-Philippe J. Sobczak, T. G. M., Thomas Gerling, Hendrik Dietz *Science* 2012, *338*, 1458-1461.

(9) Wei, B.; Dai, M. J.; Yin, P. *Nature* 2012, *485*, 623-+.

(10) Sacca, B.; Niemeyer, C. M. *Chem. Soc. Rev.* 2011, *40*, 5910-5921.

(11) Seeman, N. C. *Nature* 2003, *421*, 427-431.

(12) Rothemund, P. W. K. *Nature* 2006, *440*, 297-302.

(13) Pinheiro, A. V.; Han, D. R.; Shih, W. M.; Yan, H. *Nat. Nanotechnol.* 2011, *6*, 763-772.

(14) Ding, B. Q.; Deng, Z. T.; Yan, H.; Cabrini, S.; Zuckermann, R. N.; Bokor, J. *J. Am. Chem. Soc.* 2010, *132*, 3248-+.

(15) Pal, S.; Deng, Z. T.; Ding, B. Q.; Yan, H.; Liu, Y. *Angew. Chem. Int. Edit.* 2010, *49*, 2700-2704.

(16) Acuna, G. P.; Bucher, M.; Stein, I. H.; Steinhauer, C.; Kuzyk, A.; Holzmeister, P.; Schreiber, R.; Moroz, A.; Stefani, F. D.; Liedl, T.; Simmel, F. C.; Tinnefeld, P. *ACS Nano* 2012, *6*, 3189-3195.

(17) Pal, S.; Varghese, R.; Deng, Z. T.; Zhao, Z.; Kumar, A.; Yan, H.; Liu, Y. *Angew. Chem. Int. Edit.* 2011, *50*, 4176-4179.

(18) Wang, R.; Nuckolls, C.; Wind, S. J. *Angew. Chem. Int. Edit.* 2012, *51*, 11325-7.

(19) Ko, S. H.; Gallatin, G. M.; Liddle, J. A. *Adv. Funct. Mater.* 2012, *22*, 1015-1023.

(20) Maune, H. T.; Han, S. P.; Barish, R. D.; Bockrath, M.; Goddard, W. A.; Rothemund, P. W. K.; Winfree, E. *Nat. Nanotechnol.* 2010, *5*, 61-66.

(21) Derr, N. D.; Goodman, B. S.; Jungmann, R.; Leschziner, A. E.; Shih, W. M.; Reck-Peterson, S. L. *Science* 2012, *338*, 662-665.

(22) Chhabra, R.; Sharma, J.; Ke, Y. G.; Liu, Y.; Rinker, S.; Lindsay, S.; Yan, H. *J. Am. Chem. Soc.* 2007, *129*, 10304-+.

(23) Kuzyk, A.; Laitinen, K. T.; Torma, P. *Nanotechnology* 2009, *20*.

(24) Wong, N. Y.; Zhang, C.; Tan, L. H.; Lu, Y. *Small* 2011, *7*, 1427-1430.

(25) Kim, D. N.; Kilchherr, F.; Dietz, H.; Bathe, M. *Nucleic Acids Res.* 2012, *40*, 2862-2868.

(26) Hung, A. M.; Micheel, C. M.; Bozano, L. D.; Osterbur, L. W.; Wallraff, G. M.; Cha, J. N. *Nat. Nanotechnol.* 2010, *5*, 121-126.

(27) Li, Z.; Liu, M. H.; Wang, L.; Nangreave, J.; Yan, H.; Liu, Y. *J. Am. Chem. Soc.* 2010, *132*, 13545-13552.

(28) Liu, W. Y.; Zhong, H.; Wang, R. S.; Seeman, N. C. *Angew. Chem. Int. Edit.* 2011, *50*, 264-267.

(29) Zhao, Z.; Liu, Y.; Yan, H. *Nano Lett.* 2011, *11*, 2997-3002.

(30) Han, D. R.; Pal, S.; Nangreave, J.; Deng, Z. T.; Liu, Y.; Yan, H. *Science* 2011, *332*, 342-346.

(31) Voigt, N. V.; Torring, T.; Rotaru, A.; Jacobsen, M. F.; Ravnsbaek, J. B.; Subramani, R.; Mamdouh, W.; Kjems, J.; Mokhir, A.; Besenbacher, F.; Gothelf, K. V. *Nat. Nanotechnol.* 2010, *5*, 200-203.

(32) Liu, J. W.; Wernette, D. P.; Lu, Y. *Angew. Chem. Int. Edit.* 2005, *44*, 7290-7293.

(33) Yoon, H. C.; Hong, M. Y.; Kim, H. S. *Langmuir* 2001, *17*, 1234-1239.

(34) Gu, H. Z.; Chao, J.; Xiao, S. J.; Seeman, N. C. *Nat. Nanotechnol.* 2009, *4*, 245-248.

(35) Lund, K.; Manzo, A. J.; Dabby, N.; Michelotti, N.; Johnson-Buck, A.; Nangreave, J.; Taylor, S.; Pei, R. J.; Stojanovic, M. N.; Walter, N. G.; Winfree, E.; Yan, H. *Nature* 2010, *465*, 206-210.

(36) Sherman, W. B.; Seeman, N. C. *Nano Lett.* 2004, *4*, 1203-1207.

(37) Gu, H. Z.; Chao, J.; Xiao, S. J.; Seeman, N. C. *Nature* 2010, *465*, 202-U86.

(38) Douglas, S. M.; Bachelet, I.; Church, G. M. *Science* 2012, *335*, 831-834.

(39) Finn, F. M.; Titus, G.; Hofmann, K. *Biochemistry* 1984, *23*, 2554-2558.

(40) Green, N.; Anfinsen, C.; Edsall, J.; Richards, F. *Advances in Protein Chemistry*; Academic Press: New York, 1975; Vol. 29.

4.6 Figures

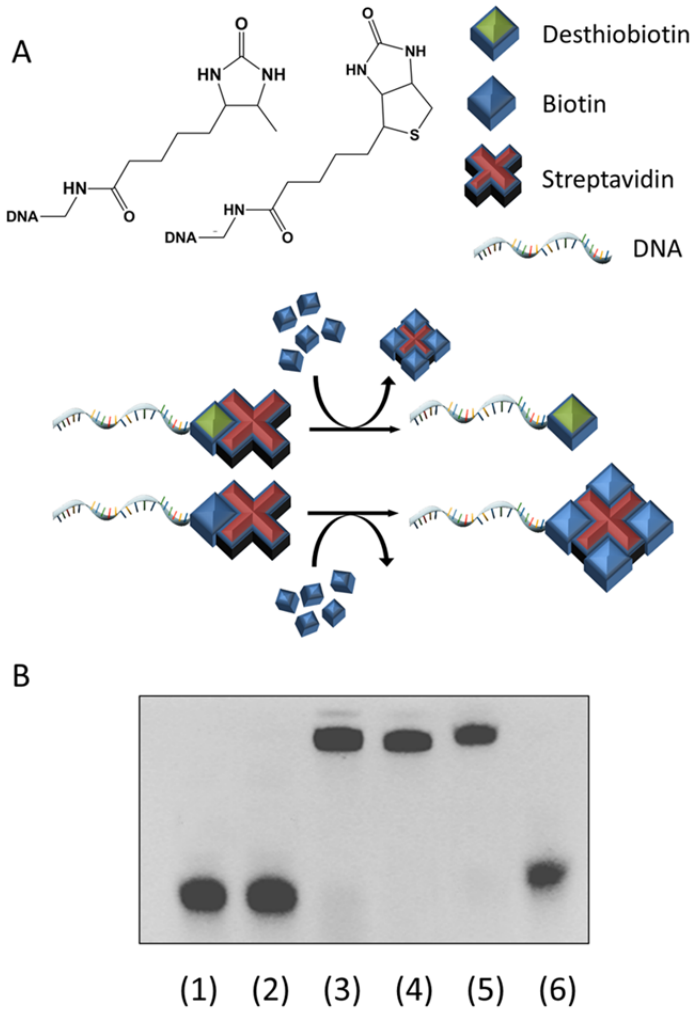

Figure 4.1 A) Chemical structures and schematic illustrations of the competitive binding between biotinylated and desthiobiotinylated DNA strands toward biotin; B) Native gel shift assay showing biotinylated and desthiobiotinylated DNA strands before (lanes 1,2 respectively), after incubation with streptavidin (lanes 3,4 respectively), and then after treatment with excess biotin (lanes 5,6 respectively).

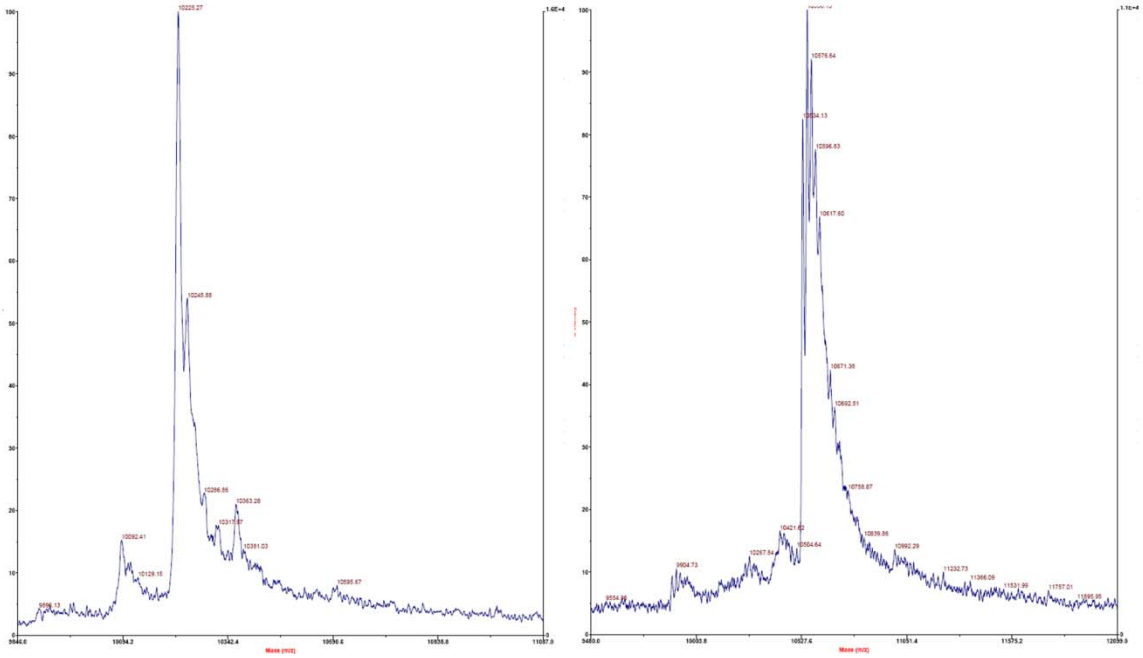

Figure 4.2 Matrix assisted laser desorption / ionization mass spectrometry (MALDI-MS) of unmodified, unpurified DNA strand with an observed mass of 10092 and10225 (left) and after modification with an observed mass of 10534-10756 (right), which corresponds well with the successful conjugation of the desthiobiotin linker, with an expected mass of 456.46 g / mol.

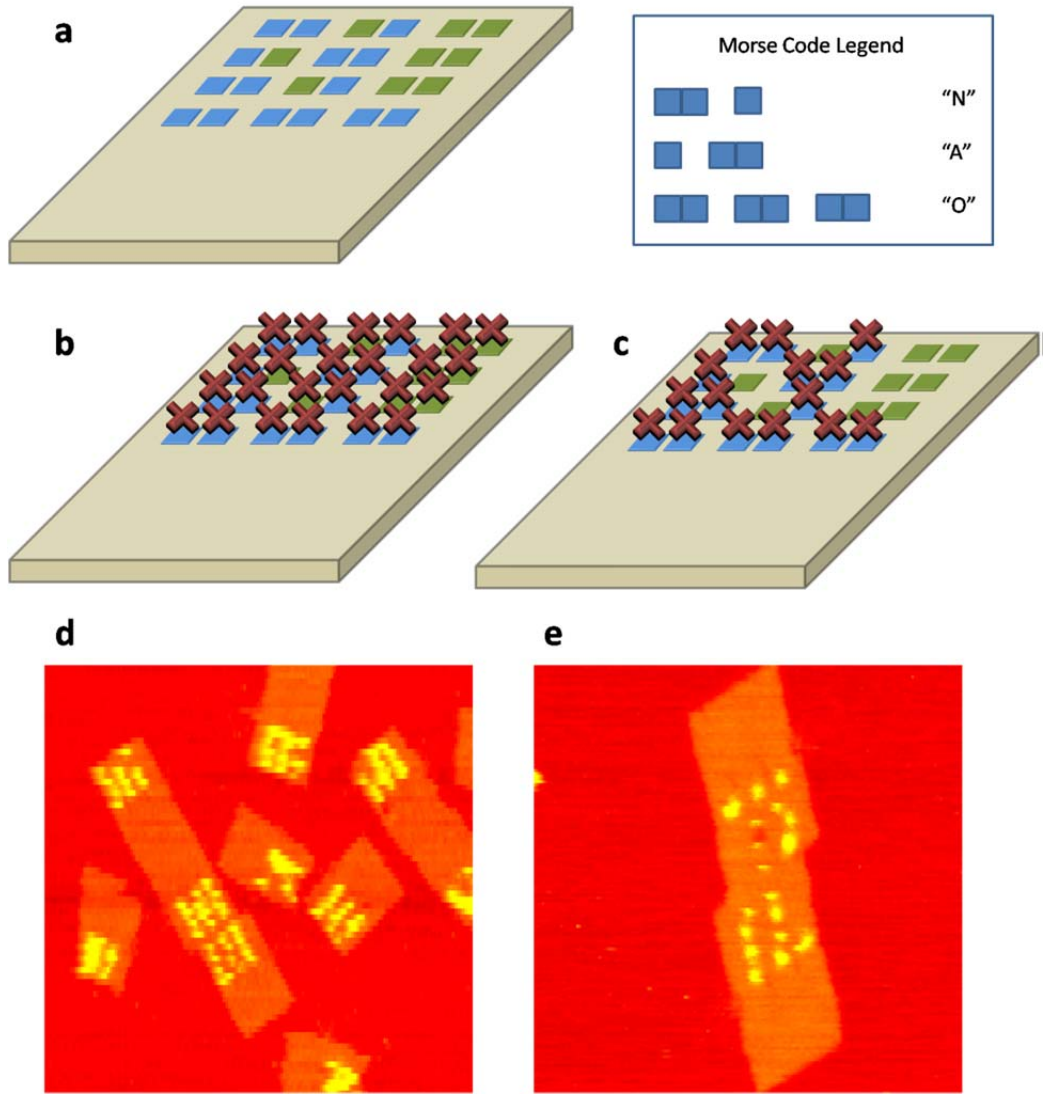

Figure 4.3 Initial design and characterization of the nano-morse code. To reduce the number of modifications necessary to form the code, only half of the DNA tile was used. The tile is a 100 nm x 70 nm rectangular tile made up for the mp13 bacteriophage DNA and 226 short stable strands (A-C). AFM characterization revealed that it was difficult to distinguish between a single protein and two adjacent proteins due to the small separations.

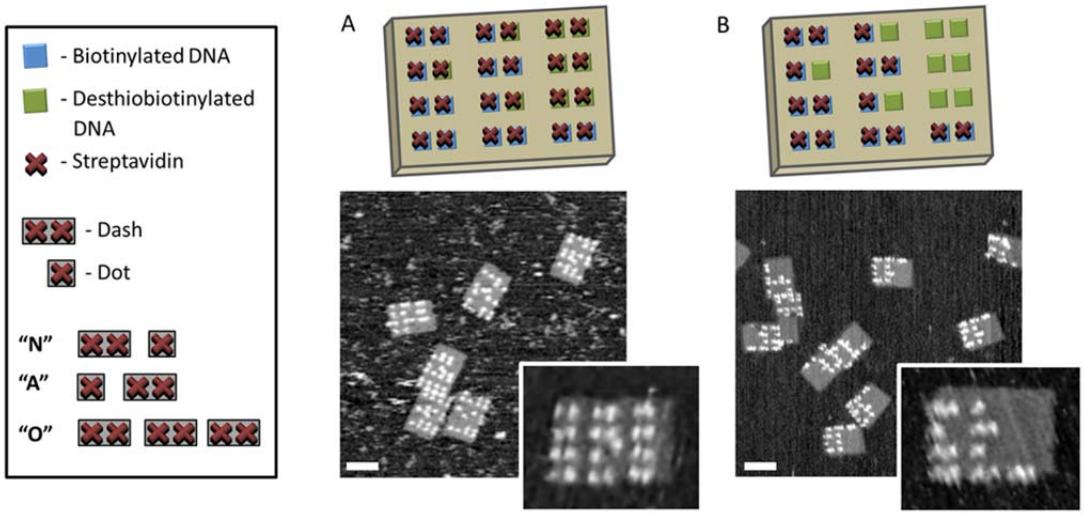

Figure 4.4 An illustration of the final design of encrypted and decrypted Morse code designs displaying the nonsense coded message "OOOO" and the hidden message "NANO" A) AFM images of tiles displaying encrypted message "OOOO" and (B) decrypted Morse code message "NANO" after biotin addition. Scale bar = 70 nm.

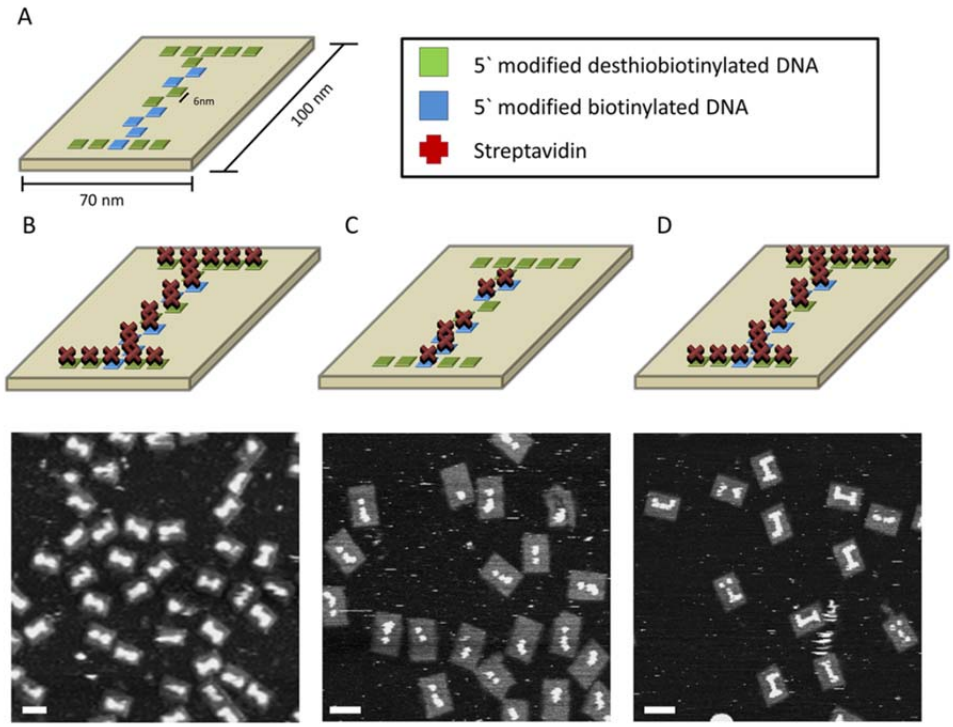

Figure 4.5 (A) Design of an uppercase “I” and lower case “i” as revealed by atomic force microscopy. (B) First incubation of functionalized tiles with streptavidin, revealing the capital “I” feature. (C) Subsequent incubation with excess biotin selectively removes streptavidin bound to desthiobiotin modifications, revealing the lower case “i.” (D) After washing, newly introduced streptavidin is allowed to bind to free desthiobiotin sites, recovering the capital “I” pattern on the DNA tile. Scale bar = 70 nm.

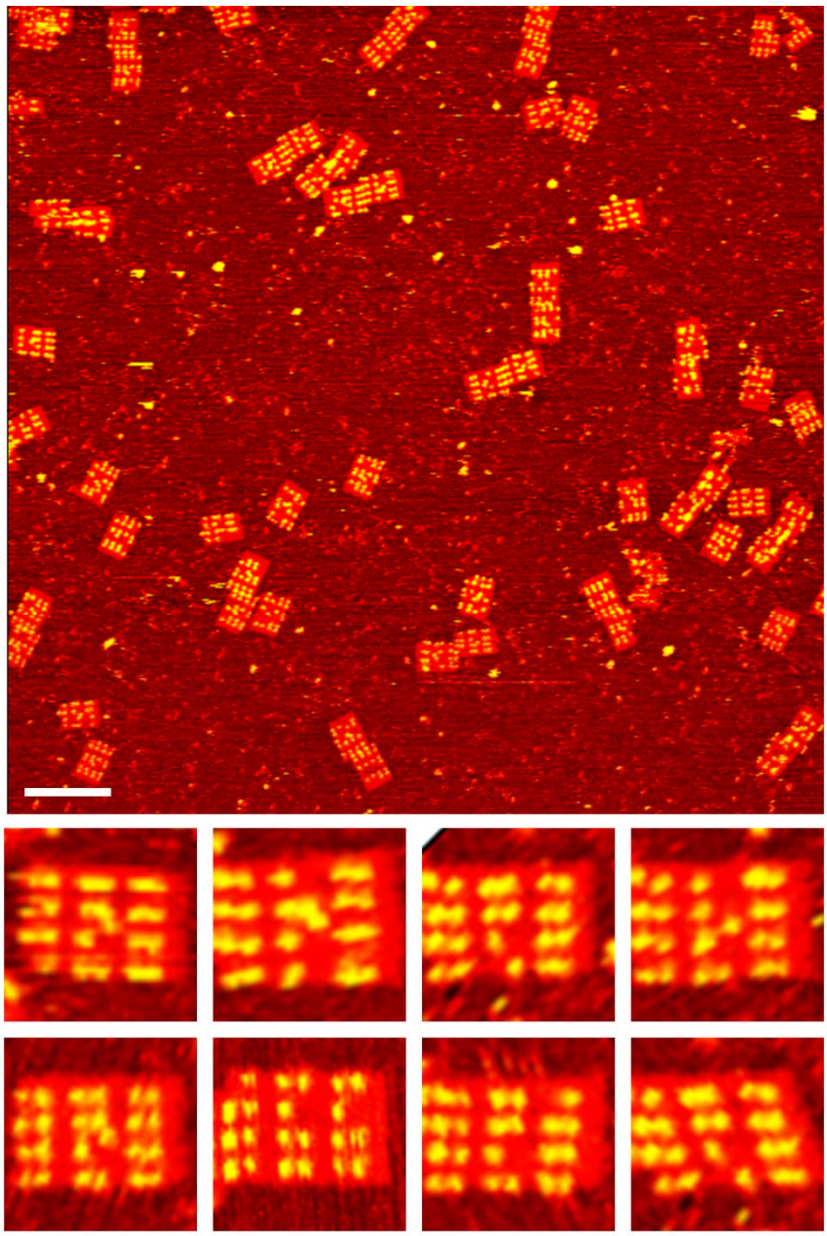

Figure 4.6 Large area atomic force microscope image of encoded nano-Morse code with zoomed in images of 8 well-formed tiles.

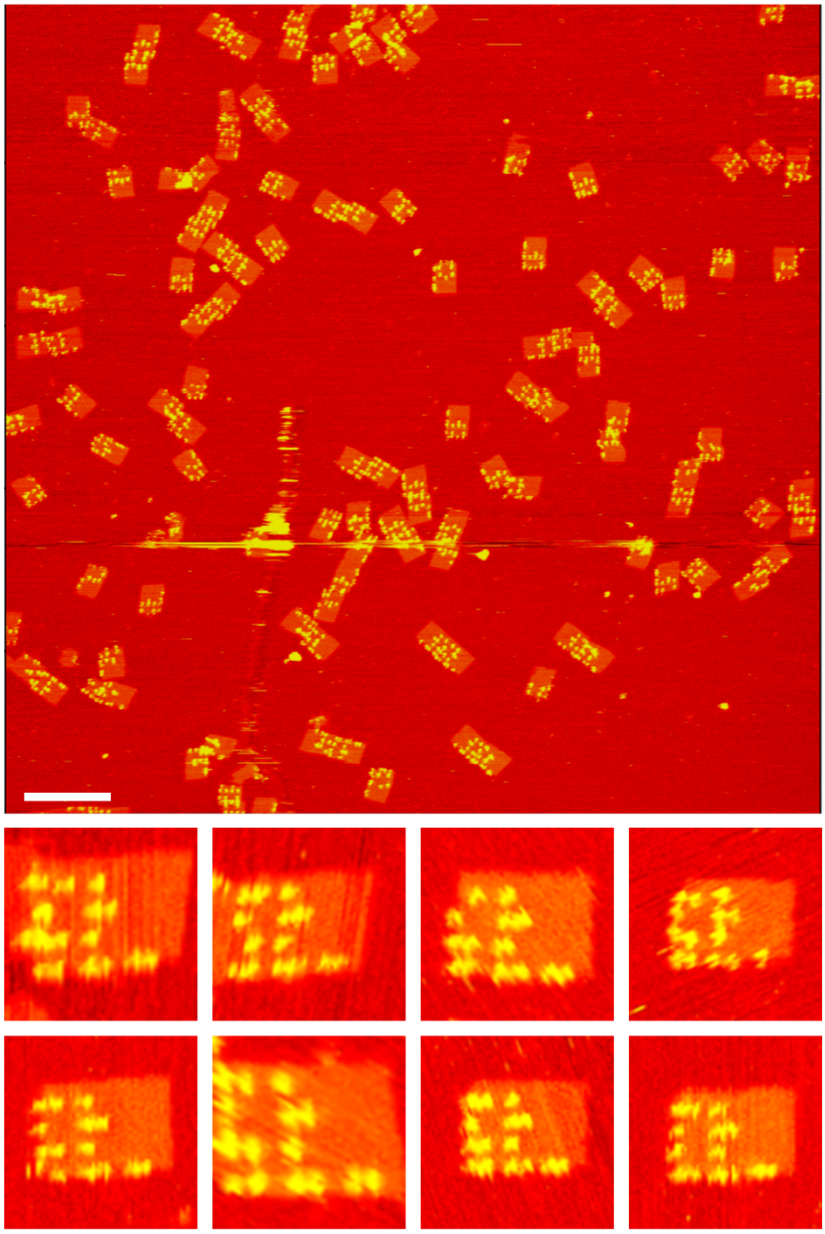

Figure 4.7 Large area atomic force microscope image of decoded nano-Morse code with zoomed in images of 8 well-formed tiles.

CHAPTER 5

FACILE, PHOTOSTABLE, AND MONODISPERSED DNA MEDIATED NANOFLOWERS AS OPTICAL CONTRAST IMAGING AGENT FOR DIRECTED UPTAKE AND IMAGING OF CANCER AND TUMOR CELLS

5.1 Introduction

The characterization of nano-bio interactions and successful application of nanosized materials for the next generation of biomedical therapies is poised to be one of the greatest developments in the 21st century. The goal of this research is to design and engineer a class of carriers that is capable of navigating the body, infecting and transforming cells, or detecting and repairing diseased cells. In order to realize these goals, we must develop an in depth understanding of nano-bio interactions and carry out standardized and complete characterization of nanomaterials across a wide range of materials, shape, size, and surface chemistry. Unfortunately, one of the major shortcomings of nano-bio research has been the proliferation of "proof-of-concept" demonstrations that have so far, been difficult to correlate in a complete, useful database. Fortunately, despite a lack of standardized experiments, some general nano-bio trends have been elucidated and validated.

For a majority of nano-bio platforms, a prototypical nanoparticle is first chemically synthesized, then the surface is modified with one or more polymer, drug, fluorophore, peptide, proteins, or oligonucleotide, and their uptake by cell cultures (*in vitro*) or various animal models (*in vivo*) are characterized and reported. Here we briefly

highlight some of the more important nano-bio concepts such as multivalency, size, shape, and surface charge, as factors within the overall parameter of "uptake efficiency."

The multivalency effect is the idea that the binding strength and uptake of a particle is enhanced if more than one ligand on a particle binds to multiple targeted receptors of a cell. This effect was observed by Jiang et al. (1) using antibody decorated nanoparticles and Walsh et al. (2) via aptamer decorated DNA tetrahedrons. Jiang and coworkers varied the density of Herceptin on a gold nanoparticle surface by varying the curvature of the particle. In their report, the binding affinity of Herceptin to the ErbB2 receptor is 10^{-10} M in solution, 5.5×10^{-12} M on a 10-nm nanoparticle, and 1.5×10^{-13} M on a 70-nm nanoparticle. Interestingly, they also reported that downstream signaling via the ErbB2 receptor was strongest with 40-50 nanometer particles, demonstrating additional effects must be considered beyond ligand density. Recently Walsh et al elegantly confirmed this finding through the use of DNA tetrahedrons (see chapter 3 of this theis). By controlling the number of ligands (DNA aptamers) at each vertex of the nanostructure, they were able to vary the orientation and the density of ligands and reported that a minimum of three ligands, oriented in the same direction, was necessary for maximum uptake. Interestingly, they also reported that additional ligands did not increase the uptake efficiency of the nanostructures.

It has long been recognized that particle size and shape were important factors in determining the final uptake efficiency. Gratton et al. demonstrated elegantly similar sized nanoparticles with different shapes significantly impact the uptake. In his work, Gratton and coworkers show that above 100 nanometers, nanorods demonstrate the highest uptake, followed by spheres, cylinders, and cubes. Interestingly, in studies with

sub-100-nm nanoparticles, spheres show an advantage over rods. (3,4) At size scales below 100 nanometers, it was reported that increasing the aspect ratio of nanorods will decrease total cell uptake. Although few studies have focused on nonspherical nanoparticles thus far, research indicates their interactions with cells may be much more complex. Ligand-coated rod-shaped nanoparticles may present to the cell with two different orientations. Compared with the short axis, the long axis will interact with many more cell surface receptors. (5) For spiky nanostructures such as gold nanourchins, whether the ligand is located on or between the spikes affects how it is presented to the target cell receptors (6). From these investigations, it can be concluded that non-spherical and asymmetric particles demonstrate more complex nano-bio interactions but also allows more control over engineering desired uptake properties. Above, it was noted that nanoparticles with at roughly 50 nanometers exhibited the most effective uptake properties. A possible explanation for this phenomenon arises from the formation of vesicles during receptor mediated endocytosis. When one or more targeting ligands bind to surface receptors, the nanoparticle causes a localized decrease in the Gibbs free energy which triggers wrapping of the membrane and the formation of vesicles by the cell. It can be calculated that nanoparticles at roughly 50 nanometers can bind enough receptors to successfully promote membrane wrapping. (7) At sizes above 50 nanometers, the nanoparticles may bind such a large number of receptors that total uptake is then limited by the redistribution of receptors on the cell surface to accommodate the binding of additional nanoparticles. Similarly, nanoparticles below 50 nanometers may not bind enough receptors to efficiently promote the wrapping of the membrane to form vesicles. Since most of the work in this field has demonstrated such proof of concept work using

immortalized cell lines, and each cell type possesses a unique phenotype with varying levels of target receptors and internalization pathways, it will become increasingly important to fully characterize the uptake with both immortalized as well as primary cells in different cell culture configurations. A standardized panel of cells and conditions would provide a roadmap toward creating a large, compatible library of information that will allow researchers to generate, test, and validate significant trends or mechanism.

As briefly mentioned above, gold nanoparticles have become one of the bedrocks of nano-biotechnology research. It processes excellent stability, biocompatibility, and a large library of available surface modifications that is often desired for in vitro and in vivo studies. A close analogy to the size and shape dependency of nanoparticle physiochemical properties, the uptake of nanoparticles by cells is highly dependent on the shape, size, and surface functionality/charge. Towards shape-controlled nanoparticle synthesis, molecular capping agents such as organic surfactants and polymers have been used to direct nanocyrstal growth in a face selective fashion. (8,9) Despite tremendous progresses made, the mechanism of the shape control is not well understood, in part due to the difficulty in defining structures and conformations of these surfactants and polymers in solution and in systematic variation of functional groups. DNA is a well-known biopolymer with more defined structure and conformation in solution and unique programmable nature to tune its functional properties. (10-13) Because of these advantages, DNA has been used as template to position nanoparticles through DNA metallization (14,15), or nanoparticle attachment (13,16-20), or to control the sizes, and the photo-luminescent property of quantum dots. (21-27) In a previous publication, Wang et al. (28) demonstrated the synthesis of a DNA template gold nanoflower that

highlighted the base dependent interaction between nucleotides, gold nanoparticle surface, and oligonucleotide driven reduction of gold ions onto a gold particle seed. In the experiment, Wang et al. demonstrated for the first time that DNA can be used to tune gold nanoparticle morphology in a sequence dependent manner, suggesting that biomolecules can play a significant role in shaping nanoparticles. Furthermore, DNA functionalization with high stability was realized in-situ during the one-step synthesis while retaining their bio-recognition ability. We have also shown that the DNA functionalized nanoflowers can be readily uptaken by cells and visualized under dark-field microscopy.

One of the major advantages of above mentioned gold nanoflowers is its high scattering profile when viewed under dark-field optical microscopy. Traditional cell labeling and imaging is done using a library of small molecule fluorophores and dyes. However, these dyes suffer from severe photobleaching effects where the dye is rapidly degraded under irradiation and their visualization often requires expensive light sources and specialized filters. By using a contrast agent that is biocompatible, does not require special illumination, and does not suffer from photo-degradation, the imaging and identification of specific cell types becomes more standardized and more widely available. The other major advantage of the current technique is the simplicity of the functionalization and the expected stability of the functionalization.

In the following work, we hypothesize that we are able to incorporate the newly discovered nanoflower structure with a cancer specific aptamer sequence (NCL / AS1411) that exhibit high affinity and specificity toward nucleolin, a protein known to be overexpressed on the surface of several cancer cell lines, such as MCF-7, an immortalized human breast cancer cell line. We are also interested in exploring the shape

and size dependent uptake of nanoflowers, especially compared to similarly sized nanoparticles. The goal is to develop a simple nanoparticle platform that is easy to produce via a one-step synthesis, with a highly stable aptamer functionalization, demonstrate improved uptake over spherical nanoparticles, and can be used for imaging, diagnosis, and therapy of cancer and other diseased cells.

5.2 Results and Discussion

Previous work by Storhoff (29) and Wang (30), have clearly demonstrated that the interaction between nucleic acid and oligonucleotides are sequence dependent with adenosine (A) and cytosine (C) showing high interaction and physical adsorbtion onto gold surfaces and tyrosine (T) showing a significantly lower interaction. Guanine (G) was not considered in the current work due to significant secondary structures when multiple, consecutive guanines are present within an oligonucleotide. (31) This was further demonstrated by Wang et al. when he showed that DNA induced formation of gold nanoflowers was observed only in the presence of a 30 adeonsine repeat (30-A) and a 30 cytosine repeat (30-C) oligonucleotide. It is noted that a 15-T and 15-A sequence did not produce a high quality nanoflower structure, indicating that the gold-nucleotide interaction is cumulative over the sequence and a minimum number of cytosine or adenosine is needed for strong adsorption. Taking these factors into consideration, two final oligo designs were tested. Since the AS1411 aptamer is a GC rich oligo and likely forms a secondary structure related to its specific binding to nucleolin, the interaction of the aptamer sequence with gold nanoparticles can be considered minimal. To confirm this, the aptamer sequence was incubated with 20 nm gold nanoparticles and upon addition of a reduc tant (NH_4OH) and gold source. UV-Vis and TEM confirm that the as-

grown nanoparticles remained spherical, a good indication that the interaction between the aptamer sequence and gold surface is negligible. Based on these observations, the first aptamer construct was a simple hybrid of a 30 repeat of cytosine or adenosine with the aptamer sequence. These sequences were named 30C-AS1411 and 30C-Control. However it is important to consider that during the nanoflower growth process, part of the oligonucleotide on the surface will become entrapped within the growing gold layer, possible disturbing the structure and functionality of the aptamer sequence. To compensate, a second construct incorporate a 15-T spacer between the gold binding region and the aptamer within the oligonucleotide sequence. These constructs were named 30C-15T-AS1411 and 30C-15T-Control. Lastly, in the event that the aptamer cannot be freed from the growing gold layer, a 5` end modified aptamer with a 5T spacer was tested as a post-synthesis functionalization. This sequence will be used also to functionalize spherical corresponding sizes of gold nanospheres to investigate a potential difference in size dependent uptake.

One of the most important parameters that affect cell uptake efficiency is nanoparticle size. Chithrani et al. showed that spherical gold nanoparticles 40-50 nm achieved optimal cellular uptake by HeLa cells. *(3)* In addition to size, it will become important to investigate many other factors such as material, shape, surface modifications, and cell types to elucidate their role in cellular uptake of DNA functionalized nanoflowers. To determine the best method to control size of gold nanoflowers, we designed two parallel experiments: seed based and growth based. Since the nanoflower growth process is one that is defined by 3 factors: gold seed size, gold seed concentration, and gold salt concentration. By first holding seed size constant (20

nm) and varying the gold salt ($AuCl_4$) concentration from 0.003% to 0.016% w/v, we were able to observe a linear increase in nanoflower size from ~35 to 50 nm diameter as determined by transmission electron micrographs. All values were calculated from averages diameters of 50 particles as measured from tip to tip as well as by dynamic light scattering (DLS). Transmission electron micrographs confirm similar trends using both oligonucleotide constructs, with both AS1411 as well as a randomized control sequence. Of note, nanoflower size homogeneity decreased with increasing nanoflower growth.

As mentioned, during the growth of the nanoflower, the growing gold layer engulfs a portion of the DNA strand. Therefore, to maximize the probability of the complete aptamer sequence remaining exposed post-synthesis, it is important to optimize the growth process to achieve the desired physical and optical properties while minimizing the gold growth needed. To achieve this, we successfully demonstrated the size control of nanoflowers by establishing the minimum growth condition for 10, 20, and 40 nm gold nanoparticle seeds as confirmed by dynamic light scattering, UV-Vis, and TEM. Of note, nanoflowers generated with 50 nm and larger seed particles did not form uniform nanoflowers and were unstable in water. This is likely because the physical adsorption of oligos was not sufficient in stabilizing the particle during the growth. The minimum growth condition is defined as the lowest $AuCl_4$ concentration that completely shifted the 520 nm absorption peak of a spherical gold nanoparticle into the characteristic absorption peak of the corresponding nanoflower. It was reported that the interaction between specific nucleotides and the gold surface can lead to the growth of sequence specific shapes, additionally, during this set of experiment we find that the size of the nanoflowers is limited by the length of the DNA strand. In particular, it was observed that

when poly-A(30) sequence was used, a 20 nm seed nanoflower cannot be growth with high yield and monodispersed at sizes less than 33 nm. On the other end of the spectrum, poly-A(30) cannot be used to grow stable nanoflowers above 50 nm, or the nanoflowers quickly aggregates and precipitates from the solution. However, when a much longer 71 base pair strand, such as the 30T-15C-APT or 30T-15C-CTRL sequence, is used to direct nanoflower growth, the size of the gold nanoflowers can be grown to greater than 200 nm while remaining stable in solution for greater than 6 months.

An important consideration for any nanoparticle system destined for in vitro and in vivo applications is the stability of the nanoparticles in biological or biologically relevant fluids. Previous work by Storhoff (29), Petrovykh (32), Wang (33), and others have demonstrated and studied the capacity of both chemically or physically bound layer of oligonucleotides to protect nanoparticles from aggregation and degradation in high salt, complex environments. In particular, Mirkin's group has developed a strategy for decorating nanoparticles with an extremely dense layer of DNA that demonstrates excellent thermal and biochemical stability. To better understand the stability of the aptamer functionalized nanoflowers, all design constructs were diluted and incubated in 1x OPTIMEM at 37 °C for 2 hours. The nanoparticles were then washed 3x in Millipore water by centrifugation and resuspended in Millipore water and analyzed by UV-Vis. As synthesized, both constructs (30C-AS1411 and 30C-15T-AS1411) showed signs of aggregation post incubation as demonstrated by a shift in UV-Vis absorption spectrum. Two strategies to increased nanoflower stability were tested, increasing the density of DNA on nanoflower surface, and post-synthesis PEGylation.

The density of oligo functionalization on a nanoparticle surface directly correlates

to the stability of the nanoparticle and its cellular uptake properties. (34,35) This was done by increasing the NaCl concentration from 0 mM to 200 mM over 24 hours during the DNA incubation with gold nanoparticle seed. By slowly increasing the concentration of NaCl in the incubation buffer, the highly negative oligonucleotides were increasingly screened from each other, theoretically allowing more oligos to be immobilized onto the surface. After the DNA incubation process, the nanoflowers synthesis proceeded as previously described. Increased stability of high density DNA nanoflowers were demonstrated by challenging as-synthesized nanoflowers and high density DNA nanoflowers to a 300 mM NaCl solution and incubated at room temperature for 1 hour. As seen from optical observation and UV-Vis characterization, after incubation in a 300 mM NaCl solution for 1 hour, the as-synthesized nanoflowers aggregated and settled to the bottom of the tube while the high density DNA nanoflowers retained the characteristic blue-ish color. UV-Vis and electron micrographs further confirm the stability of the high density DNA nanoflowers. However, when challenged with 1x OPTIMEM, the high density DNA nanoflowers also appears to aggregate after a 2 hour incubation at 37 °C.

A second technique, post synthesis PEG functionalization was also carried out. After nanoflower synthesis, the nanoflowers were washed 3x by centrifugation in DI water and resuspended in a conjugation buffer. SH-PEG (MW 1000) was added and kept for 2 hours before washing 5x in DI water. PEGylated and non-PEGylated DNA nanoflowers were then resuspended in OPTIMEM for 2 hours at 37 °C. UV-Vis data shows that the PEGylated nanoflowers did not experience a shift in its absorption peak, indicating good stability while the non-PEGylated nanoflowers showed peak shift and

broadening that is characteristic of nanoparticle aggregation. The addition of PEG post-synthesis significantly enhanced the stability of the nanoflowers in cell media and no aggregation was observed when the nanoflowers were suspended in Opti-Mem for 2 hours.

Finally, it is possible that the growth of the nanoflowers will partially or completely block the aptamer and reducing or eliminating its target recognition ability. Therefore, as a backup we also decorated pre-synthesized nanoflowers with thiolated aptamers. The nanoflowers were treated first with a polyA-30 oligonucleotide, grown into nanoflower shapes, and then finally decorated with aptamers. This technique guarantees the availability of the aptamers on the surface of the nanoflowers for target specific binding.

In addition to demonstrating the cell specific uptake of the nanoflowers by cancer cells, we were interested in the uptake characteristic of a nanoflower shaped particle versus the more traditional nanospheres that are widely used today. Chithrani et al. (*3*) reported in 2006 that *in vitro* uptake of nanospheres are size dependent, where 40 nanometer particles are most readily taken up by cells. Additionally, for *in vivo* applications, it has been reported and confirmed that nanoparticles from 40 nm to 200 nm exhibit the longest half-life in the blood stream due to their ability to avoid the liver. A similar study was also reported for the size dependent uptake of nanorods in cells. Therefore, we were interested in the size dependent uptake behavior of nanoflower shaped particles as well nanoflower uptake efficiency compared with spherical nanoparticles under similar conditions.

Targeted uptake *in vitro*. To understand the cellular uptake properties of the DNA

nanoflowers and whether it is able to achieve selective uptake through aptamer recognition, we choose to work with MCF-7 cells, a human breast cancer cell line, as a model cell system. This particular cell line overexpresses the nucleolin protein on the cell surface and which can be effectively targeted by the AS1411 aptamer. One of the main advantages of the nanoflower structure is its high scattering profile when viewed under dark field microscopy as first reported by Wang et al. Therefore, uptake experiments are characterized by bright and dark field microscopy and quantified using transmission electron microscopy and ion-coupled plasma mass spectroscopy (ICP-MS).

The nanoflowers synthesized by each of the three techniques described above were incubated with MCF-7 cells to determine their cellular uptake properties.

Following the original hypothesis, we prepared a series of nanoflowers grown using a single DNA strand which consists of three sub-segments: anchor (poly-C-30), spacer (poly-T-15), and the targeting aptamer (or control sequence). The 71 base pair sequence is incubated with a 20 nanometer gold particle seed for 20 minutes, and grown into ~ 35 nanometer gold nanoflower structures. As figure XX shows, below 30 nanometers, the size distribution of the nanoflowers increased dramatically and a percentage of the nanoparticles remained in spherical, rather than flower shaped. Therefore, given this minimum size restriction, the MCF-7 cell cultures were incubated with the nanoflowers for 2 hours. Under the optical microscope, it can be observed that there is a high background from non-specific binding of nanoparticle aggregates on the bottom of the plate. While there seems to be some increase in the aptamer functionalized nanoflowers to the MCF-7 cells, due to the significant background signal and aggregation, this system was not pursued further.

Next, as mentioned above, we reasoned that the stability of the nanoflowers could be increased by either increasing the density of the DNA on the surface of the nanoparticle, or by backfilling the nanoflower surface with polyethylene glycol. The first strategy is one that has been perfected by the Mirkin group at Northwestern. By slowly increasing the salt concentration while incubating gold nanoparticles with thiolated DNA, Dr. Mirkin has successfully demonstrated highly dense packing of DNA on gold nanoparticles which exhibit extraordinary stability and interestingly, a much sharper melting temperature than a normal double stranded DNA. Following this model, we hypothesized that by increasing the density of the DNA coverage on the surface of the particle, we would accomplish two goals simultaneously. The first was to increase the density of DNA coverage to increase the stability of the nanoflowers. The second was that increasing the density of the coverage meant that the spacer portion of the DNA (with lower DNA-gold binding affinity) would be crowded off the surface of the gold by the presence of more anchoring strands (with higher DNA-gold binding affinity), this in turn, would increase the distance between the targeting aptamer sequence to the growing gold surface, thus increasing the likelihood that the aptamer would be intact post-synthesis. The second strategy to improve the stability was by post-functionalization of the nanoflowers by conjugating a thiolated PEG to the surface. A short 1000 MW HS-PEG was used to minimize the chances of the PEG blocking the activity of the aptamer. Both nanoflowers in these experiments were grown from 20 nm gold particle seeds to roughly 35 nanometer gold nanoflowers.

Figure 5.3 shows the results of the uptake experiment with nanoflowers grown by increasing the salt concentration slowly from 0 mM to 75 mM while the nanoparticle

seeds were incubated with DNA. In this case, we observe a seemingly large difference between the aptamer and control samples with a decreased level of aggregates visible in the sample. However two things were of concern, first, we observe that there is significant non-specific binding in the aptamer functionalized samples and the second is that the brightness levels were disproportionate with the number of visible uptaken particles. This was later confirmed as an imaging irregularity. Repeated experiments show the presence of non-specific binding and this strategy was no longer pursued.

Next, Figure 5.4 shows the results of the uptake experiments with nanoflowers post-functionalized with polyethylene glycol to increase the stability of the nanoflowers. We observe under bright and dark field imaging that indeed both the aptamer functionalized and control nanoflowers had significantly reduced background, non-specific binding as well as complete absence of aggregation as seem in previous samples. Unfortunately, there was no obvious difference in the uptake of the aptamer functionalized nanoflowers versus the nanoflower with control sequences. At this point, it was assumed that the growth of the nanoflower with a single strand strategy, while ideally more simple, was not a feasible strategy. Finally, as a positive control experiment, MCF-7 cell cultures were incubated with PEG protected, control sequence nanoflowers for 24 hours. Figure 5.2 shows properly uptaken nanoflowers in darkfield scattering mode, with little aggregation and non-specific binding visible in either darkfield or bright field microscopy.

The last strategy was a post-synthesis with thiolated aptamer and control sequence. While this strategy does not offer the advantage of increased stability of the aptamer by virtue of a physical incorporation of the sequence into the nanoflower

structure, it does offer better control of the nanoflower growth (with a simple, poly-A strand), guaranteed availability of the aptamer, and a path to study shape and size dependent uptake of nanoflowers with multiple cell types. The experiment following consisted of comparing nanoflowers and nanoparticles of 4 different sizes, 20 nm, 40 nm, 60 nm, and 80 nm, decorated with either the AS1411 aptamer sequence or control sequence.

Before describing the growth the various sizes of nanoflowers, there was an effort to reduce the dispersity of the synthesized nanoflowers. In the previous described procedure by Wang et al. the synthesis process involved adding a small volume (~1 μL) of a high concentration of gold salt (1% w/v) into a relative small volume of gold nanoparticles (~300 μL). This was suitable for the particular system that was described by Wang et al., however, when the same procedure was used to synthesize a board range of sizes of nanoflowers, the poly-dispersity of the product was quite high, as confirmed by both DLS and TEM imaging. To address these issues, the hypothesis was that the polydispersity was caused by the very quick reaction that was taking place to grow the nanoflowers. By increasing the overall volume of the system, reducing the concentration of gold nanoparticles, reducing the concentration of reduction agent, and reducing the stock concentration of gold stock, would slow the reaction down enough to achieve uniform mixing before significant growth of the nanoflowers occurred. After optimization, a general procedure for highly monodispersed nanoflowers across a large size spectrum was established. Briefly, a 100 μL stock solution of gold nanoparticles was diluted in 500 uL of Millipore water and incubated with 3 μM of DNA for at least 20 minutes at room temperature. Next, 500 μL of Millipore water was added to a NaOH

treated glass vial and 30 uL of 400 mM hydroxylamine hydrochloride were added. Next, the gold nanoparticle solution was added to the glass vials. While under vortex (setting between 7 and 8), a variable volume of 0.01% w/v gold salt solution was added quickly and the solution was vortex vigorously for 15 minutes to allow the complete reduction of gold salt onto gold nanoparticle seeds.

To synthesize 20 nanometer gold nanoflowers, we start with a 10 nm seed; incubate with a 3 μM poly-A30 DNA sequence and varied the gold salt from 100 μL to 400 μL. The resulting nanoflowers followed a linear trend from 18 nm to 28 nm, with 300 μL corresponding to a 20 nm nanoflower. Synthesized nanoflowers were characterized by UV-Vis, DLS, and TEM imaging. It is of note that nanoflowers using seeds below 10 nm does not lead to smaller nanoflower structures, rather small amounts of nonspecific aggregation occurs and links the small nanoparticle seeds into amorphous structures. The 20 nm gold nanoflowers also exhibited a slightly different structure then its larger counter parts, namely each nanoflower shows only 2-3 ‘spikes’ rather then

To synthesize 40 nanometer gold nanoflowers, we start with a 20 nm seed; incubate with a 3 μM poly-A30 DNA sequence and varied the gold salt from 100 μL to 400 μL. The resulting nanoflowers followed a linear trend from 35 nm to 45 nm, with 400 μL corresponding to a 40 nm nanoflower. Synthesized nanoflowers were characterized by UV-Vis, DLS, and TEM imaging.

To synthesize 60 nanometer gold nanoflowers, we start with a 40 nm seed; incubate with a 3 μM poly-A30 DNA sequence and varied the gold salt from 100 μL to 400 μL. The resulting nanoflowers followed a linear trend from 55 nm to 80 nm, with 250 μL corresponding to a 60 nm nanoflower. Synthesized nanoflowers were

characterized by UV-Vis, DLS, and TEM imaging. TEM characterization is summarized and presented in Figure 5.6.

The nanoflowers are then washed at least twice by centrifuge before storing in a NaOH treated 20 mL scintillation vials. In the following experiments, 1X concentration represents 100 μL of original stock nanoparticles per 500 μL final volume. The 1X concentrated nanoparticles are then incubated with thiolated DNA (previously treated with 0.4 mM TCEP for 1 hour in 5.2 pH phosphate buffer). After 16 hours, 30 μL of pH 8.2 phosphate buffer is added dropwise, followed by 300 μL of 1 M NaCl, added dropwise. The nanoparticles are stored for another 16 hours before use. Corresponding sizes of gold nanoparticles were functionalized similarly and stored in NaOH treated 20 mL scintillation vials. Prior to incubation, an appropriate amount of nanoparticles is transferred to a 2 mL centrifuge tube and centrifuged at 11k RPM for 20 minutes to remove excess salt.

The synthesized nanoflowers and correspondingly sized nanoparticles were then incubated with MCF-7 and LnCaP cell cultures to determine uptake profiles. The nanoflowers and nanoparticles were pelleted by centrifugation and dispersed in 1X Opti-Mem and introduced to cells grow on cover slips inside 6 well plates. Maintaining a constant incubation time of 2 hours, the concentration was varied from 1X concentrated to 5X concentration.

MCF-7 cell cultures were grown on sterilized glass cover slips in 6 well plates for overnight before uptake experiments. After incubating for 2 hours with 3X concentrated gold nanoparticles in 1X Opti-Mem cell culture media, the cells were washed three times in 1X PBS and fixed by incubating in 4% PFA in 1X PBS for 20 minutes at room

temperature. The coverslips were placed onto glass slides and characterized using an inverted optical microscope with a switchable brightfield / darkfield objective lens.

Figure 5.7 shows a comparison 40 nm nanoflowers with and without aptamer targeting after 2 hours incubation. It is observed that there is a high amount of scattering from within the cells, most likely from the scattering profile of gold nanoflowers and consistent with the positive controls. To quantify the amount of aptamer and control nanoflower inside the cells, dissolved cell samples were analyzed by inductive coupled plasma mass spectrometry.

Next, in order to compare size dependent uptake of gold nanoflowers, 20, 40, and 60 nm nanoflowers functionalized with either NCL aptamer sequence or a control sequence were incubated at 3X concentration for 2 hours at 37 °C. Figure 5.8 shows the uptake profile as characterized by darkfield microscopy. From the figure, it is observed that 40 nm nanoflowers achieved optimal uptake into MCF-7 cells and produced the greatest scattering signal. At time time, there has not been an in-depth characterization of the nanoflower's optical scattering profile with respect to size, therefore the uptake was also quantified by ICP-MS. The optical micrographs reveal that while scattering and uptake seems to increase with size of the nanoflowers, above 60 nm, there is a corresponding increase in non-specific binding of the nanoflowers to the surface.

Finally, to compare the uptake profiles of similarly sized nanoflowers with spherical nanoparticles, we incubated 20 nm, 40 nm, and 60 nm nanoflowers and nanoparticles, functionalized with the NCL aptamer strand for 2 hours at 37 °C. Figure 5.9 shows the brightfield and scattering profiles of each cell culture. It can be observed that at larger sizes, the nanoparticles are also observed to scatter light, but at a lower

intensity then the correspondingly sized nanoflowers. In order to quantify the uptake of nanoparticles and nanoflowers, each sample was repeated and analyzed by ICP-MS. Based on this data, we can conclude that nanoflowers, especially those roughly 40 nanometers, are effectively uptaken by MCF-7 cells when decorated with the appropriate aptamer strand. Thanks to its optical scattering profile, the 40 nm nanoflower is a significantly improved contrast agent over spherical nanoparticles and represents and improvement over traditional fluorescent labels in terms of photostability and ease of use.

5.3 Conclusions

We have demonstrated the successful synthesis of an aptamer functional nanoflower structure. To optimize the growth process, we used different sized starting gold seeds and optimized toward a minimum growth parameter which is defined by the condition at which optical and physical parameters characteristic of gold nanoflowers are first observed from the growth of DNA functionalized gold nanoparticles. We established that increasing the density of DNA strands onto the surface before the growth process does not improve stability in OPTIMEM media but post-synthesis PEGylation proved to be an effective strategy without impacting the properties of the nanoflowers. Finally, we were able to demonstrate selective uptake of aptamer functionalized nanoflowers by MCF-7 cells after 3 hours of incubation at 37 °C. Thanks to the high optical scattering profile of the nanoflower, we were able to characterize nanoflower uptake by bright and dark field optical microscopy. Further work is needed to understand the mechanism of uptake, whether the nanoflowers are attached to the surface of the cell or uptaken into the intracellular space, and quantify the uptake using ion-coupled plasma mass spectroscopy or transmission electron microscopy. Finally, preliminary data suggests that nanoflowers

synthesized and characterized here exhibit much faster uptake mechanisms at a 100x lower concentration then similarly functionalized spherical gold nanoparticles. If demonstrated, we expect the faster uptake at a lower concentration, targeted cell uptake, and easy imaging by optical microscopy will lead to an improved platform for cell type characterization over traditional dye and fluorescent based assays.

5.4 Experimental Details

All Oligonucleotides used in current study were purchased from Integrated DNA Technologies Inc. (Coralville, IA). 20 nm and 5 nm gold nanospheres (AuNSs) solutions were purchased from Ted Pella (Redding, CA) and purified using a centrifuge before use. Hydrogen tetrachloroaurate(III) hydrate ($HAuCl_4 \cdot 3H_2O$, 99.999%; Sigma-Aldrich), Hydroxylamine hydrochloride ($NH_2OH \cdot HCl$, 99.9999%; Sigma-Aldrich), Sodium hydroxide (NaOH, 98%; Sigma-Aldrich), Adenosine 5′-monophosphate sodium salt (AMP, 99%; Sigma-Aldrich), Tris(2-carboxyethyl)phosphine hydrochloride (TCEP, $C_9H_{15}O_6P \cdot HCl$; Sigma-Aldrich), 2-Mercaptoethanol (ME, 98%; Sigma-Aldrich) and mPEG thiol (CH_2O-$(CH_2CH_2O)_6$-CH_2CH_2SH, Mw = 356.5; Polypure) were used without further purification.

Synthesis of the gold nanoparticles mediated by DNA. The concentration of the purified 20 nm gold nanospheres (AuNSs) was calculated based on Beer–Lambert law (Extinction coefficient of 20 nm AuNS at 520nm is $9.406*10^8$ $M^{-1}cm^{-1}$) and then adjusted to 0.5 nM. 300 μL of 0.5 nM 20 nm AuNS solution was first incubated with 1 μM of DNA (poly A30, poly C30 or poly T30) for 15 min to let DNA adsorb onto the AuNS surface. 15 μL of 400 mM NH_2OH (adjusted to pH 5 with NaOH) was then added to the AuNS solution. After vortexing, 2.1 μL 1% (wt/wt) $HAuCl_4$ was introduced to AuNS

mixture solution ($HAuCl_4$ concentration in the mixture solution is 167 μM) to initiate the reduction reaction. A color change (depending on the sequence of the DNA used in the incubation step) was observed in seconds. The mixture solution was constantly vortexed for another 15 min until the reaction was complete. Based on the DNA sequences used and their shape, the synthesized gold nanoparticles were called AuNF_A30, AuNF_C30 or AuNS_T30 respectively.

Cell culture and nanoparticle incubation. AuNFs were synthesized with 1 μM of Fluorophore (FAM) labeled poly A30 (FAM-A30) by following the procedure in section 2. The AuNFs were purified by centrifuge before cell incubations. CHO (Chinese hamster ovary) and MCF-7 cells were cultured in Dulbecco's modified eagle medium (DMEM; Cell Media Facility, University of Illinois at Urbana-Champaign, Urbana, IL) supplemented with 10% fetal bovine serum (FBS), penicillin (50 U/ml), and streptomycin (50 μg/ml), at 37 ^{o}C in a humidified atmosphere of 5% CO2. Cells were seeded at a density of 1 x 10^5 cells/cm2 on a cover glass in a 6-well plate and the cells were grown for 24 hours before treatment with nanoparticles. After incubation with nanoparticles (normally 2 hours unless otherwise noted), the cells were washed with 1XPBS five times. The cells were then fixed using a 4% paraformaldehyde solution in 1X PBS for 20 minutes, and washed once more with 1XPBS before imaging.

Characterization Methods. Shape and size of gold nanoparticles as well as the nano-assemblies were analyzed using a JEOL 2010LaB6 transmission electron microscope (TEM) operated at 200 kV. Samples were prepared by putting a drop of nanoparticle solutions onto a carbon-coated copper TEM grid (Ted pella). Absorbance of the nanoparticle solutions were characterized using UV-Vis spectrophotometry (Hewlett–

Packard 8453). Darkfield light-scattering images were acquired using a Zeiss Axiovert 200M inverted microscope coupled with a CCD digital camera. The individual nanoparticle on the glass coverslip were imaged using an EC Epiplan 50X HD objective (NA=0.7) and the MCF-7 cells were imaged with a Plan-Neofluar 10x objective (NA=0.3). Prior to acquisition, the digital camera was white-balanced using Zeiss Axiovision software so that colors observed in the digital images represent the true color of the scattered light. Z-stacks of fluorescence images of the cells were acquired using Andor Technology Revolution System Spinning Disk Confocal Microscope at 100X objective (oil immersion, excitation wavelength 488 nm). The collected z-stacks of images were then deconvoluted and assembled into a 3D image using Autoquant X software and Imaris software.

5.5 References

(1) Jiang, W.; Kim, B. Y. S.; Rutka, J. T.; Chan, W. C. W. *Nat. Nanotechnol.* **2008**, *3*, 145-150.

(2) Walsh, A. S.; Yin, H. F.; Erben, C. M.; Wood, M. J. A.; Turberfield, A. J. *ACS Nano* **2011**, *5*, 5427-5432.

(3) Chithrani, B. D.; Ghazani, A. A.; Chan, W. C. W. *Nano Lett.* **2006**, *6*, 662-668.

(4) Qiu, Y.; Liu, Y.; Wang, L.; Xu, L.; Bai, R.; Ji, Y.; Wu, X.; Zhao, Y.; Li, Y.; Chen, C. *Biomaterials* **2010**, *31*, 7606-7619.

(5) Chithrani, B. D.; Chan, W. C. W. *Nano Lett.* **2007**, *7*, 1542-1550.

(6) Hutter, E.; Boridy, S.; Labrecque, S.; Lalancette-Hebert, M.; Kriz, J.; Winnik, F. M.; Maysinger, D. *ACS Nano* **2010**, *4*, 2595-2606.

(7) Yuan, H.; Li, J.; Bao, G.; Zhang, S. *Phys. Rev. Lett.* **2010**, *105*, 138101-138101.

(8) Tao, A. R.; Habas, S.; Yang, P. D. *Small* **2008**, *4*, 310-325.

(9) Xia, Y.; Xiong, Y.; Lim, B.; Skrabalak, S. E. *Angew. Chem. Int. Edit.* **2009**, *48*, 60-103.

(10) Seeman, N. C. *Nature* **2003**, *421*, 427-431.

(11) Rothemund, P. W. K. *Nature* **2006**, *440*, 297-302.

(12) Lu, Y.; Liu, J. *Accounts Chem Res* **2007**, *40*, 315-323.

(13) Lee, J. H.; Wernette, D. P.; Yigit, M. V.; Liu, J.; Wang, Z.; Lu, Y. *Angew. Chem. Int. Edit.* **2007**, *46*, 9006-9010.

(14) Braun, E.; Eichen, Y.; Sivan, U.; Ben-Yoseph, G. *Nature* **1998**, *391*, 775-778.

(15) Gu, Q.; Cheng, C. D.; Gonela, R.; Suryanarayanan, S.; Anabathula, S.; Dai, K.; Haynie, D. T. *Nanotechnology* **2006**, *17*, R14-R25.

(16) Alivisatos, A. P.; Johnsson, K. P.; Peng, X. G.; Wilson, T. E.; Loweth, C. J.; Bruchez, M. P.; Schultz, P. G. *Nature* **1996**, *382*, 609-611.

(17) Mirkin, C. A.; Letsinger, R. L.; Mucic, R. C.; Storhoff, J. J. *Nature* **1996**, *382*, 607-609.

(18) Warner, M. G.; Hutchison, J. E. *Nat. Mater.* **2003**, *2*, 272-277.

(19) Le, J. D.; Pinto, Y.; Seeman, N. C.; Musier-Forsyth, K.; Taton, T. A.; Kiehl, R. A. *Nano Lett.* **2004**, *4*, 2343-2347.

(20) Zhang, J. P.; Liu, Y.; Ke, Y. G.; Yan, H. *Nano Lett.* **2006**, *6*, 248-251.

(21) Bigham, S. R.; Coffer, J. L. *J. Phys. Chem.* **1992**, *96*, 10581-10584.

(22) Ma, N.; Dooley, C. J.; Kelley, S. O. *J. Am. Chem. Soc.* **2006**, *128*, 12598-12599.

(23) Kumar, A.; Jakhmola, A. *Langmuir* **2007**, *23*, 2915-2918.

(24) Ma, N.; Yang, J.; Stewart, K. M.; Kelley, S. O. *Langmuir* **2007**, *23*, 12783-12787.

(25) Berti, L.; Burley, G. A. *Nat. Nanotechnol.* **2008**, *3*, 81-87.

(26) Wang, Q.; Liu, Y.; Ke, Y.; Yan, H. *Angew. Chem. Int. Edit.* **2008**, *47*, 316-319.

(27) Ma, N.; Sargent, E. H.; Kelley, S. O. *Nat. Nanotechnol.* **2009**, *4*, 121-125.

(28) Wang, Z.; Zhang, J.; Ekman, J. M.; Kenis, P. J. A.; Lu, Y. *Nano Lett.* **2010**, *10*, 1886-1891.

(29) Storhoff, J. J.; Elghanian, R.; Mirkin, C. A.; Letsinger, R. L. *Langmuir* **2002**, *18*, 6666-6670.

(30) Wang, Z. D.; Zhang, J. Q.; Ekman, J. M.; Kenis, P. J. A.; Lu, Y. *Nano Lett.* **2010**, *10*, 1886-1891.

(31) Poon, K.; Macgregor, R. B. *Biopolymers* **1998**, *45*, 427-434.

(32) Petrovykh, D. Y.; Kimura-Suda, H.; Whitman, L. J.; Tarlov, M. J. *J. Am. Chem. Soc.* **2003**, *125*, 5219-5226.

(33) Wang, Z. D.; Lee, J. H.; Lu, Y. *Chem. Commun.* **2008**, 6005-6007.

(34) Giljohann, D. A.; Seferos, D. S.; Patel, P. C.; Millstone, J. E.; Rosi, N. L.; Mirkin, C. A. *Nano Lett.* **2007**, *7*, 3818-3821.

(35) Seferos, D. S.; Prigodich, A. E.; Giljohann, D. A.; Patel, P. C.; Mirkin, C. A. *Nano Lett.* **2009**, *9*, 308-311.

5.6 Figures

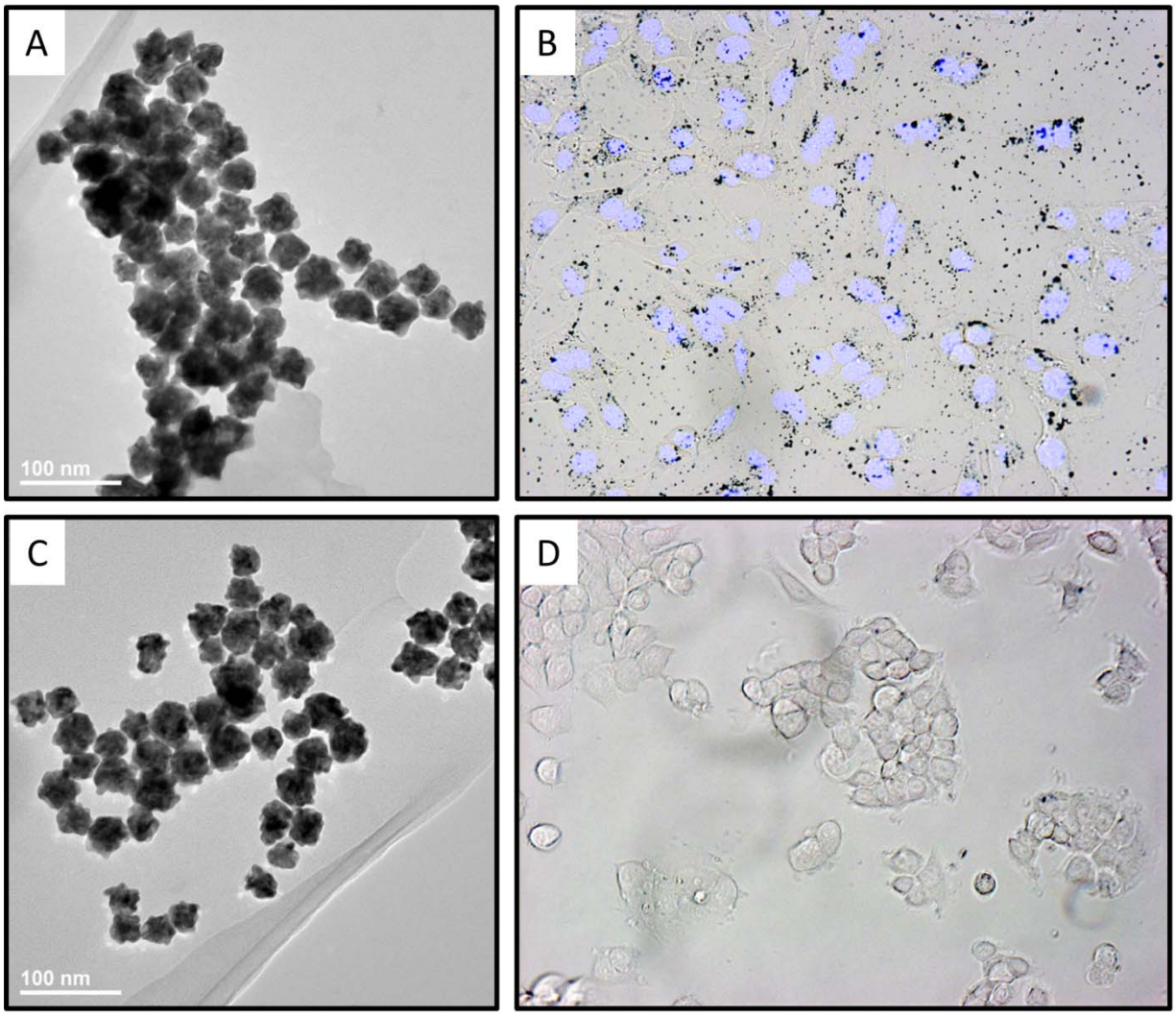

Figure 5.1 Nanoflowers via single strand design. Nanoflowers synthesized with polyC30-15T-Aptamer (A) and polyC30-15T-Control (C) strands and grown from 20 nm nanoparticle seeds. Bright field optical micrographs obtained after 2 hour incubation with MCF-7 cell cultures (aptamer strand and control strand, B and D, respectively).

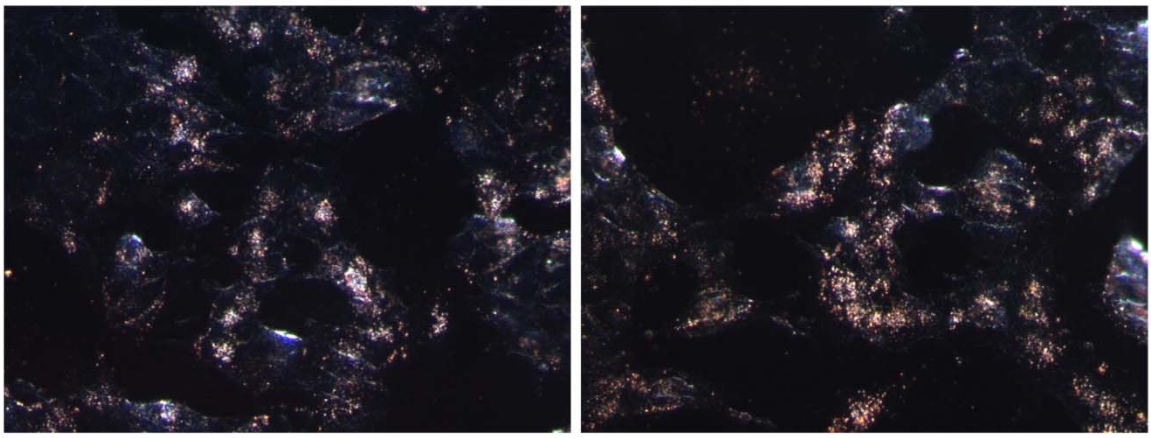

Figure 5.2 Positive controls for PEGylated nanoflowers. 40 nm gold nanoflowers, post-functionalized with PEG, grown from 20 nm nanoparticle seeds and polyC30-T15-Aptamer (Left) and polyC30-T15-Control (Right) strands are incubated with MCF-7 cell cultures for 24 hours. Imaged by darkfield optical microscopy.

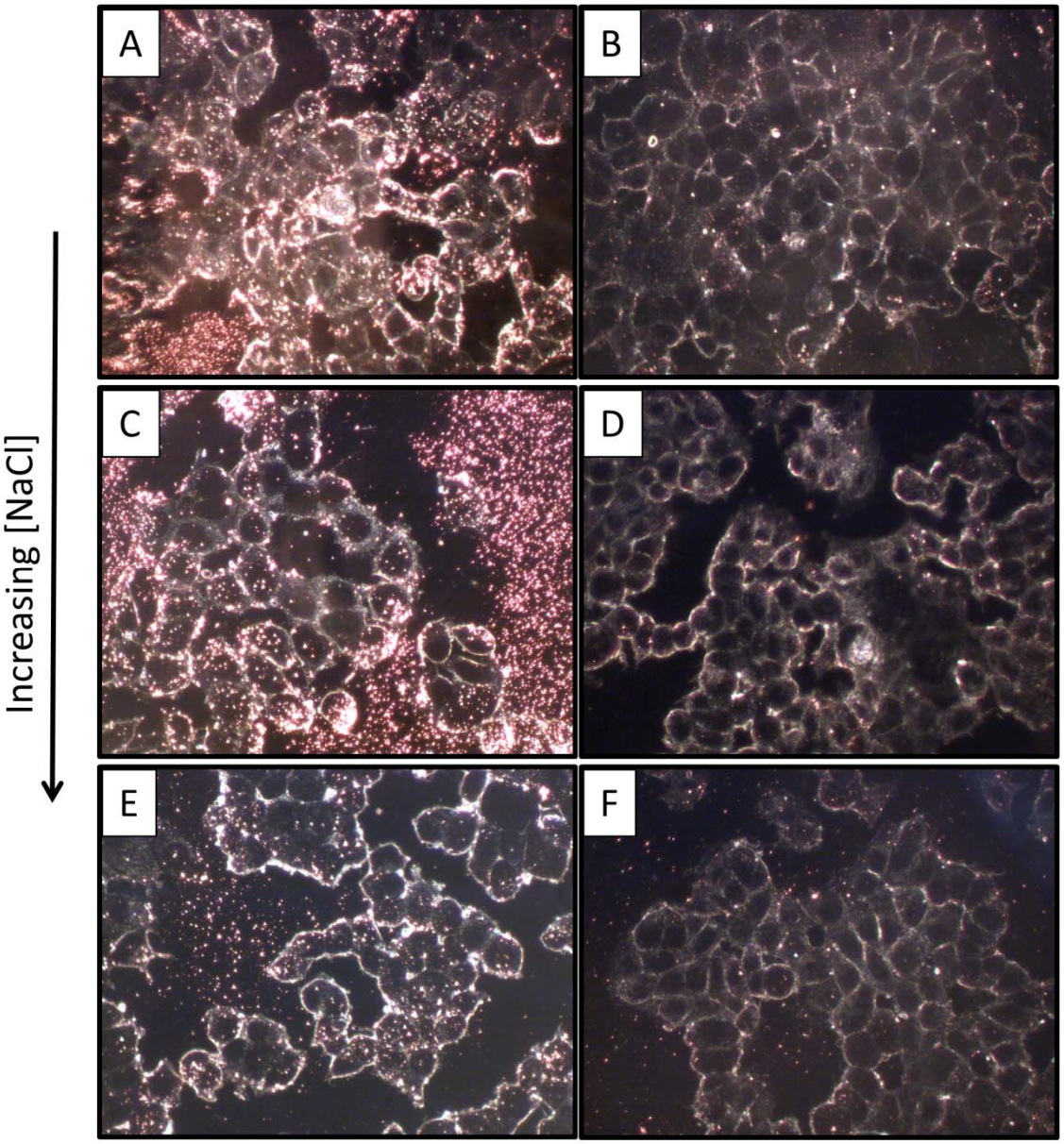

Figure 5.3 Cellular uptake of salt stabilized nanoflowers. The nanoparticle seeds were incubated in 0 mM (top), 25 mM (middle), and 75 mM (bottom) NaCl increased over 3 hours. The left and right column represents aptamer and control strands, respectively.

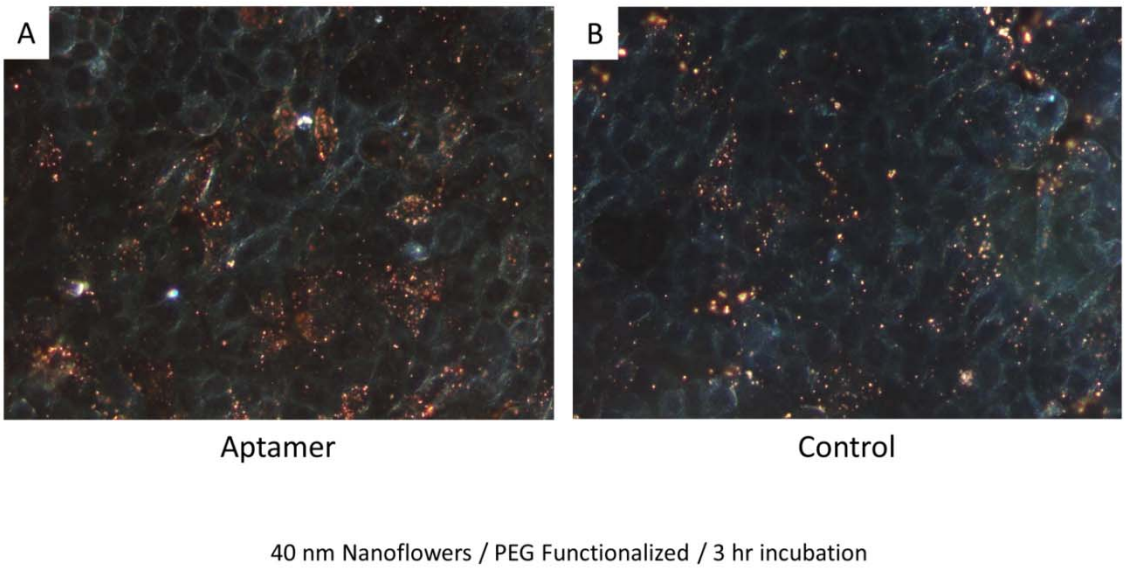

Figure 5.4 Darkfield optical micrographs obtained after 2 hour incubation of 40 nm nanoflowers synthesized from 20 nm nanoparticle seeds with 1 strand design. Post functionalization with thiolated PEG to reduce non-specific binding. Aptamer strand (Left) and Control sequence shown (Right).

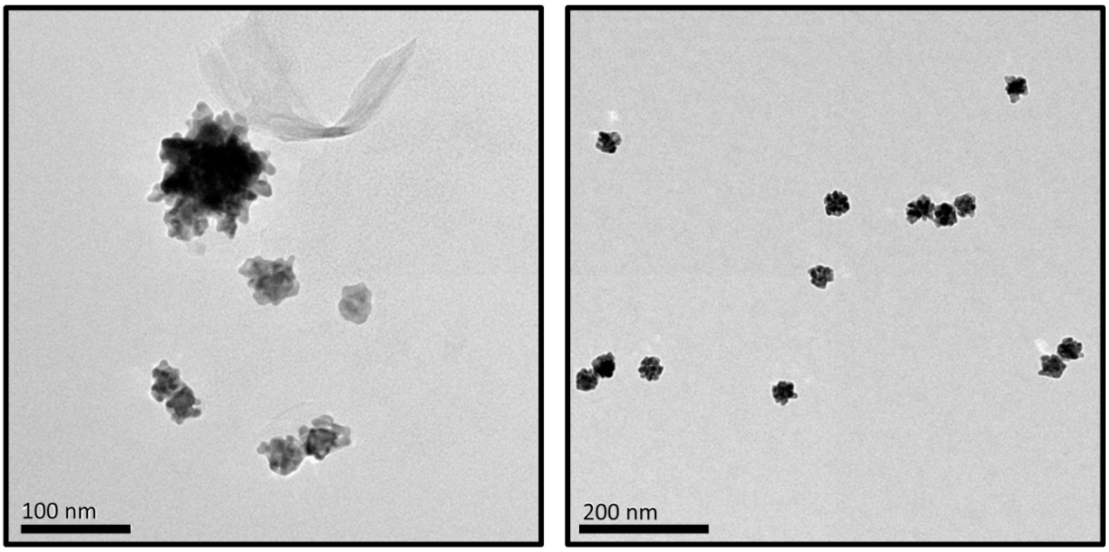

Figure 5.5 (Left) Nanoflowers synthesized using previously reported methods, note the difference in size of nanoflowers. (Right) Optimized procedures to synthesize a large range of nanoflower sizes with excellent homogeneity, as confirmed by transmission electron micrographs and dynamic light scattering.

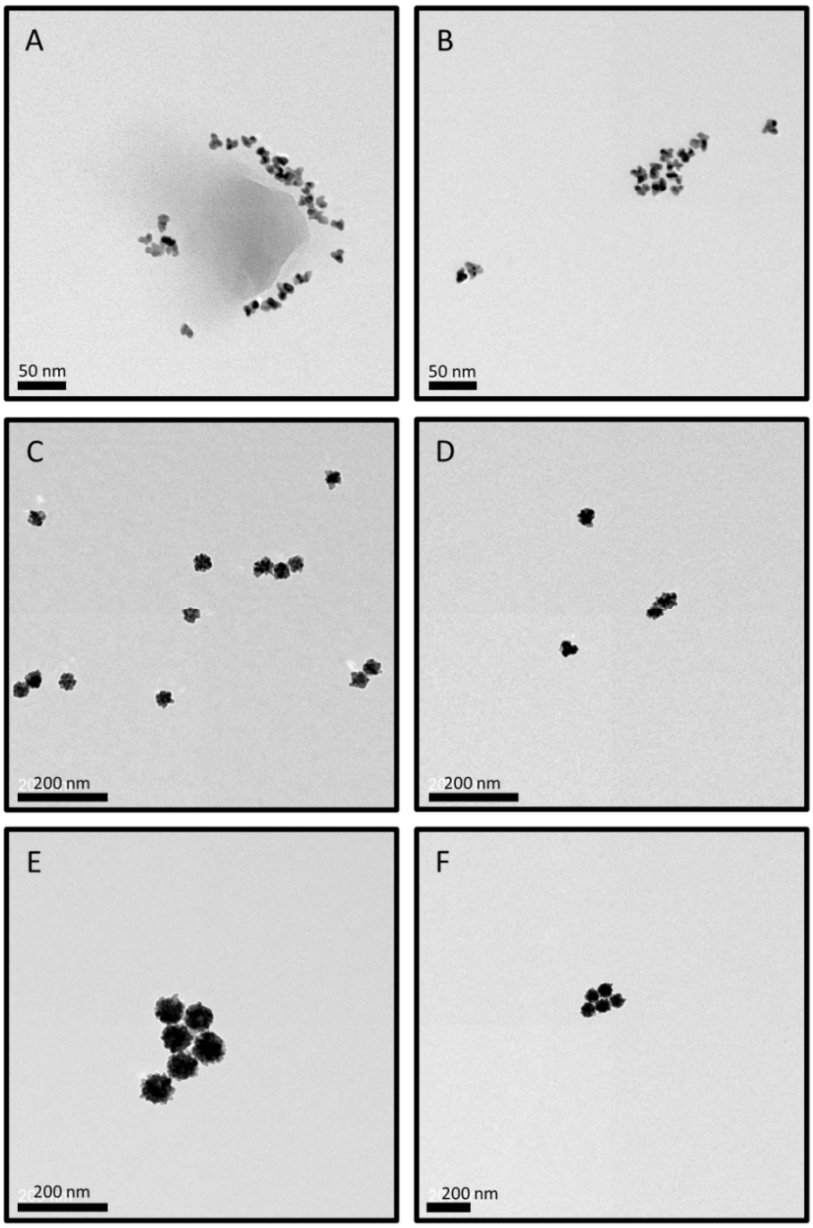

Figure 5.6 Size control of nanoflowers with excellent homogeneity with post-synthesis DNA functionalization. 20 nm nanoflowers grown from 10 nm seeds (aptamer and control sequences, A and B, respectively). 40 nm nanoflowers grown from 20 nm seeds (aptamer and control sequences, C and D, respectively). 60 nm nanoflowers grown from 40 nm seeds (aptamer and control sequences, E and F, respectively).

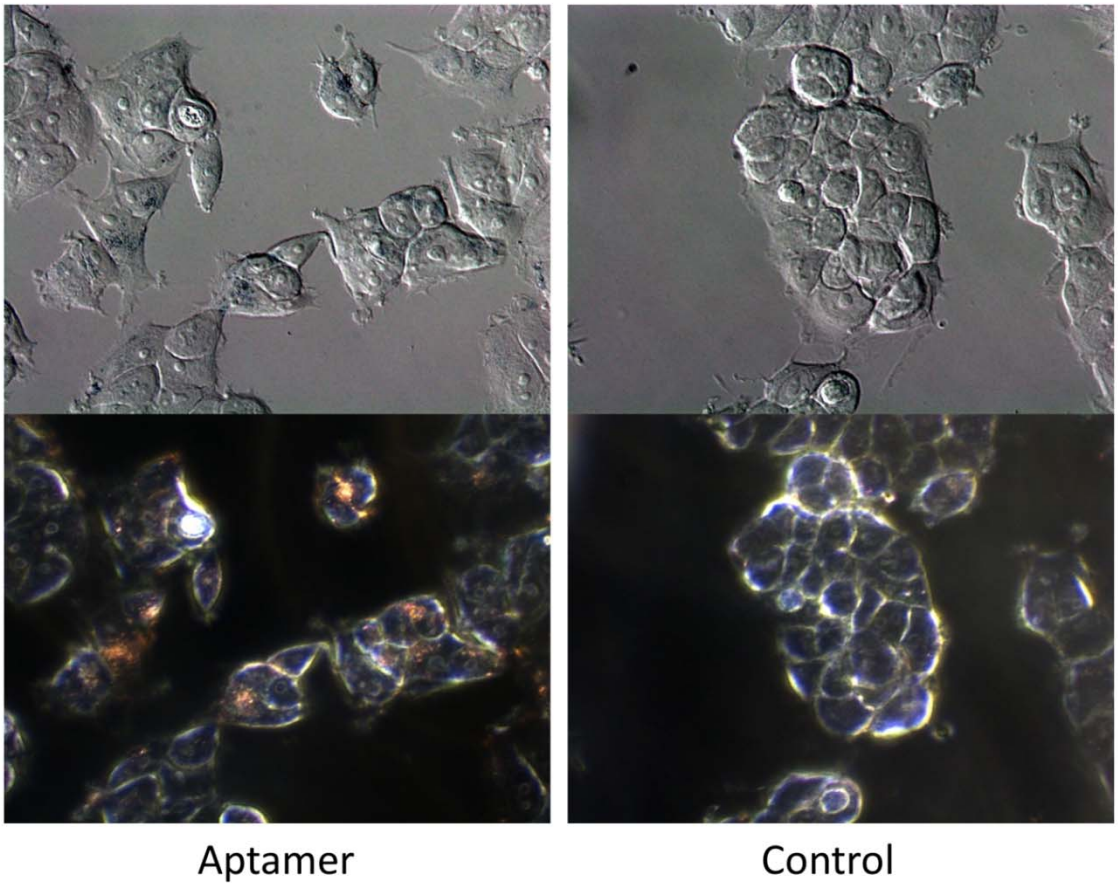

Figure 5.7 Selective uptake of aptamer decorated nanoflowers by MCF-7 cell culture. Bright and dark field optical micrographs of (Left) 40 nm nanoflowers, decorated with NCL aptamer post-synthesis, incubated with MCF-7 cell culture after 2 hour incubation and (Right) 40 nm nanoflowers, decorated with a control strand, after incubation for 2 hours under identical conditions.

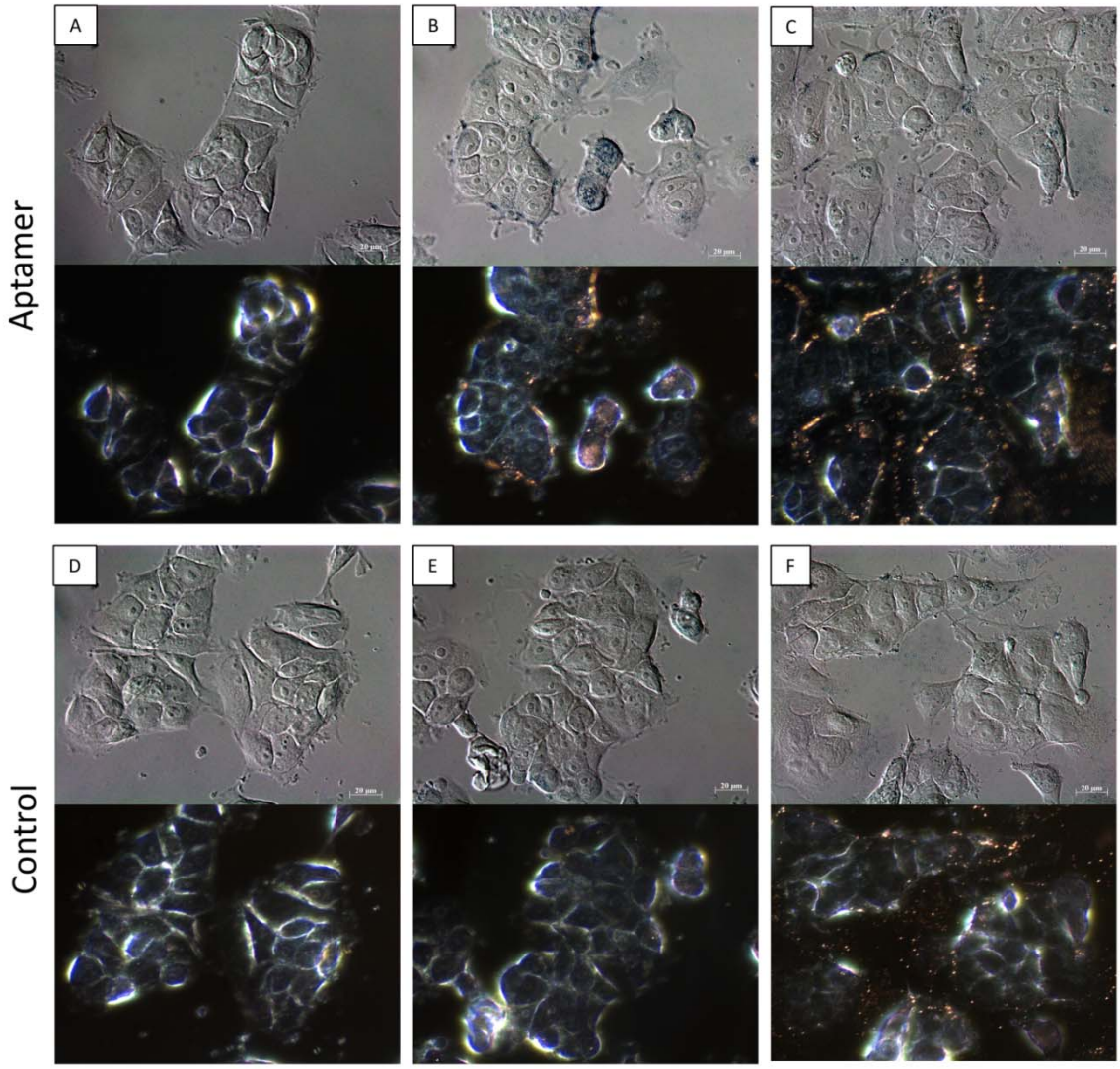

Figure 5.8 Optical micrographs analyzing size dependent uptake of aptamer and control sequence decorated nanoflowers. (A, D) 20 nm nanoflowers . (B, E) 40 nm nanoflowers. (C, F) 60 nm nanoflowers. It is observed that while targeted uptake is achieved, non-specific binding and uptake seems to increase with nanoflower size.

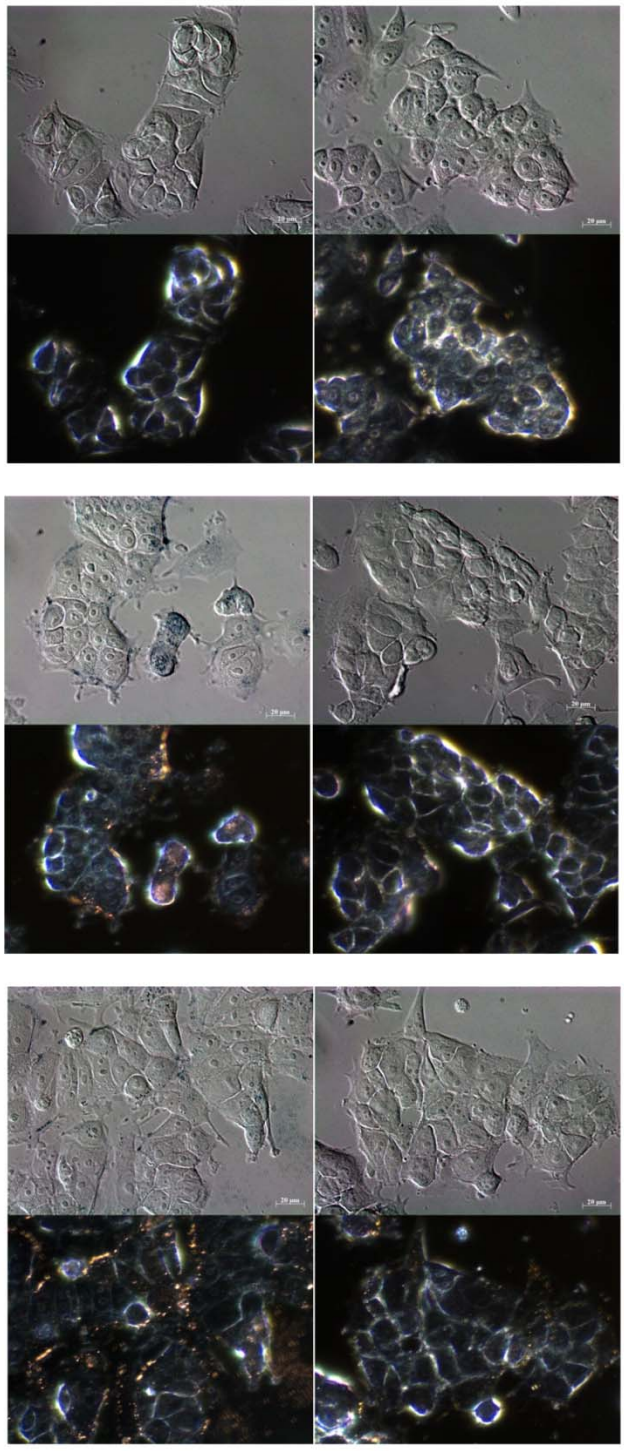

Figure 5.9 Optical uptake profile of similar sized, aptamer functionalized nanoflowers versus nanoparticles. (Left) 20, 40, and 60 nm nanoflowers. (Right) 20, 40, and 60 nm nanoparticles.

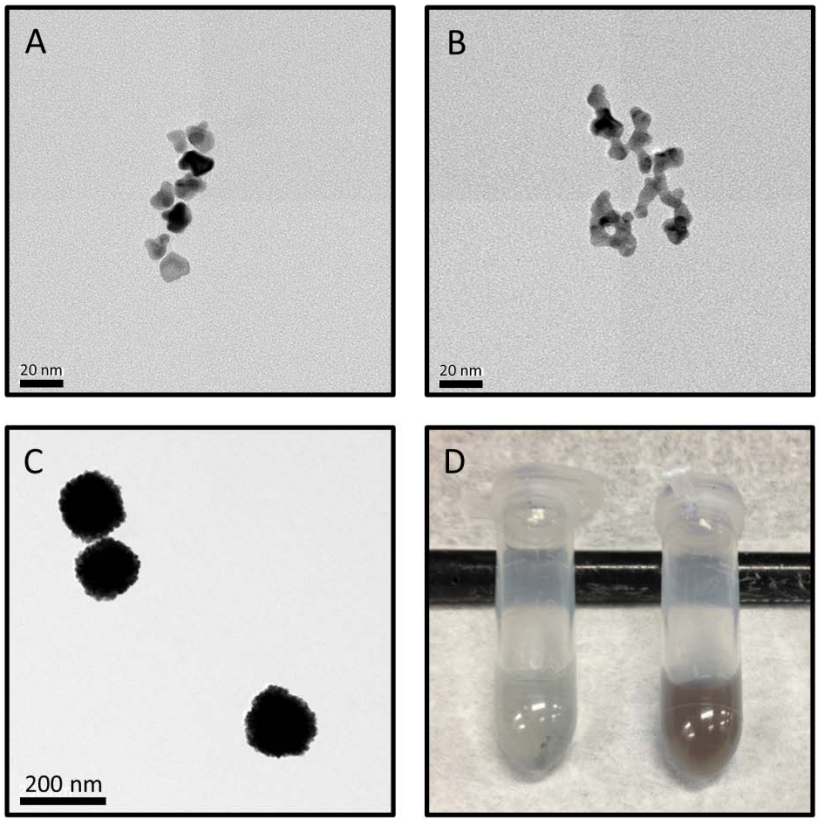

Figure 5.10 Lower and upper limits of nanoflower growth. Gold nanoflowers grown from 5 nm seed particles using polyA-30 strand using a (A) lower and (B) higher amount of gold salt. (C) Transmission electron micrograph of 200 nm gold nanoflowers grown from 20 nm particle seeds and 71 base pair strand. (D) Optical image showing the same growth conditions using a polyA-30 sequence results in quick aggregation of the nanoparticles (left tube) versus 200 nm nanoflowers structures that remain stable after 3 months of storage (right tube).

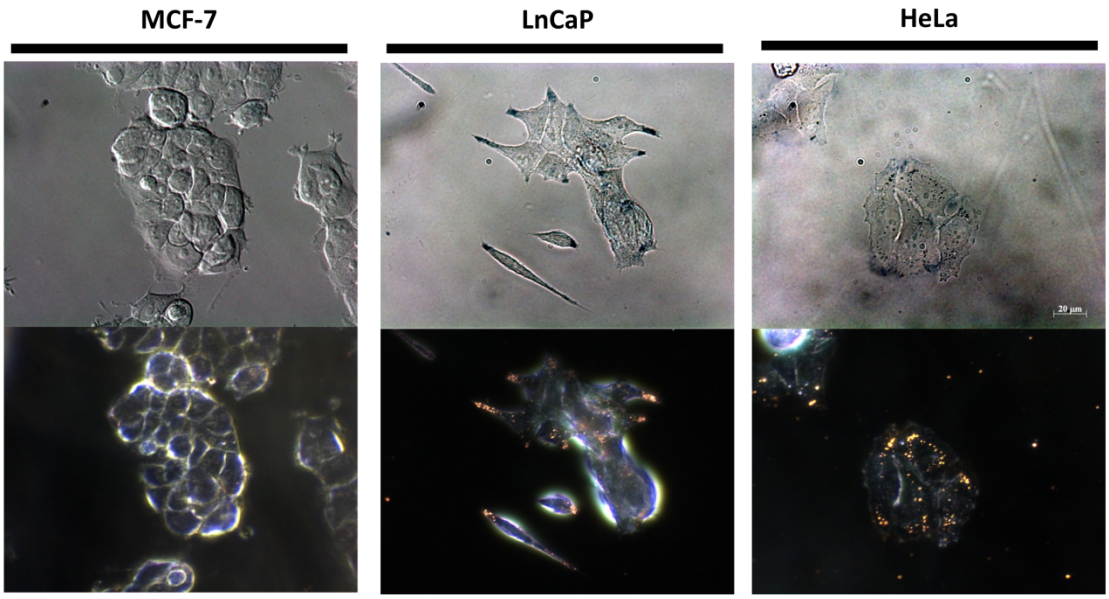

Figure 5.11 Comparison of cell type dependent uptake of 40 nm nanoflowers post-functionalized with a control oligo (randomized aptamer). Bright and dark field optical imaging shows patches of gold and yellow representing scattering signal from one or more gold nanoflower. (Left) Uptake profile of MCF-7 cells, with little to no signal observed indicating a lack of uptaken nanoflowers. (Middle) Uptake profile of LnCaP cells, with an observed concentrated scattering signal from cell "tips," representing a higher concentration of uptaken nanoflowers. (Right) Uptake profile of HeLa cells.